

Tunable room temperature nonlinear Hall effect from the surfaces of elementary bismuth thin films

Pavlo Makushko,¹ Sergey Kovalev,² Yevhen Zabala,^{1,3} Igor Ilyakov,² Alexey Ponomaryov,² Atiq Arshad,² Gulloo Lal Prajapati,² Thales V. A. G. de Oliveira,² Jan-Christoph Deinert,² Paul Chekhonin,^{1,4} Igor Veremchuk,¹ Tobias Kosub,¹ Yurii Skourski,⁵ Fabian Ganss,¹ Denys Makarov,^{1,*} and Carmine Ortix^{6,†}

¹*Helmholtz-Zentrum Dresden-Rossendorf e.V., Institute of Ion Beam Physics and Materials Research, 01328 Dresden, Germany*

²*Helmholtz-Zentrum Dresden-Rossendorf e.V., Institute of Radiation Physics, 01328 Dresden, Germany*

³*The H. Niewodniczanski Institute of Nuclear Physics, Polish Academy of Sciences, 31–342 Krakow, Poland*

⁴*Helmholtz-Zentrum Dresden-Rossendorf e.V., Institute of Resource Ecology, 01328 Dresden, Germany*

⁵*Helmholtz-Zentrum Dresden-Rossendorf e.V., Dresden High Magnetic Field Laboratory (HLD-EMFL), 01328 Dresden, Germany*

⁶*Dipartimento di Fisica “E. R. Caianiello”, Università di Salerno, IT-84084 Fisciano (SA), Italy*

The nonlinear Hall effect (NLHE) with time-reversal symmetry constitutes the appearance of a transverse voltage quadratic in the applied electric field. It is a second-order electronic transport phenomenon that induces frequency doubling and occurs in non-centrosymmetric crystals with large Berry curvature – an emergent magnetic field encoding the geometric properties of electronic wavefunctions. The design of (opto)electronic devices based on the NLHE is however hindered by the fact that this nonlinear effect typically appears at low temperatures and in complex compounds characterized by Dirac or Weyl electrons. Here, we show a strong room temperature NLHE in the centrosymmetric elemental material bismuth synthesized in the form of technologically relevant polycrystalline thin films. The (111) surface electrons of this material are equipped with a Berry curvature triple that activates side jumps and skew scatterings generating nonlinear transverse currents. We also report a boost of the zero field nonlinear transverse voltage in arc-shaped bismuth stripes due to an extrinsic geometric classical counterpart of the NLHE. This electrical frequency doubling in curved geometries is then extended to optical second harmonic generation in the terahertz (THz) spectral range. The strong nonlinear electrodynamic responses of the surface states are further demonstrated by a concomitant highly efficient THz third harmonic generation which we achieve in a broad range of frequencies in Bi and Bi-based heterostructures. Combined with the possibility of growth on CMOS-compatible and mechanically flexible substrates, these results highlight the potential of Bi thin films for THz (opto)electronic applications.

Second-order electrical responses are fundamentally prohibited in material structures with inversion symmetry. Essential nonlinear electrodynamic operations such as frequency mixing and current rectification are thus sought in non-centrosymmetric materials. This excludes the largest class of materials known to mankind: non-magnetic ones with bulk inversion symmetry. However, this paradigm is strictly valid only in bulk three-dimensional materials. At surfaces

and interfaces, the centrosymmetry of the structure is naturally broken, and certain second harmonic electrodynamic processes are symmetry-allowed. For instance, the nonlinear Hall effect (NLHE) [1–3] due to the Berry curvature dipole can be non-vanishing at surfaces with unusually low crystalline symmetries [4]. Surface-induced nonlinear electrical processes have been also observed [5] at the (111) surface of Bi₂Se₃ – a strong three-dimensional topological insulator with trigonal symmetry [6]. The threefold rotational symmetry of its crystal forces the Berry curvature dipole associated with the topological surface Dirac cone to vanish. However, a higher order moment, dubbed Berry curvature triple (BCT), activates side jumps [7, 8] and skew scatterings capable of inducing large nonlinear responses. This effect, dubbed as quantum frequency doubling in Ref. [5] and disorder-induced NLHE in Ref. [3], is different with respect to the nonlinear Hall effect related to the Berry curvature dipole only in that the transversal nonlinear currents are related to dissipative longitudinal responses [see Ref. [2] and Supplementary Information]. In the remainder, we will adopt the nomenclature of Ref. [3], and refer to this effect as NLHE capitalizing on the fact that what is observed is an electrical second-harmonic generation in the transverse channel related to the geometric properties of the wavefunctions.

Second harmonic generation (SHG) and current rectification due to geometric properties of Bloch electrons [9] have been predicted to be highly efficient at high frequencies and thus possibly relevant for optoelectronic applications [10, 11] in the terahertz spectral domain. To bring this concept to reality, a number of criteria should be fulfilled [*c.f.* Table I]. First, the nonlinear transverse responses should be sizable at room temperature and above. Second, the NLHE voltage should be controllable by a non-thermal parameter and thus be tunable. Third, NLHE-based devices should rely on technologically relevant material fabrication, for instance, with the use of CMOS-compatible (*e.g.* silicon) and mechanically flexible substrates (*e.g.* polymers). This can be achieved by first searching for materials with a simplified chemical composition, ideally single-element systems, and then for low-cost microstructures: polycrystalline thin films rather than single crystals. Finally, toxic heavy rare-earth materials should be eliminated all together, thus paving a way towards green (opto)electronics. Room-temperature nonlinear Hall effect has been observed in the ternary type-II Weyl semimetal [12]

* d.makarov@hzdr.de

† cortix@unisa.it

TaIrTe₄ and in the Dirac material BaMnSb₂ [13]. Tunability via gating has been instead theoretically predicted and experimentally verified at low temperatures in low-dimensional materials including transition metal dichalcogenides [14–22], bilayer graphene [23, 24], and oxide interfaces [25]. Here, we report the discovery of the first material structure fulfilling all the technologically relevant criteria at the same time: (111) polycrystalline thin films of elemental bismuth. The strong spin-orbit coupled surface states of this element [26, 27] are equipped with a finite Berry curvature that averages to zero but possesses a finite BCT. Importantly, the room-temperature NLHE of this green [28] semimetal can be efficiently tuned using a curvature-induced classical shape effect [29], namely the geometric NLHE whose signatures have been reported so far only in graphene [30]. We show that this effect is present in full force in polycrystalline thin films and cooperates with the BCT to create second harmonic transverse electrical responses. Moreover, we report a complementary optical SHG at THz frequencies in arrays of arc-shaped bismuth stripes, thereby providing for the first time signatures of the connection between nonlinear transport at low frequencies and optical nonlinearities at higher frequencies.

We prepared Bi thin films with a nominal thickness of 100 nm by magnetron sputtering at room temperature. The thin films are characterized using X-ray diffraction (XRD) [c.f. Fig. 1(a)], which reveals a polycrystalline microstructure with grains of typical size of $\simeq 33$ nm. Furthermore, XRD and electron backscatter diffraction (EBSD) data [Supplementary Information] indicate a preferred rhombohedral (111) crystallographic texture [c.f. Fig. 1(b)], and hence the possibility of non-trivial geometric properties of the surface electronic waves in the material [31]. The EBSD pole figures indicate the thin films to be structurally isotropic within the film plane.

The polycrystalline nature of the Bi thin films does not hinder the appearance of quantum phenomena conventionally observed in single crystals. This is verified in Fig. 1(c), where we show that the high-field magnetoresistance is characterized by a drop when the externally applied in-plane magnetic field $B > 35$ T. This is consistent with a previous study [32] that related such high-field magnetoresistance drop with the complete drying of a Fermi sea of electrons confined to their lowest Landau levels, and thus well inside the so-called quantum limit [33] attained in Bi crystals at magnetic fields $B > 15$ T.

The high-field magnetotransport measurement of Fig. 1(c) probes a quantum response associated with the bulk hole and electron states. However, it makes no assertion on the presence and physical properties of surface states. To overcome this hurdle, we employ a terahertz third harmonic generation (THG) approach, which was previously used to study the Dirac states at the surface of topological insulators [34]. Specifically, a THz excitation at the fundamental frequency of 300 GHz is applied with normal incident pulse. The generated third harmonic at 900 GHz is characterized in time-domain using electro-optical sampling. A systematic analysis of the THz THG in our Bi thin films proves the surface origin of the signal, analogously to the surface-mediated THz nonlinearities in topological insulators [35]. The THz THG amplitude reveals only very weak temperature dependence, as shown in

Fig. 1(d). We also observe a quenching of the THz THG signal for Bi films thinner than 15 nm [c.f. Fig. 1(e) and Supplementary Information]. This indicates a surface band gap opening due to the hybridization of surface states belonging to opposite surfaces. Further evidence that high harmonic generation in Bi is predominantly due to its surface states comes from the study of Bi/Au multilayers. As shown in Fig. 1(f), a stack of four Bi(25 nm)/Au(2 nm) heterolayers has a more efficient THz THG as compared to two stacked Bi(50 nm)/Au(4 nm) bilayers, in agreement with the fact that in the former multilayer the number of surfaces is doubled. The linear THz emission is instead the same for the two multilayers since the total thickness of the Bi and Au layers are equal.

The observed highly nonlinear kinetics at THz frequencies of the Bi surface states can be ascribed to a low surface carrier density – this implies a reduced heat capacity and thus enhanced thermodynamic nonlinearity [36] – and to surface band dispersions that contain terms growing linearly with the crystalline momentum [37]. Bismuth has been recently classified as an higher-order topological insulator [38], with a trivial value of the \mathbb{Z}_2 topological invariant [39] for systems in the AII class of the Altland-Zirnbauer classification [40]. This immediately implies that the surface states cannot realize Dirac cones [Supplementary Information]. Nevertheless, the strong spin-orbit coupling of Bi combined with the surface inversion symmetry breaking yields a sizable, linear in k , Rashba spin-orbit coupling. Additionally, the (111) texture of our polycrystalline samples leads to a hexagonal warping that has a twofold effect. First, the surface bands have Fermi lines with a hexagonal “snowflake” shape [41]. Second, electrons are equipped with a non-vanishing local Berry curvature driven entirely by crystalline anisotropy effects. These two properties enable both nonlinear side-jumps [2, 7, 8] and nonlinear skew scattering due to the fact that surface Bloch electrons with opposite velocities self-rotate in opposite directions and give rise to a net Magnus effect [c.f. Fig. 1(g)] quantified by the BCT [Supplementary Information]. Importantly, the third-order skew scattering deflections of surface electrons belonging to different Rashba branches do not cancel each other and lead to a net contribution to the NLHE [Supplementary Information].

To verify the occurrence of this quantum transport effect, we pattern our polycrystalline samples in a Hall cross geometry [c.f. Fig. 2(a)]. We first perform temperature dependent Hall resistance measurements by applying an external out-of-plane magnetic field. Consistently with the high-field magnetotransport characterization, we find Hall transport to be dominated by bulk carriers: the Hall coefficient displays a strong temperature dependence [c.f. Fig. 2(b)]. The associated bulk carrier density of $n = 2 \cdot 10^{26} \text{ m}^{-3}$ at room temperature [c.f. Fig. 2(c)] is consistent with previous reports on Bi thin films and single crystals. This holds true also when considering the temperature decrease of the sheet resistance [c.f. Fig. 2(c)].

Zero-field transport properties are obtained by sourcing an oscillating current with frequency $\omega/(2\pi)$ along the \hat{x} direction, and concomitantly measuring the longitudinal U_{xx}^ω as well as the first (U_{xy}^ω) and second ($U_{xy}^{2\omega}$) harmonic transverse voltages in a conventional lock-in detection scheme.

Fig. 2(d) [see also Supplementary Information] shows the ensuing current-voltage characteristic of the first harmonic longitudinal response, which remains linear over the full range of sourced currents [Supplementary Information]. This Ohmic behavior allows us to exclude a leading role played by Schottky barriers. Furthermore, using a bimaterial model, we estimate thermal effects due to Joule heating to be negligible [Supplementary Information]. We also find the first harmonic transverse voltage U_{xy}^ω [c.f. Fig. 2(d)] to be three orders of magnitude smaller than U_{xx}^ω . This is consistent with the fact that in time-reversal symmetric conditions linear transverse responses are symmetry-allowed only in crystals of sufficiently low symmetry. The threefold rotation symmetry of Bi implies that the in-plane resistivity can be described by a single scalar. Therefore, the transverse voltage U_{xy}^ω is forced to vanish both in single crystals and in polycrystalline (111) Bi thin films.

Second-order transverse responses are instead completely compatible with a threefold rotational symmetry [Supplementary Information]. The bulk centrosymmetry of Bi however implies that any second-order electrical response, if finite, must originate entirely from its surface states. Fig. 2(e) demonstrates that our polycrystalline Bi thin films possess a surface-induced second-order transverse response. We note that the transverse voltage $U_{xy}^{2\omega}$ has a characteristic quadratic current-voltage behaviour: the measured signal can be reliably fitted by the relation $U_{xy}^{2\omega}(I_x) = R_{yxx}^{2\omega} \cdot I_x^2$ with $R_{yxx}^{2\omega} = 166 \Omega/\text{A}$. Combined with the fact that the response occurs at double the driving frequency, this establishes the electronic second-order nature of the effect. We show this nonlinear transverse response to be present also in a Bi device grown on mechanically flexible polymeric substrate [Supplementary Information]. Furthermore, the surface-mediated NLHE of Bi establishes a general approach to generate this effect in other elemental materials. Various noble metals, such as Pt, Rh or Ir, do feature surface states [4]. As proof of concept, we verify the presence of a nonlinear Hall voltage in 5-nm-thick Pt thin film [Supplementary Information].

Being related to an intrinsic geometric property of surfaces electronic wavefunctions in a bulk material, the electronic second harmonic generation due to the BCT cannot be tuned using a non-thermal control parameter. This is different from the gate dependence widely reported at low temperatures in low-dimensional materials with finite Berry curvature dipoles [14, 19, 24, 25]. Nevertheless, we are able to reach control of the magnitude of the nonlinear transverse voltage using a curvature-induced classical shape effect [29]: the so-called geometric nonlinear Hall effect [30]. This phenomenon is due to the spontaneous appearance in bent conducting channels of a transverse electric potential, which is necessary to accelerate radially the charge carriers and let them follow the curved path of the material microstructure. As a result, surface charges similar in nature to those of the classical Hall effect arise, even in the complete absence of external perpendicular magnetic fields. The presence of time-reversal symmetry implies that the electrical transverse potential needs to be quadratic in the injected current density, qualifying this curvature-induced effect as nonlinear Hall. Importantly, the loss of centrosymmetry necessary for the occurrence of the

nonlinear electrical response is obtained at the level of the mesoscale geometry of the material structure, in strict analogy with the flexoelectric effect [42]. Conceptually speaking, a geometric nonlinear Hall effect is therefore allowed even in centrosymmetric crystals. In the specific case of bismuth thin films, this implies that both surface charge carriers and bulk charge carriers can in principle give rise to a geometric nonlinear Hall response.

We verify the occurrence of this geometric effect by patterning arc-shaped Hall bars [c.f. Fig. 3(a)] with the longitudinal arc-shaped channels that have inner curvature radii, r_{in} , of $\simeq 3, 6$ and $9 \mu\text{m}$ and a width in the radial direction of $w \simeq 1.2 \mu\text{m}$: this quasi-one-dimensional geometry of the longitudinal channel guarantees substantial geometry-induced modifications of charge motion. We first verify [c.f. Fig. 3(b)] that electrical transport in the linear response regime is Ohmic with the current-voltage characteristic that is linear in all the range of sourced currents. The corresponding longitudinal resistivities are independent of the specific curvature radius and similar to the conventional Hall cross devices discussed in Fig. 2(c). Fig. 3(b) also shows that the transverse voltage is suppressed indicating the absence of geometric effects in the linear response [see Supplementary Information].

The nonlinear response has instead a completely different behavior. As shown in Fig. 3(c), the second harmonic transverse voltage of the arc with inner radius $r_{in} = 3 \mu\text{m}$ inner radius has about 500% increase with respect to the Hall cross. The geometric NLHE of bismuth can be larger than the contribution from the BCT of its surface states. Our data show that control of the mesoscale curvature of the conducting channel can be used to tune the nonlinear transverse voltage $U_{xy}^{2\omega}$. This is in agreement with the fact that the geometric contribution is expected to scale inversely with the inner arc radius r_{in} as [30]

$$U_{xy,geo}^{2\omega} \simeq \frac{1}{r_{in} w t^2} \frac{m}{n^2 q^3} I_x^2,$$

where t, w indicate the thickness and width of the conducting channel, respectively, while n, m, q indicate the density, mass and charge of the carriers, respectively. Figure 3(d) shows that the Bi arcs follow the curvature radius scaling of the nonlinear Hall voltage predicted in the equation above. We can also attribute the sizable geometric NLHE of the arc-shaped Hall crosses predominantly to the Bi surface states. Considering the charge carrier density obtained from magnetotransport measurement [Fig. 2(c)], the bulk contribution to $U_{xy,geo}^{2\omega}$ lies in the hundreds of pV for a 100 nm-thick film. When considering the surface states contribution, the film thickness has to be replaced with their nanometer sized penetration depth. This can lead to a strong boost of the transverse voltage up to the scale of μV in agreement with our experimental observations.

The strong enhancement of the NLHE due to curvature effects at low frequencies is complemented by the occurrence of optical second harmonic generation (SHG) in the terahertz spectral domain. Extended arrays of 100-nm-thick Bi arcs with inner radius of $3 \mu\text{m}$ [see Fig. 3(e)] display a SHG signal at 600 GHz in response to a 300 GHz excitation. We also observe a strong polarization dependence in the THz SHG sig-

nal of Bi arcs. As shown in Fig. 3(f) the second harmonic peak is enhanced when the incident electric field is polarized along the arc, *i.e.* perpendicular to the symmetry axis of an individual arc structure. This is consistent with the main feature of the geometric NLHE. Furthermore, the universality of the geometric nonlinear transport effect is paralleled by the ubiquitous occurrence of THz SHG in devices with curved geometries. As shown in Supplementary Information, arrays of 20-nm-thick Au arcs display an even stronger SHG signal, even though THz THG is completely absent in Au thin films. In Ref. [43], SHG was observed in devices with gold splitting resonators arrays and attributed to the nonlinear Thomson scattering. We note that in our devices this mechanism is unlikely to be responsible of the SHG at the fundamental frequency of 0.3 THz due to the small dimensions of Au and Bi arcs. We can therefore attribute the THz SHG of our study to geometric effects related to Bi and Au surface states. Intrinsic second-order nonlinear effects related to well-known surface states of Au [44] have been anticipated in Ref. [43].

The room temperature nonlinear electrodynamic responses featured above indicate that elemental bismuth generally possess large THz nonlinear susceptibilities and high harmonic conversion efficiencies. We observe [*c.f.* Fig. 4(a)] highly-efficient room temperature THz THG with the efficiency that can be tuned changing the thin film microstructure either via thermal processing [*c.f.* Fig. 4(b) and Supplementary Information] or by growing Bi/Au heterolayers [*c.f.* Fig. 1(f), Fig. 4(c) and Supplementary Information]. We find a field conversion efficiency (FCE) of the third harmonic that can reach values $\simeq 2.5\%$ [*c.f.* Fig. 4(d)] thus surpassing the performance of Bi₂Se₃: the benchmark material providing by now the highest known efficiency of THz THG [45]. Note that for the nonlinear transport in the DC limit Bi₂Se₃ has been reported [5] to display nonlinear Hall voltages that reach a few μV sourcing currents of 1 mA. In Bi polycrystalline thin films, similar nonlinear Hall voltages are reached [*c.f.* Fig. 3(c)] sourcing currents of 40 μA . This tenfold decrease in the required current and the fact that the DC NLHE in Bi₂Se₃ occurs only at temperatures < 200 K additionally demonstrate the advantages of Bi thin films for nonlinear electrical and electrodynamic responses.

We also demonstrate efficient THz THG in a broad frequency range [*c.f.* Fig. 4(e)]. Upon increase of the fundamental frequency from 300 GHz to 500 GHz, high efficiency of the generated third harmonic retains even at 1.5 THz. Furthermore, the fluence dependence of THz THG and fifth harmonic does not show any saturation [*c.f.* Fig. 4(f)], see also [Supplementary Information]. This indicates the absence of detrimental heat accumulations effects, and thus of ultrafast electronic heat dissipation due to Coulomb scattering between surface-state charges and bulk charges [46]. The ensuing possibility of using pulses of longer duration enabling parametric processes together with the observed broad-range high efficiency paves the way to green optoelectronic devices for prospective communication technologies, *e.g.* sixth generation (6G) networks. In this regard, elementary bismuth offers key advantages due to established commodity scale production, commercial availability and possibility of straightforward process-

ing as technologically relevant thin films. Furthermore, due to its notorious magnetoresistance and Hall effects [47], bismuth is also relevant for sensor applications [48, 49]. Finally, the combination of nonlinear electrodynamical capabilities and higher-order topological properties leading to spin-momentum locked hinge modes can be used to integrate optoelectronic and spintronic functionalities in a single elemental material system. Topological properties have been recently shown to appear even in amorphous matter [50]. From a fundamental point of view, our results represent the first step forward in realizing Berry curvature-mediated effects in polycrystalline structures, and thus open a vast space of exploration of quantum effects related to the electronic wavefunction geometry using modern thin film technology.

TABLE I. Materials for the nonlinear Hall effect vs relevant criteria for their technological exploitation.

Materials for nonlinear Hall	Chemical composition	Operating temperature	Tunability	Green
Transition metal dichalcogenides (Refs [14], [19], [20], [51], [22])	Binary compound	< 100 K	✓	✗
Twisted and corrugated graphene (Refs [52], [24])	Elemental	<200 K	✓	✓
Weyl semimetals (Ref [13])	Ternary compound	Room temperature	✗	✗
Dirac semimetals (Ref [13])	Ternary compound	Room temperature	✗	✗
Topological insulators (Ref [52])	Binary compound	<200 K	✗	✗
Oxide heterostructure (Ref [25])	Ternary compounds	<30 K	✓	✗
Bismuth (this work)	Elemental	Room temperature	✓	✓

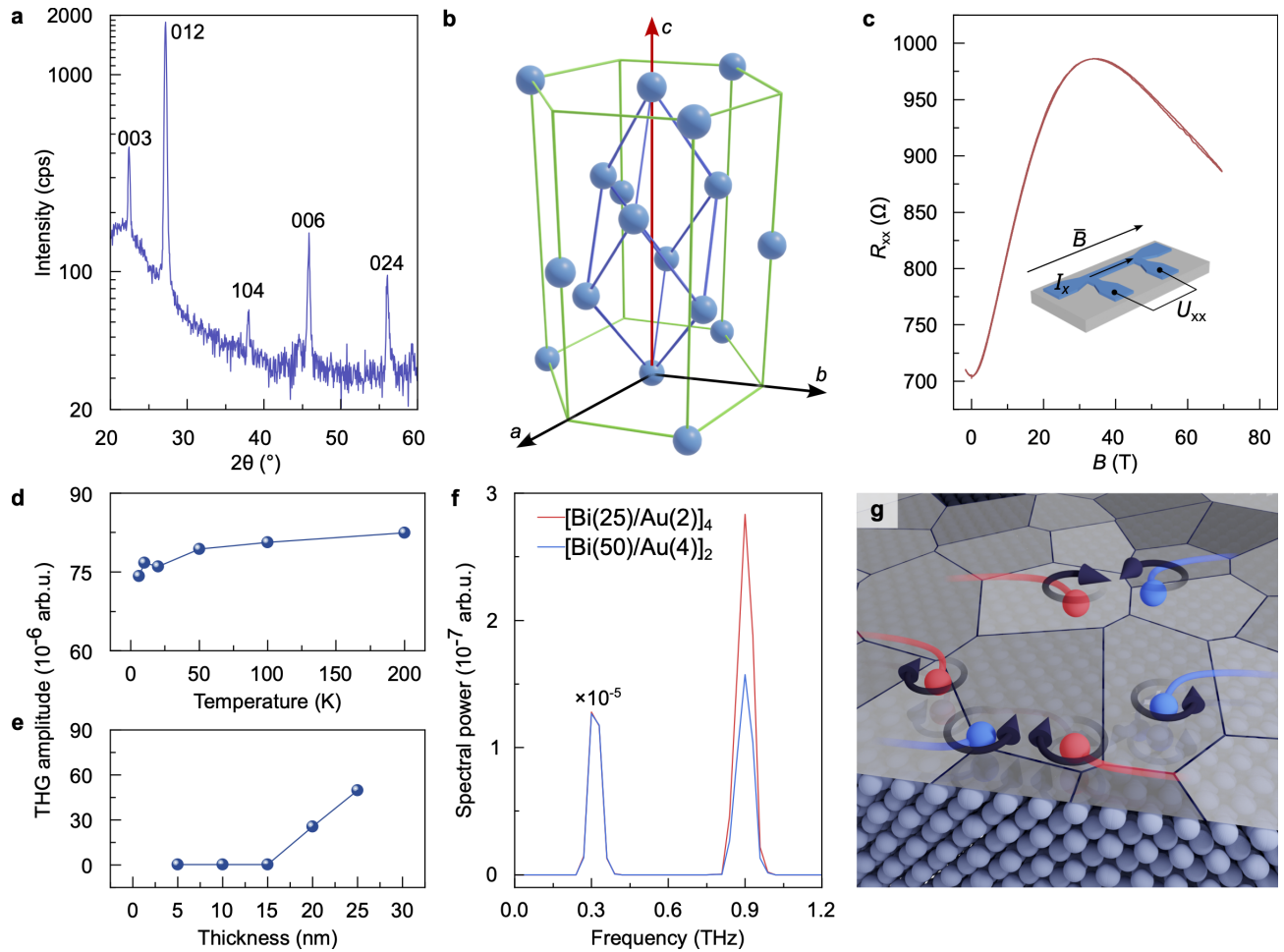


FIG. 1. **Quantum properties and surface states of polycrystalline Bi thin films.** (a) XRD data confirming the (001) [hexagonal] // (111) [rhombohedral] texture of the investigated bismuth thin film (see also Supplementary Information). (b) Unit cell of elemental bismuth in hexagonal (green lines) and rhombohedral (blue lines) representation (not all atoms are shown). Red line represents the three-fold rotation symmetry axis. (c) High-field magnetoresistance data. An inset schematic shows the device under test and the direction of the applied magnetic field. (d) Temperature dependence of the third harmonic generated (THG) signal amplitude. Varying temperature from 4 K up to room temperature there is a less than 10% variation that can be ascribed to temperature drifts of the experimental setup. (e) bismuth film thickness dependence of the third harmonic generated (THG) signal amplitude, indicating that THG in Bi thin films originates from surface states. (f) Power spectrum of the THz THG measured of Bi/Au heterostructures. (g) Schematic of side jumps and skew scattering. Self-rotating surface Bloch electrons are deflected like the Magnus effect.

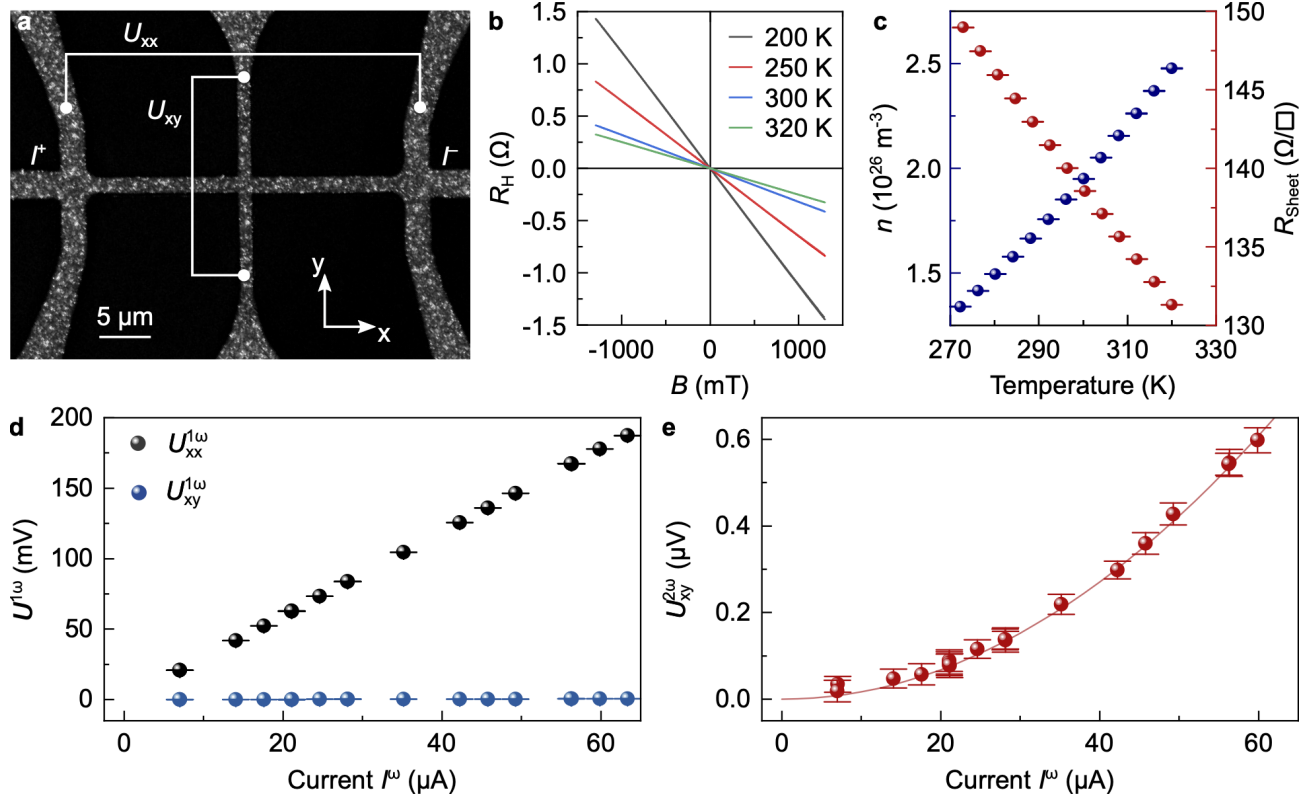


FIG. 2. **Magnetotransport and nonlinear Hall effect in Bi thin films.** (a) Electron microscopy image of a Hall cross device and schematic configuration of the transverse harmonic measurement. (b) Hall resistance R_H measured of an extended 100-nm-thick Bi film at selected temperatures. (c) Temperature evolution of the charge carriers density n and sheet resistance R_{Sheet} of the extended bismuth thin film. (d) First harmonic longitudinal $U_{xx}^{1\omega}$ and transverse $U_{xy}^{1\omega}$ voltages vs current amplitude measured of the Hall cross structures shown in panel (a). (e) Second harmonic transverse voltage $U_{xy}^{2\omega}$ vs current amplitude. Symbols correspond to the measured data and solid line is a quadratic fit $R_{yxx}^{2\omega} \cdot I^2$, where $R_{yxx}^{2\omega}$ is the nonlinear transverse resistance. Harmonic transport measurements are carried out at the fundamental frequency of 787 Hz.

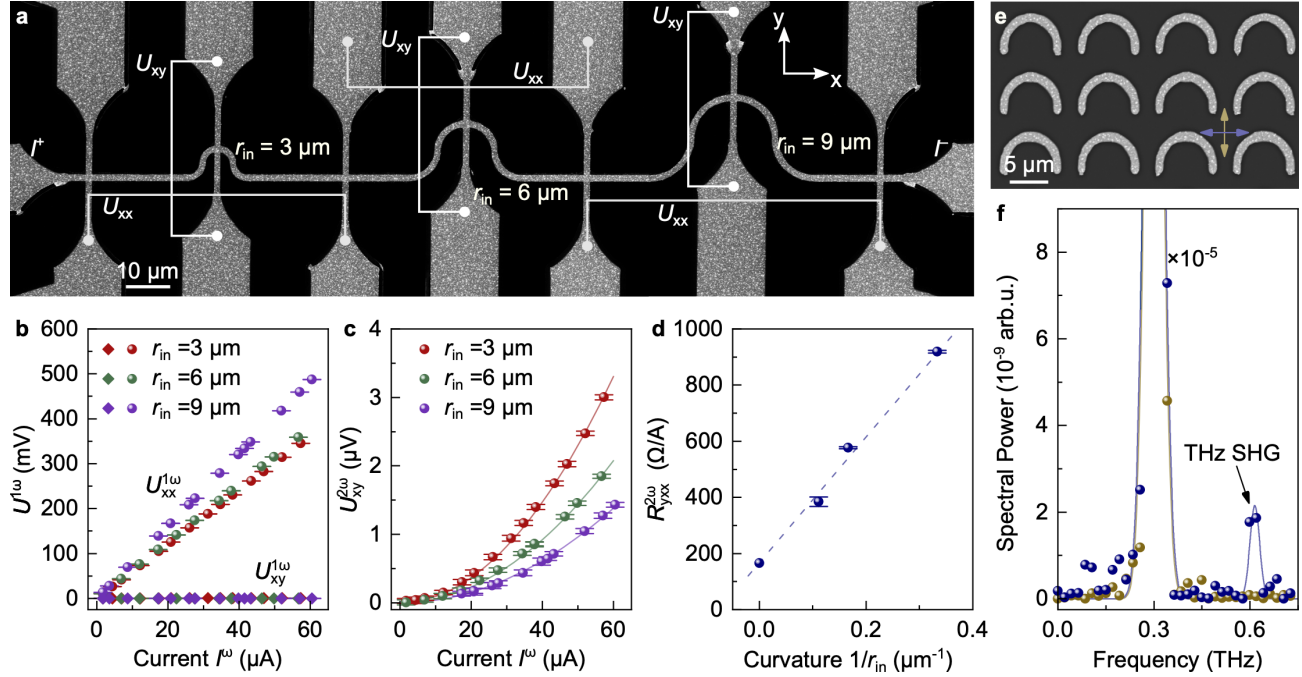


FIG. 3. Geometric nonlinear Hall effect in arc-shaped bismuth Hall bars. (a) Electron microscopy image of the Hall bar device with curved longitudinal channels of different inner radii ($R_{in} = 3 \mu\text{m}$, $6 \mu\text{m}$, $9 \mu\text{m}$) and width $1.4 \mu\text{m}$. The schematics show the configuration of transverse harmonic measurement at each arc-shaped Hall bar. (b) First harmonic longitudinal $U_{xx}^{1\omega}$ and transverse $U_{xy}^{1\omega}$ voltages vs current amplitude measured at each of arc-shaped Halls bars. (c) Second harmonic transverse $U_{xy}^{2\omega}$ voltages vs current amplitude. Symbols correspond to the measured data and solid lines are quadratic fit $R_{yxx}^{2\omega} \cdot I^2$. Harmonic transport measurements are carried out at the fundamental frequency of 787 Hz. (d) Scaling of the nonlinear transverse resistance $R_{yxx}^{2\omega}$ with the inverse inner radius R_{in} of the arc structures. Zero curvature corresponds to the data of the bismuth cross shown in Fig. 2(e). Dashed line is guide to the eye. (e) Electron microscopy image of an array of 100-nm-thick bismuth arcs (inner radius: $3 \mu\text{m}$; width: $1.2 \mu\text{m}$) used for THz second harmonic generation (SHG) measurement. Arrows indicate relative polarization of the incident THz radiation. (f) Transmitted spectral power of the THz signal measured of the sample shown in panel (e). A peak at 0.6 THz indicates generation of the second harmonic signal (fundamental THz frequency is 0.3 THz). The color of the lines in panel (f) corresponds to the color of the arrows in panel (e), indicating the polarization of the incident THz pulse. Intensity of the fundamental beam is suppressed by bandpass filters located between the sample and the detector. The background for each curve is also suppressed by subtracting measurements done in antiparallel polarization of THz pulse relative to the symmetry axis of the arcs, *i.e.* $0 - 180^\circ$ and $90 - 270^\circ$.

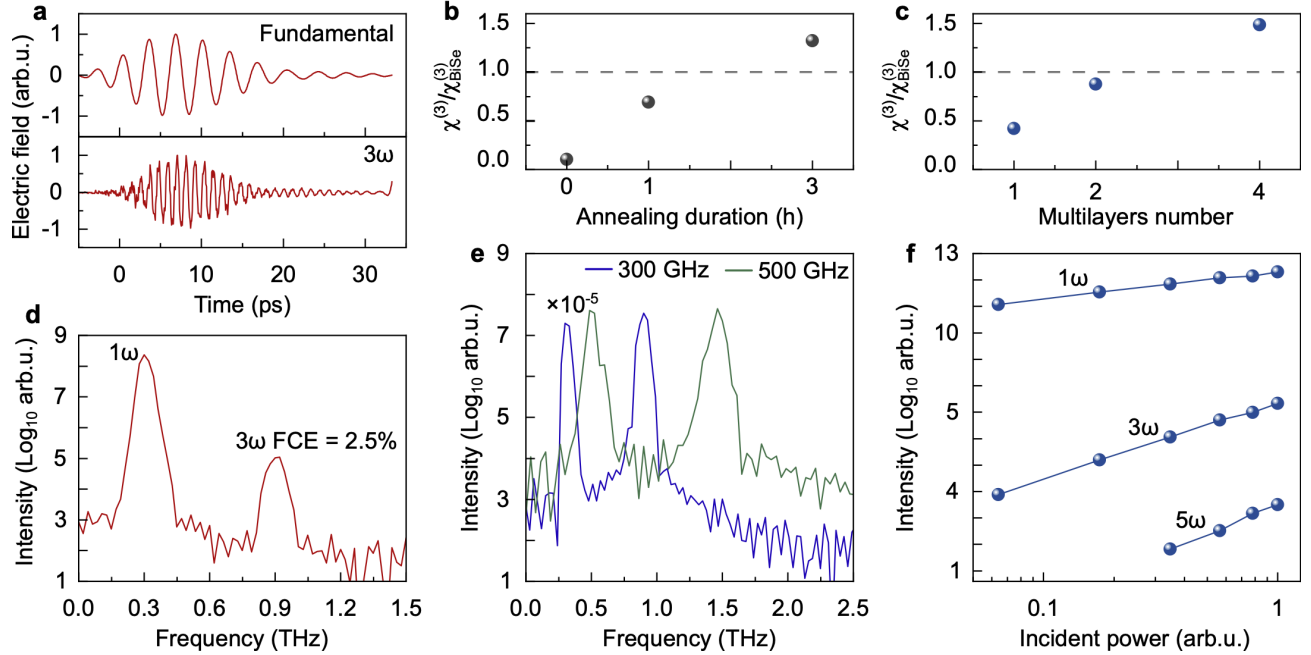


FIG. 4. **Highly-efficient and tunable THz high harmonic generation in bismuth-based systems.** (a) Time-domain dynamics of the THz light at fundamental frequency $\omega = 300$ GHz (top panel) and generated 3ω signal (bottom panel) measured through electro-optic sampling taken after Bi(100 nm)/Au(2 nm) thin film was annealed at 200°C for 3 h. (b) Tailoring the efficiency of the THz THG in Bi(100 nm)/Au(2 nm) thin films by thermal annealing in vacuum at 200°C. (c) Tailoring the efficiency of the THz THG in Bi/Au heterostructures: #1 = Bi(100 nm)/Au(2 nm), #2 = [Bi(50 nm)/Au(4 nm)]₂, #4 = [Bi(25 nm)/Au(2 nm)]₄. (d) Transmitted spectral power of the THz signal taken from the Bi(100 nm)/Au(2 nm) thin film annealed at 200°C for 3 h. The corresponding time-domain data is shown in panel (a). Here, no band-pass filter was applied during measurement. The data reveal high field conversion efficiency (FCE) of the THz THG at 2.5%. (e) Intensity of the transmitted signal taken of the Bi(100 nm)/Au(2 nm) thin film exposed to the THz light at fundamental frequency of 300 GHz and 500 GHz. (f) Spectral power of the 1st, 3rd and 5th harmonics measured in [Bi(25 nm)/Au(2 nm)]₄ heterostructure. The fundamental frequency of the incident light is 300 GHz. In panels (b) and (c), the plots show the third-order susceptibility $\chi^{(3)}$ measured in Bi samples normalized to the efficiency of the THz THG in epitaxially grown 100-nm-thick Bi₂Se₃ films [45].

METHODS

Sample fabrication

For transport characterization, thin films of bismuth with nominal thickness of 100 nm were deposited onto thermally oxidized 0.5-mm-thick Si with a 500-nm-thick SiO_x layer (CrysTec GmbH, Germany) and mechanically flexible Kapton polymer foils of 25- μ m thickness (DuPont, USA). For THz THG and FHG characterization, the samples were grown on SiO₂ quartz glass substrates (CrysTec GmbH, Germany) and capped with a 2-nm-thick Au layer to prevent oxidation. It is known that gold thin films do not contribute to THz high-harmonic generation. Some of the Bi(100 nm)/Au(2 nm) thin films were annealed in vacuum (below 10^{-3} mbar) at 200°C for 1 h and 3 h to investigate the effect of microstructure on THz THG. Furthermore, to study scaling of THz THG efficiency with the number of bismuth interfaces we prepared [Bi(50 nm)/Au(4 nm)]₂ and [Bi(25 nm)/Au(2 nm)]₄ heterostructures. To investigate the nonlinear Hall effect in Pt thin films, we prepared Hall crosses of 5-nm-thick Pt on Si/SiO_x(500 nm) substrates. To investigate THz SHG, we prepared extended array of arcs of 100-nm-thick Bi thin films and 20-nm-thick Au thin films on high purity silicon substrates. The arcs for THz studies were fabricated of 100-nm-thick Bi and 20-nm-thick Au thin films and had inner radius of 3 μ m and width of 1.2 μ m. To study scaling of the geometric nonlinear Hall effect in arc-shaped Hall bars, we lithographically patterned 100-nm-thick Bi thin film to obtain a sample accommodating three arcs of different inner radius of 3, 6, 9 μ m and width of 1.4 μ m. The deposition was done using RF magnetron sputtering at room temperature (base pressure: better than 10^{-7} mbar; Ar sputter pressure: 10^{-3} mbar; deposition rate: 0.3 nm/s). Hall cross devices were prepared using conventional optical lithography and lift-off process. The substrate was pre-baked at 120°C for 5 min and surface cleaned in oxygen plasma for 3 min. TiPrime adhesion promoter (MicroChemicals GmbH, Germany) was spin coated at 3000 rpm and soft baked at 115°C for 3 min. Image reversal photoresist AZ5214e (MicroChemicals GmbH, Germany) was spin coated at 6000 rpm for 30 s and soft baked on a hot plate at 100°C for 90 s. The samples were exposed using direct laser writer (DWL66, Heidelberg Instruments, Germany), post-baked at 115°C for 90 s and developed in 1 : 4 solution of AZ351b developer (MicroChemicals GmbH, Germany) in deionized (DI) water. After thin film deposition, extra material was lifted-off in acetone to reveal the device structure and rinsed with isopropanol and DI water. For transport characterization, to prevent oxidation of bismuth surface layers, the devices were covered with GE-varnish (Oxford Instruments, UK).

X-ray diffraction

XRD studies were carried out using a Rigaku SmartLab 3 kW with a parallel beam of Cu- K_{α} radiation (wavelength: 1.542 Å). Lattice parameter refinement was performed with

SmartLab Studio II. Bismuth crystallites lateral size was estimated from the width of four most intense X-ray reflections using the Scherrer equation.

Electron microscopy

Scanning electron microscopy (SEM) imaging and electron backscatter diffraction (EBSD) were performed in a Zeiss NVision 40 SEM equipped with a field emission electron cathode and a Bruker EBSD system with an e-Flash HR+ detector. The acceleration voltage was set to 30 kV, the beam current to about 10 nA using a 120 μ m aperture. The EBSD detector resolution was set to 320×240 pixels and the exposure time to at least 6×17 ms per frame. EBSD mapping was done as a rectangular grid of 1000×750 points with a step size of 100 nm. The evaluation of the EBSD data was done with the Bruker EBSD software ESPRIT. To have high confidence on correct EBSD pattern indexation, the minimum number of indexed bands was set to 9 and the maximum mean angular deviation to 1.1° . These conditions resulted in indexation rates of 24% and 22% for the as-deposited and annealed samples, respectively. A manual review of the EBSD patterns revealed that mostly, the EBSD patterns are different between adjacent mapping points. Hence, the grain size is estimated to be about 100 nm or below, while the number of grains contributing to the mapping data is estimated to be of order 10^5 .

High-field magnetoresistance

Pulsed-field magnetoresistance measurements reported in Fig. 1(c) were performed at Dresden High Magnetic Field Laboratory, the large scale facility of the Helmholtz-Zentrum Dresden-Rossendorf. The measurement was carried out in the longitudinal geometry by 4-terminal method (current parallel to magnetic field). The sample was fed with AC current of 2 mA at a frequency of 13 kHz. The voltage was acquired by a digitizer at sampling rate of 1 MHz. The recorded waveforms were analyzed by a numerical lock-in software. Magnetic field was obtained by integrating the voltage induced in a calibrated pick-up coil located in the vicinity of the sample.

THz study

The experiments were performed at the Helmholtz-Zentrum Dresden-Rossendorf. One part of the experiments (Figs. 1(d), 3(f)) was performed with the THz accelerator-based facility TELBE, and another part of the experiments (Figs. 1(e), 1(f), 4(a-f)) was performed with THz pulses generated by a Ti:sapphire femtosecond laser system using a tilted pulse front technique. Linearly polarized THz pulses with fundamental frequency of 0.3 THz and 0.5 THz were used as an input driving field. The input THz beam was focused on the samples at normal incidence, and the transmitted THz waves were detected behind the sample. During measurements, the temperature of the sample was controlled us-

ing cryostat (OptistatCF-V) in vacuum. After transmission through the sample, the THz waves containing the remainder of the fundamental field, as well as the generated harmonics, were sent through a set of bandpass filters with the transmission band centered at the generated harmonic frequency. The THz field of higher harmonics was measured directly in the time domain by free-space electro-optic sampling (FEOS) in a 2 mm thick ZnTe crystal. For FEOS THz detection, we used synchronized optical probe pulses of 35 fs duration, central wavelength 800 nm. To measure the absolute value of the conversion efficiency of the THz field of higher harmonics, 100 μm GaP and no bandpass filters were used.

Magnetotransport and Sheet resistance

The magnetotransport measurements reported in Fig. 2(b) were carried out of an extended 100-nm-thick Bi thin film using the Zero-Offset Hall preset of a Tensormeter measurement device (Tensor Instruments, HZDR Innovation GmbH, Germany), which provides the absolute transverse resistance without any offset. Magnetic field was applied perpendicular to the film plane. Temperature control in the range of 270 K – 320 K was achieved using cryostat in vacuum. The charge carriers density was calculated assuming only electron conductivity as

$$n = \frac{1}{R_{\text{H}}tq},$$

where R_{H} – Hall resistance reported in Fig. 2(b), $t = 100$ nm – film thickness and q – electron charge. Temperature evolution of the sheet resistance (Fig. 2(c)) was measured of an extended 100-nm-thick Bi thin film in the classical van der Pauw configuration by placing 4 electrical contacts at the edges of the sample. This measurement geometry provides sheet resistance with a geometry factor = 1.

Harmonic transport measurement

Electrical transport harmonic measurements reported in the main text were performed using HF2LI Lock-in (Zurich Instruments, Switzerland). The sinusoidal current at the fundamental frequency of 787 Hz was sourced using internal generator. Amplitude and phase of the measured longitudinal and transverse voltages at fundamental frequency and second harmonic were recorded. For each sourcing current value, the data was averaged over one minute integration time. Metal shielding around the sample was used to minimize the influence of external RF parasitic signals. For comparison, in Supplementary Information, we report measurements taken with two other devices including Tensormeter RTM2 (Tensor Instruments, HZDR Innovation GmbH, Germany) and lock-in amplifier SR860 (Stanford Research Systems, USA).

We note that the compound (*i.e.*, including oscillator output and signal input) nonlinearity of our tested lock-in amplifiers (Stanford SR860 and Zurich HF2LI) poses a limit for the assessment of small harmonic distortions in the presence

of a large fundamental signals. This is of particular relevance for the detection of the second harmonic longitudinal voltage. The SR860 and HF2LI are medium to high frequency lock-in amplifiers with a reported total harmonic distortion of -80 dB (*i.e.* 4 orders of magnitude). As a result, we see a noise floor in the dominant harmonic distortion orders (*i.e.*, 2nd harmonic) that is approximately 10^{-4} of the first harmonic fundamental signal. This is evidenced even for the case of commercial surface mounted device (SMD) metal film resistors, where lock-ins show signal at the level of $20 \mu\text{V}$ at the second harmonic longitudinal voltage (Supplementary Fig. 13). As this noise can also scale with current, it can be mistaken for an actual harmonic distortion caused by the sample’s physics. We have validated the harmonic distortion signals in our data through the additional measurements with a Tensormeter RTM2 (Tensor Instruments, HZDR Innovation GmbH, Germany). While targeted at lower frequency range of below 50 kHz, this device offers an improved compound nonlinearity of max. 5 ppm, which is confirmed by measuring apparent harmonic distortions from a highly linear reference made of commercial resistors. This test reassures that harmonic distortion signals reported to be in excess of 10^{-6} and measured with the Tensormeter RTM2 originate from the studied samples. In particular, we report current-voltage curves of the longitudinal voltage at the second harmonic. The second harmonic signal of the longitudinal voltage is at the level of < 100 nV for Bi thin films (Supplementary Fig. 14) and for the reference SMD resistor (Supplementary Fig. 13).

DATA AVAILABILITY

All data that support the plots within this paper and other findings of this study are available from the corresponding authors upon reasonable request.

ACKNOWLEDGEMENTS

We thank Conrad Schubert (HZDR) for support with thin film deposition, Dr. Larysa Baraban (HZDR) for providing access to the measurement equipment for harmonic analysis, and Prof. Olav Hellwig (HZDR, TU Chemnitz) for providing access to the XRD tool. This research was carried out in part at the Ion Beam Center and ELBE large-scale facilities at the Helmholtz-Zentrum Dresden-Rossendorf e.V., member of the Helmholtz Association. We acknowledge the support of the Dresden High Magnetic Field Laboratory at the Helmholtz-Zentrum Dresden-Rossendorf e.V., member of the European Magnetic Field Laboratory (EMFL). This work is financed in part via the German Research Foundation (DFG) under Grants No. MA 5144/22-1, MA 5144/24-1, MA 5144/33-1, and European Commission Community Research and Development Information Service (project REGO; ID: 951887).

AUTHOR CONTRIBUTIONS

C.O. and D.M. developed the project idea. P.M. prepared samples and performed magnetotransport characterization with the support from Y.Z., T.K. and D.M. S.K., I.I., A.P., A.A., G.C.P., T.O., and J.-C.D. performed THz studies. P.C. carried out electron microscopy measurements. F.G. performed XRD measurements with support from I.V. C.O. developed theoretical description of the transport effects in Bi thin films. Y.S. carried out high-field magnetoresistance

measurements with the support from I.V. The manuscript was written by C.O., P.M. and D.M. with the contribution from S.K., T.K., I.I., A.P., P.C. Y.Z., I.V., Y.S., F.G, A.A., G.C.P., T.O., and J.-C.D..

COMPETING INTERESTS

The authors declare no competing interests.

-
- [1] I. Sodemann and L. Fu, Quantum nonlinear Hall effect induced by Berry curvature dipole in time-reversal invariant materials, *Phys. Rev. Lett.* **115**, 216806 (2015).
- [2] C. Ortix, Nonlinear Hall effect with time-reversal symmetry: Theory and material realizations, *Advanced Quantum Technologies* **4**, 2100056 (2021).
- [3] Z. Z. Du, H.-Z. Lu, and X. C. Xie, Nonlinear hall effects, *Nature Reviews Physics* **3**, 744 (2021).
- [4] D. Wawrzik, J. I. Facio, and J. van den Brink, Surface induced electronic berry curvature in bulk berry curvature free materials, *Materials Today Physics* **33**, 101027 (2023).
- [5] P. He, H. Isobe, D. Zhu, C.-H. Hsu, L. Fu, and H. Yang, Quantum frequency doubling in the topological insulator Bi_2Se_3 , *Nature Communications* **12**, 698 (2021).
- [6] S.-C. Zhang, X. Dai, X.-L. Qi, C.-X. Liu, H. Zhang, and Z. Fang, Topological insulators in Bi_2Se_3 , Bi_2Te_3 and Sb_2Te_3 with a single Dirac cone on the surface, *Nature Physics* **5**, 438 (2009).
- [7] Z. Z. Du, C. M. Wang, S. Li, H.-Z. Lu, and X. C. Xie, Disorder-induced nonlinear Hall effect with time-reversal symmetry, *Nature Communications* **10**, 3047 (2019).
- [8] C. Xiao, Z. Z. Du, and Q. Niu, Theory of nonlinear Hall effects: Modified semiclassics from quantum kinetics, *Phys. Rev. B* **100**, 165422 (2019).
- [9] J. Orenstein, J. Moore, T. Morimoto, D. Torchinsky, J. Harter, and D. Hsieh, Topology and symmetry of quantum materials via nonlinear optical responses, *Annual Review of Condensed Matter Physics* **12**, 247 (2021).
- [10] Y. Zhang and L. Fu, Terahertz detection based on nonlinear hall effect without magnetic field, *Proceedings of the National Academy of Sciences* **118**, e2100736118 (2021), <https://www.pnas.org/doi/pdf/10.1073/pnas.2100736118>.
- [11] H. Isobe, S.-Y. Xu, and L. Fu, High-frequency rectification via chiral bloch electrons, *Science Advances* **6**, 10.1126/sciadv.aay2497 (2020).
- [12] D. Kumar, C.-H. Hsu, R. Sharma, T.-R. Chang, P. Yu, J. Wang, G. Eda, G. Liang, and H. Yang, Room-temperature nonlinear Hall effect and wireless radiofrequency rectification in Weyl semimetal TaIrTe_4 , *Nature Nanotechnology* 10.1038/s41565-020-00839-3 (2021).
- [13] L. Min, H. Tan, Z. Xie, L. Miao, R. Zhang, S. H. Lee, V. Gopalan, C.-X. Liu, N. Alem, B. Yan, and Z. Mao, Strong room-temperature bulk nonlinear hall effect in a spin-valley locked dirac material, *Nature Communications* **14**, 364 (2023).
- [14] S.-Y. Xu, Q. Ma, H. Shen, V. Fatemi, S. Wu, T.-R. Chang, G. Chang, A. M. M. Valdivia, C.-K. Chan, Q. D. Gibson, J. Zhou, Z. Liu, K. Watanabe, T. Taniguchi, H. Lin, R. J. Cava, L. Fu, N. Gedik, and P. Jarillo-Herrero, Electrically switchable Berry curvature dipole in the monolayer topological insulator WTe_2 , *Nature Physics* **14**, 900 (2018).
- [15] J.-S. You, S. Fang, S.-Y. Xu, E. Kaxiras, and T. Low, Berry curvature dipole current in the transition metal dichalcogenides family, *Phys. Rev. B* **98**, 121109 (2018).
- [16] Y. Zhang, J. van den Brink, C. Felser, and B. Yan, Electrically tuneable nonlinear anomalous Hall effect in two-dimensional transition-metal dichalcogenides WTe_2 and MoTe_2 , *2D Materials* **5**, 044001 (2018).
- [17] Z. Z. Du, C. M. Wang, H.-Z. Lu, and X. C. Xie, Band signatures for strong nonlinear Hall effect in bilayer WTe_2 , *Phys. Rev. Lett.* **121**, 266601 (2018).
- [18] J. Son, K.-H. Kim, Y. H. Ahn, H.-W. Lee, and J. Lee, Strain engineering of the berry curvature dipole and valley magnetization in monolayer mos_2 , *Phys. Rev. Lett.* **123**, 036806 (2019).
- [19] Q. Ma, S.-Y. Xu, H. Shen, D. MacNeill, V. Fatemi, T.-R. Chang, A. M. Mier Valdivia, S. Wu, Z. Du, C.-H. Hsu, S. Fang, Q. D. Gibson, K. Watanabe, T. Taniguchi, R. J. Cava, E. Kaxiras, H.-Z. Lu, H. Lin, L. Fu, N. Gedik, and P. Jarillo-Herrero, Observation of the nonlinear Hall effect under time-reversal-symmetric conditions, *Nature* **565**, 337 (2019).
- [20] K. Kang, T. Li, E. Sohn, J. Shan, and K. F. Mak, Nonlinear anomalous Hall effect in few-layer WTe_2 , *Nature Materials* **18**, 324 (2019).
- [21] S. Singh, J. Kim, K. M. Rabe, and D. Vanderbilt, Engineering Weyl phases and nonlinear Hall effects in T_d - MoTe_2 , *Phys. Rev. Lett.* **125**, 046402 (2020).
- [22] T. Ma, H. Chen, K. Yananose, X. Zhou, L. Wang, R. Li, Z. Zhu, Z. Wu, Q.-H. Xu, J. Yu, C. W. Qiu, A. Stroppa, and K. P. Loh, Growth of bilayer mote_2 single crystals with strong non-linear hall effect, *Nature Communications* **13**, 5465 (2022).
- [23] R. Battilomo, N. Scopigno, and C. Ortix, Berry curvature dipole in strained graphene: A Fermi surface warping effect, *Phys. Rev. Lett.* **123**, 196403 (2019).
- [24] S.-C. Ho, C.-H. Chang, Y.-C. Hsieh, S.-T. Lo, B. Huang, T.-H.-Y. Vu, C. Ortix, and T.-M. Chen, Hall effects in artificially corrugated bilayer graphene without breaking time-reversal symmetry, *Nature Electronics* **4**, 116 (2021).
- [25] E. Lesne, Y. G. Sağlam, R. Battilomo, M. T. Mercaldo, T. C. van Thiel, U. Filippozzi, C. Noce, M. Cuoco, G. A. Steele, C. Ortix, and A. D. Caviglia, Designing spin and orbital sources of berry curvature at oxide interfaces, *Nature Materials* **22**, 576 (2023).
- [26] Y. M. Koroteev, G. Bihlmayer, E. V. Chulkov, and S. Blügel, First-principles investigation of structural and electronic properties of ultrathin bi films, *Phys. Rev. B* **77**, 045428 (2008).
- [27] H. Du, X. Sun, X. Liu, X. Wu, J. Wang, M. Tian, A. Zhao, Y. Luo, J. Yang, B. Wang, and J. G. Hou, Surface landau levels and spin states in bismuth (111) ultrathin films, *Nature Com-*

- munications **7**, 10814 (2016).
- [28] R. Mohan, Green bismuth, *Nature Chemistry* **2**, 336 (2010).
- [29] P. Gentile, M. Cuoco, O. M. Volkov, Z.-J. Ying, I. J. Vera-Marun, D. Makarov, and C. Ortix, Electronic materials with nanoscale curved geometries, *Nature Electronics* **5**, 551 (2022).
- [30] N. B. Schade, D. I. Schuster, and S. R. Nagel, A nonlinear, geometric hall effect without magnetic field, *Proceedings of the National Academy of Sciences* **116**, 24475 (2019), <https://www.pnas.org/doi/pdf/10.1073/pnas.1916406116>.
- [31] R. Battilomo, N. Scopigno, and C. Ortix, Anomalous planar Hall effect in two-dimensional trigonal crystals, *Phys. Rev. Research* **3**, L012006 (2021).
- [32] Z. Zhu, J. Wang, H. Zuo, B. Fauqué, R. D. McDonald, Y. Fuseya, and K. Behnia, Emptying dirac valleys in bismuth using high magnetic fields, *Nature Communications* **8**, 15297 (2017).
- [33] A. A. Abrikosov, Quantum magnetoresistance, *Phys. Rev. B* **58**, 2788 (1998).
- [34] S. Kovalev, K. J. Tielrooij, J. C. Deinert, I. Ilyakov, N. Awari, M. Chen, A. Ponomaryov, M. Bawatna, T. V. A. G. de Oliveira, L. M. Eng, K. A. Kuznetsov, D. A. Safronenkov, G. K. Kitaeva, P. I. Kuznetsov, H. A. Hafez, D. Turchinovich, and M. Gensch, Terahertz signatures of ultrafast dirac fermion relaxation at the surface of topological insulators, *npj Quantum Materials* **6**, 84 (2021).
- [35] F. Giorgianni, E. Chiadroni, A. Rovere, M. Cestelli-Guidi, A. Perucchi, M. Bellaveglia, M. Castellano, D. Di Giovenale, G. Di Pirro, M. Ferrario, R. Pompili, C. Vaccarezza, F. Villa, A. Cianchi, A. Mostacci, M. Petrarca, M. Brahlek, N. Koirala, S. Oh, and S. Lupi, Strong nonlinear terahertz response induced by dirac surface states in Bi_2Se_3 topological insulator, *Nature Communications* **7**, 11421 (2016).
- [36] S. Kovalev, H. A. Hafez, K.-J. Tielrooij, J.-C. Deinert, I. Ilyakov, N. Awari, D. Alcaraz, K. Soundarapandian, D. Saleta, S. Germanskiy, M. Chen, M. Bawatna, B. Green, F. H. L. Koppens, M. Mittendorff, M. Bonn, M. Gensch, and D. Turchinovich, Electrical tunability of terahertz non-linearity in graphene, *Science Advances* **7**, eabf9809 (2021), <https://www.science.org/doi/pdf/10.1126/sciadv.abf9809>.
- [37] S. Kovalev, R. M. A. Dantas, S. Germanskiy, J.-C. Deinert, B. Green, I. Ilyakov, N. Awari, M. Chen, M. Bawatna, J. Ling, F. Xiu, P. H. M. van Loosdrecht, P. Surówka, T. Oka, and Z. Wang, Non-perturbative terahertz high-harmonic generation in the three-dimensional dirac semimetal Cd_3As_2 , *Nature Communications* **11**, 2451 (2020).
- [38] F. Schindler, Z. Wang, M. G. Vergniory, A. M. Cook, A. Murani, S. Sengupta, A. Y. Kasumov, R. Deblock, S. Jeon, I. Drozdov, H. Bouchiat, S. Guéron, A. Yazdani, B. A. Bernevig, and T. Neupert, Higher-order topology in bismuth, *Nature Physics* **14**, 918 (2018).
- [39] L. Fu and C. L. Kane, Topological insulators with inversion symmetry, *Phys. Rev. B* **76**, 045302 (2007).
- [40] A. Altland and M. R. Zirnbauer, Nonstandard symmetry classes in mesoscopic normal-superconducting hybrid structures, *Phys. Rev. B* **55**, 1142 (1997).
- [41] L. Fu, Hexagonal warping effects in the surface states of the topological insulator Bi_2Te_3 , *Phys. Rev. Lett.* **103**, 266801 (2009).
- [42] P. Zubko, G. Catalan, and A. K. Tagantsev, Flexoelectric effect in solids, *Annual Review of Materials Research* **43**, 387 (2013), <https://doi.org/10.1146/annurev-matsci-071312-121634>.
- [43] Y. Wen, F. Giorgianni, I. Ilyakov, B. Quan, S. Kovalev, C. Wang, C. Vicario, J.-C. Deinert, X. Xiong, J. Bailey, M. Chen, A. Ponomaryov, N. Awari, A. Rovere, J. Sun, R. Morandotti, L. Razzari, G. Aeppli, J. Li, and J. Zhou, A universal route to efficient non-linear response via Thomson scattering in linear solids, *National Science Review* **10**, nwad136 (2023), <https://academic.oup.com/nsr/article-pdf/10/7/nwad136/50768156/nwad136.pdf>.
- [44] B. Yan, B. Stadtmüller, N. Haag, S. Jakobs, J. Seidel, D. Jungkenn, S. Mathias, M. Cinchetti, M. Aeschlimann, and C. Felser, Topological states on the gold surface, *Nature Communications* **6**, 10167 (2015).
- [45] K.-J. Tielrooij, A. Principi, D. S. Reig, A. Block, S. Varghese, S. Schreyeck, K. Brunner, G. Karczewski, I. Ilyakov, O. Ponomaryov, T. V. A. G. de Oliveira, M. Chen, J.-C. Deinert, C. G. Carbonell, S. O. Valenzuela, L. W. Molenkamp, T. Kiessling, G. V. Astakhov, and S. Kovalev, Milliwatt terahertz harmonic generation from topological insulator metamaterials, *Light: Science & Applications* **11**, 315 (2022).
- [46] A. Principi and K.-J. Tielrooij, Ultrafast electronic heat dissipation through surface-to-bulk coulomb coupling in quantum materials, *Phys. Rev. B* **106**, 115422 (2022).
- [47] F. Y. Yang, K. Liu, K. Hong, D. H. Reich, P. C. Searson, and C. L. Chien, Large magnetoresistance of electrodeposited single-crystal bismuth thin films, *Science* **284**, 1335 (1999).
- [48] M. Melzer, J. I. Mönch, D. Makarov, Y. Zabala, G. S. Cañón Bermúdez, D. Karnaushenko, S. Baunack, F. Bahr, C. Yan, M. Kaltenbrunner, and O. G. Schmidt, Wearable magnetic field sensors for flexible electronics, *Advanced Materials* **27**, 1274 (2015).
- [49] E. S. Oliveros-Mata, C. Voigt, G. S. Cañón Bermúdez, Y. Zabala, N. M. Valdez-Garduño, M. Fritsch, S. Mosch, M. Kusnezoff, J. Fassbender, M. Vinnichenko, and D. Makarov, Dispenser printed bismuth-based magnetic field sensors with non-saturating large magnetoresistance for touchless interactive surfaces, *Advanced Materials Technologies* **7**, 2200227 (2022).
- [50] P. Corbae, S. Ciocys, D. Varjas, E. Kennedy, S. Zeltmann, M. Molina-Ruiz, S. M. Griffin, C. Jozwiak, Z. Chen, L.-W. Wang, A. M. Minor, M. Scott, A. G. Grushin, A. Lanzara, and F. Hellman, Observation of spin-momentum locked surface states in amorphous Bi_2Se_3 , *Nature Materials* **22**, 200 (2023).
- [51] A. Tiwari, F. Chen, S. Zhong, E. Druke, J. Koo, A. Kaczmarek, C. Xiao, J. Gao, X. Luo, Q. Niu, Y. Sun, B. Yan, L. Zhao, and A. W. Tsen, Giant c-axis nonlinear anomalous hall effect in td-mote_2 and wte_2 , *Nature Communications* **12**, 2049 (2021).
- [52] P. He, G. K. W. Koon, H. Isobe, J. Y. Tan, J. Hu, A. H. C. Neto, L. Fu, and H. Yang, Graphene moiré superlattices with giant quantum nonlinearity of chiral Bloch electrons, *Nature Nanotechnology* **17**, 378 (2022).

**Supplementary Information:
Tunable room temperature nonlinear Hall effect
from the surfaces of elementary bismuth thin films**

Pavlo Makushko,¹ Sergey Kovalev,² Yevhen Zabala,^{1,3} Igor Ilyakov,² Alexey Ponomaryov,² Atiqah Arshad,²
Gulloo Lal Prajapati,² Thales V. A. G. de Oliveira,² Jan-Christoph Deinert,² Paul Chekhonin,^{1,4}
Igor Veremchuk,¹ Tobias Kosub,¹ Yurii Skourski,⁵ Fabian Ganss,¹ Denys Makarov,^{1,*} and Carmine Ortix^{6,†}

¹*Helmholtz-Zentrum Dresden-Rossendorf e.V., Institute of Ion Beam Physics and Materials Research, 01328 Dresden, Germany*

²*Helmholtz-Zentrum Dresden-Rossendorf e.V., Institute of Radiation Physics, 01328 Dresden, Germany*

³*The H. Niewodniczanski Institute of Nuclear Physics,
Polish Academy of Sciences, 31-342 Krakow, Poland*

⁴*Helmholtz-Zentrum Dresden-Rossendorf e.V., Institute of Resource Ecology, 01328 Dresden, Germany*

⁵*Helmholtz-Zentrum Dresden-Rossendorf e.V., Dresden High*

Magnetic Field Laboratory (HLD-EMFL), 01328 Dresden, Germany

⁶*Dipartimento di Fisica "E. R. Caianiello", Università di Salerno, IT-84084 Fisciano (SA), Italy*

CONTENTS

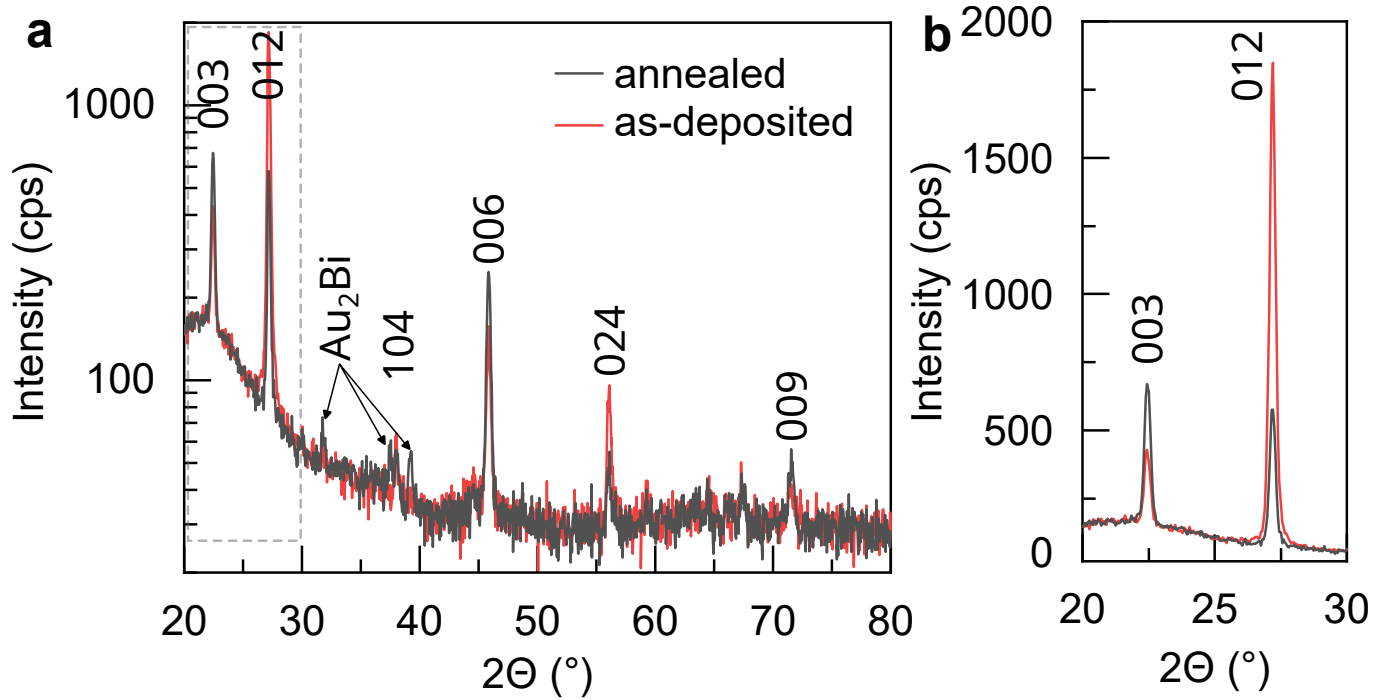
I. Supplementary structural characterization	2
A. X-ray diffraction data	2
B. Electron microscopy characterization	4
II. Supplementary Theory Notes	6
A. Electronic properties and Berry curvature at the Bi (1 1 1) surface states	6
B. Second-order scattering rate and transport scattering time	7
C. Third-order scattering rate and skew contribution to the nonlinear Hall effect	9
D. Coordinate shift and side jump contributions to the nonlinear Hall effect	11
E. Symmetry constraints on the nonlinear conductivity tensor	13
F. On the difference between dissipative and dissipationless (non)linear transverse electrical responses.	15
G. Scaling of the nonlinear Hall effect in Bi thin films	16
H. Thermal effects in bismuth thin films due to charge current	18
III. Supplementary THz high harmonic generation measurements	20
A. THz fifth harmonic generation in Bi thin films	20
B. THz third harmonic generation in Bi/Au heterostructures	21
C. Bismuth film thickness dependence of the THz third harmonic generation	22
D. Effect of thermal annealing on THz third harmonic generation	23
E. Optical second-harmonic generation at THz frequencies in curved devices	24
IV. Supplementary transport characterization	26
A. Harmonic transport measurement of a reference resistor	26
B. Harmonic transport measurement of Bi thin films on polymeric foils	27
C. Harmonic transport measurements of Bi Hall crosses using different devices	28
D. Harmonic transport measurements of arc-shaped Bi Hall bars using different devices	29
E. Harmonic transport measurements of Pt Hall crosses using different devices	30
V. Fundamental achievements of this work and their potential technological implications	31
References	32

* d.makarov@hzdr.de

† cortix@unisa.it

I. SUPPLEMENTARY STRUCTURAL CHARACTERIZATION

A. X-ray diffraction data

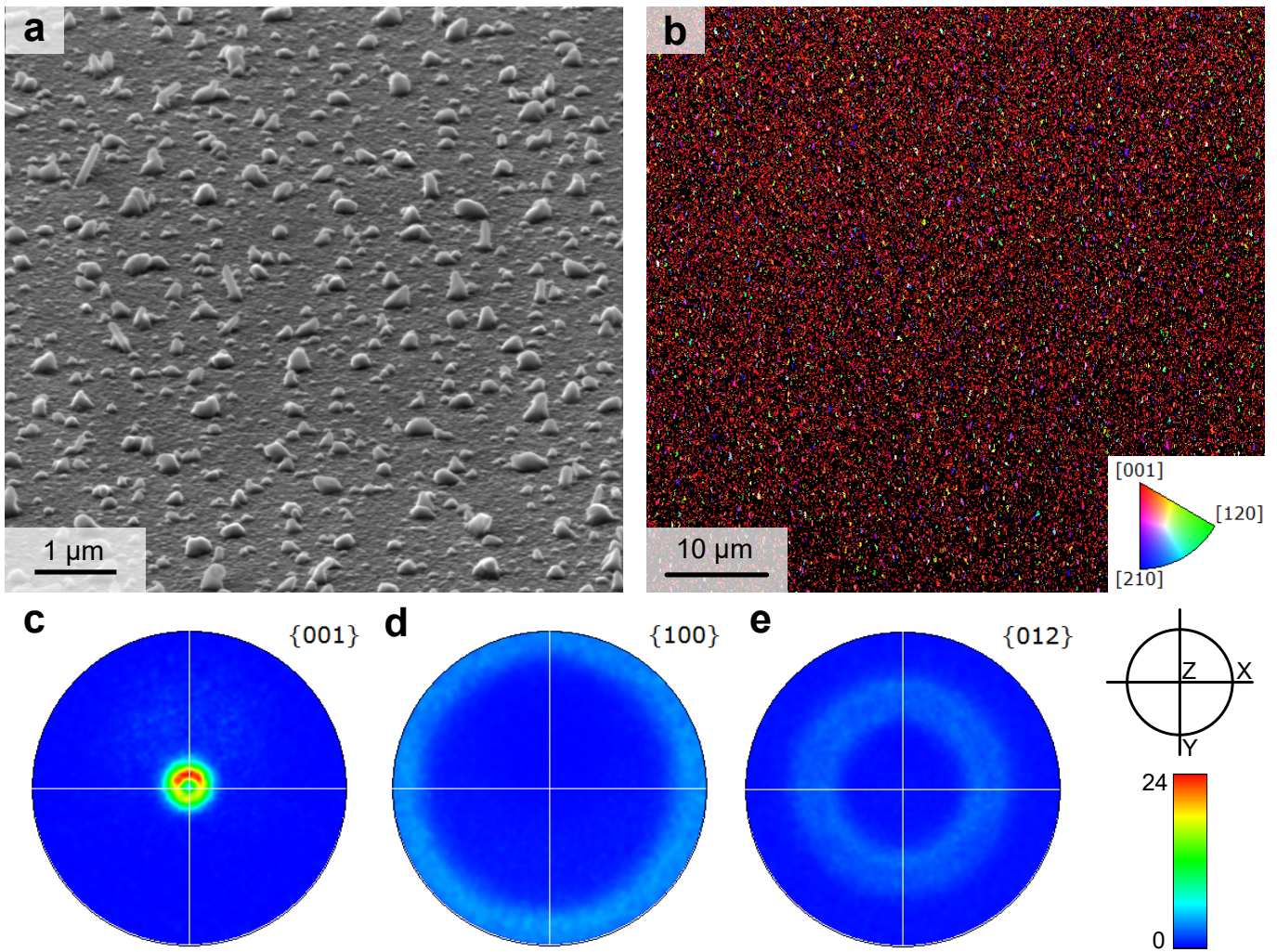


Supplementary Fig. 1. **Structural characterization of 100-nm-thick Bi thin films.** X-ray diffraction (XRD) patterns of the Bi(100 nm)/Au(2 nm) thin films. As-deposited thin film reveals high intensity of (003) and (006) reflections, indicating the presence of (001) texture. Vacuum annealing at 200°C enhances the (001) texture, in line with the increase of the ratio between (003) and (012) reflections. XRD data do not reveal the presence of the Au layer in the as-deposited sample due to low amount of material (only 2 nm). After annealing, low intensity peak of maldonite Au_2Bi appears, indicating thermally induced reaction of the gold capping layer with bismuth.

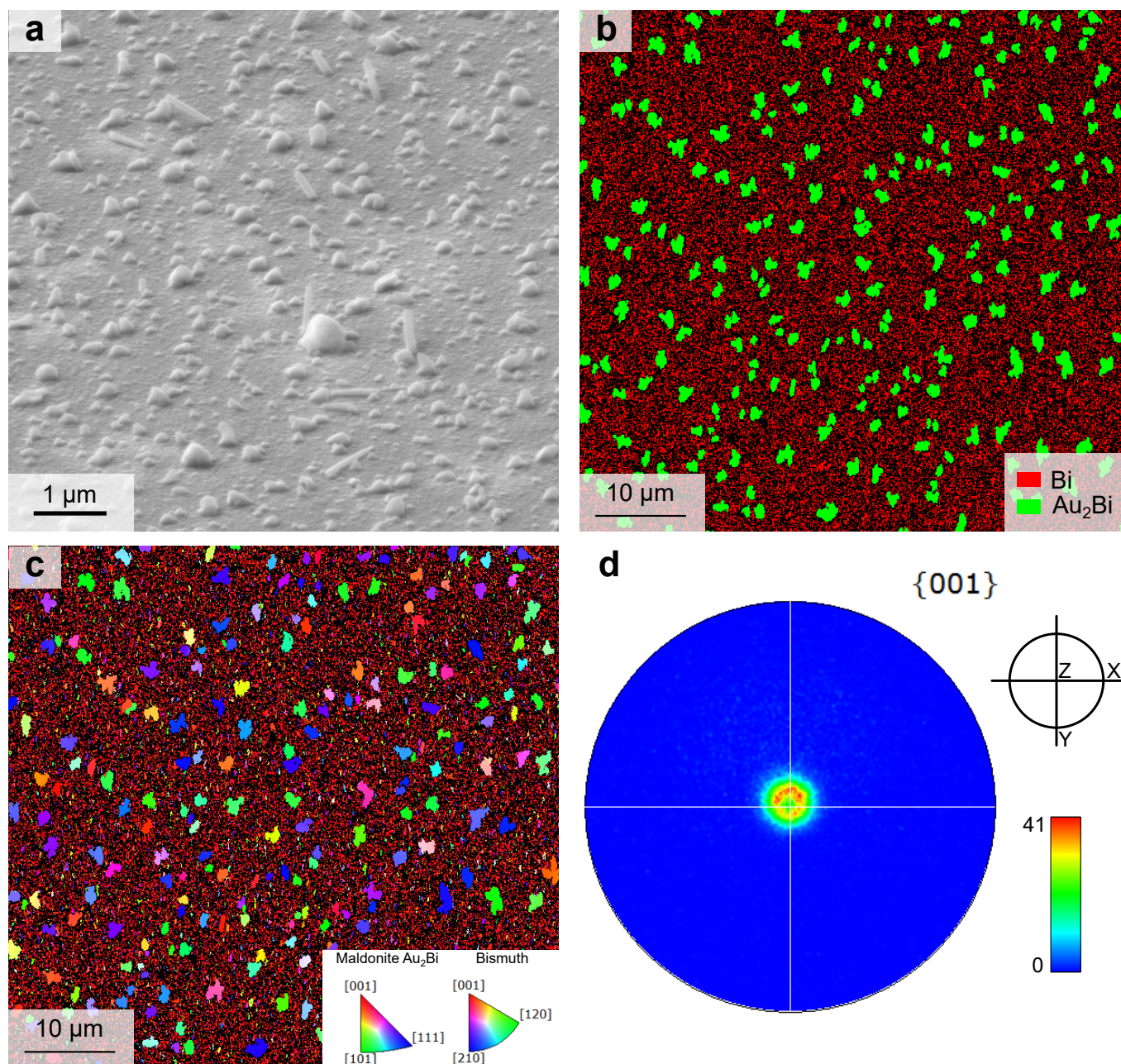
TABLE I. **Summary of the XRD data.** Lattice parameters, ratio of the integral intensity of XRD reflections and average grain size, estimated based on the Scherrer equation. Lattice parameters of bismuth in our thin films are close to ones for bulk material, indicating the absence of residual mechanical stresses in our thin films. Vacuum annealing enhances the (00 l) texture, retaining the microstructure of the samples (lattice parameters and grain size) unchanged.

Sample	a , Å	c , Å	I_{003}/I_{012}	I_{006}/I_{024}	Grain size, nm
PDF database	4.54(7)	11.86(2)	6%	86%	–
as-deposited	4.54	11.89	13%	137%	33
200°C 3 h	4.54	11.87	93%	972%	34

B. Electron microscopy characterization



Supplementary Fig. 2. **Microstructure characterization of the as-deposited 100-nm-thick Bi thin film.** (a) High-resolution SEM secondary electron image of the sample surface (the sample is tilted by 70°). (b) Inverse pole figure for the thin film normal direction (Z), colors show crystallographic direction $[h k l]$, which is parallel to the sample surface normal according to key figure. (c-e) Pole figures for selected crystallographic planes calculated from the EBSD data. The data indicate preferred (001) fiber texture in the thin film. The film is in-plane structurally isotropic.



Supplementary Fig. 3. **Microstructure characterization of the 100-nm-thick Bi thin film after annealing at 200°C for 3 h.** (a) High-resolution SEM secondary electron image of the sample surface (the sample is tilted by 70°). (b) Phase map measured at the top surface of the thin film. Upon annealing, the 2-nm-thick gold layer reacted with bismuth (red) and formed islands of maldonite Au_2Bi phase (green). (c) Inverse pole figure map for the thin film normal direction (Z) for both Bi and Au_2Bi phases. Colors show crystallographic direction $[hkl]$, which is parallel to the sample surface normal according to the respective key figures. (d) Pole figure for the $\{001\}$ plane in bismuth calculated from the EBSD data. The figures indicate the presence of a (001) fiber texture in bismuth and random texture for maldonite grains.

II. SUPPLEMENTARY THEORY NOTES

A. Electronic properties and Berry curvature at the Bi (111) surface states

Here, we derive the electronic properties of the (111) surface states of Bismuth using symmetry principles. We recall that in the remainder we use the rhombohedral notation for the crystal structure. Previous density functional theory calculations have shown that surface states in Bi are centered at the $\bar{\Gamma}$ point of the surface Brillouin zone. The minimal model Hamiltonian close to the surface effective spin- $\frac{1}{2}$ Kramers' doublet can be derived in a $\mathbf{k} \cdot \mathbf{p}$ expansion accounting for all symmetry-allowed terms. To do so, we note that in the surface Kramers' doublet basis, the time-reversal symmetry can be represented as $\mathcal{T} = i\sigma_y \mathcal{K}$ with \mathcal{K} the complex conjugation. The vertical mirror symmetry can be represented by $\mathcal{M} = i\sigma_x$. In the basis $|\psi^{\uparrow\downarrow}\rangle$, the threefold rotation operator takes the form $\mathcal{C}_3 = e^{-i\sigma_z \pi/3}$. Under the operation of \mathcal{C}_3 and \mathcal{M} , momentum and spin transform as follows,

$$\begin{aligned} \mathcal{C}_3 : & & k_{\pm} & \rightarrow e^{\pm i2\pi/3} k_{\pm}, & \sigma_{\pm} & \rightarrow e^{\pm i2\pi/3} \sigma_{\pm}, & \sigma_z & \rightarrow \sigma_z \\ \mathcal{M} : & & k_+ & \rightarrow -k_- & \sigma_x & \rightarrow \sigma_x, & \sigma_{y,z} & \rightarrow -\sigma_{y,z} \end{aligned}$$

where $k_{\pm} = k_x \pm ik_y$ and $\sigma_{\pm} = \sigma_x \pm i\sigma_y$. The Hamiltonian must also be invariant under time reversal, which adds the constraint $\mathcal{H}(\mathbf{k}) = \mathcal{T}\mathcal{H}(-\mathbf{k})\mathcal{T}^{-1} = \sigma_y \mathcal{H}^*(-\mathbf{k})\sigma_y$.

At linear order in the momentum \mathbf{k} , the minimal two-band Hamiltonian for a Kramers' related pair of bands corresponds to a Dirac cone:

$$\mathcal{H}_{\text{TI}}(\mathbf{k}) = \hbar v_F (\sigma_x k_y - \sigma_y k_x) \quad (1)$$

where v_F is the Fermi velocity. The Hamiltonian above does not capture crystalline anisotropy effects. The first symmetry-allowed term accounting for crystalline anisotropy is third order in momentum and takes the form,

$$\mathcal{H}_w(\mathbf{k}) = \frac{\lambda}{2} (k_+^3 + k_-^3) \sigma_z. \quad (2)$$

This warping Hamiltonian is proportional to the Pauli matrix σ_z , which is crucial to obtain a non-zero Berry curvature and leads to out-of-plane spin textures. The Hamiltonian $\mathcal{H} = \mathcal{H}_{\text{TI}} + \mathcal{H}_w$ realizes the hexagonally warped Dirac cone [1] originally predicted to appear at the surface of the Bi_2Te_3 . However, such an anomalous state is allowed only in strong three-dimensional topological insulators. Although recent reports [2] suggest that Bi can have a non-trivial \mathbb{Z}_2 time-reversal-protected topology, previous studies have indicated that this elemental material has a trivial strong topological index, and rather realizes a higher-order topological insulator [3]. The trivial value of the strong topological index implies that the effective surface Hamiltonian must be equipped with a regularizing term $\propto \mathbf{k}^2$ such that at each Fermi energy there is an even number of surface Kramers' pairs [4]. As a result, the effective surface Hamiltonian reads

$$\mathcal{H}(\mathbf{k}) = \frac{\hbar^2 k^2}{2m^*} + \hbar v_F (\sigma_x k_y - \sigma_y k_x) + \frac{\lambda}{2} (k_+^3 + k_-^3) \sigma_z, \quad (3)$$

which corresponds to the Hamiltonian of a hexagonally warped Rashba two-dimensional electron system.

The Berry curvature associated with this effective Hamiltonian can be calculated by rewriting Eq. 3 as $\mathcal{H}(\mathbf{k}) = \mathbf{d}(\mathbf{k}) \cdot \boldsymbol{\sigma} + \hbar^2 \mathbf{k}^2 \sigma_0 / (2m)$. Here, \mathbf{d} is a momentum dependent vector, which for our specific model has components $\mathbf{d} = \{-v_F k_y, v_F k_x, \lambda (k_+^3 + k_-^3) / 2\}$. In terms of the \mathbf{d} vector, the Berry curvature can be expressed as $\Omega_z^{\pm}(\mathbf{k}) = \pm \hat{\mathbf{d}} \cdot (\partial_{k_x} \hat{\mathbf{d}} \times \partial_{k_y} \hat{\mathbf{d}}) / 2$ with $\hat{\mathbf{d}} = \mathbf{d} / |\mathbf{d}|$. As a result, we have that for the surface effective Hamiltonian Eq. 3 the Berry curvature is

$$\Omega_{\pm}^z(k, \theta_{\mathbf{k}}) = \pm \frac{2\sqrt{2}\lambda \hbar^2 v_F^2 k^3 \cos(3\theta_{\mathbf{k}})}{[2\hbar^2 v_F^2 k^2 + \lambda^2 k^6 \cos(6\theta_{\mathbf{k}}) + \lambda^2 k^6]^{3/2}}, \quad (4)$$

where θ is the polar angle in momentum space, and the \pm sign distinguishes the two surface bands. The Berry curvature is well defined in each point except the origin where the bands are degenerate. Note that the constraints set by time reversal symmetry and the three-fold rotational symmetry are satisfied as can be verified upon a closer inspection of Eq. (4). Moreover, $\Omega_{\pm}^z(k, \theta_{\mathbf{k}})$ vanishes along the mirror lines thus proving that the Berry curvature is

entirely driven by crystalline anisotropy terms. The Berry curvature triple (BCT) [5] is instead defined as a convolution of the Berry curvature with the angular form factor for the threefold rotation symmetry:

$$\text{BCT}(\epsilon_F) = 2\pi\hbar \int \frac{d^2\mathbf{k}}{(2\pi)^2} \delta(\epsilon_F - \epsilon) \Omega_{\pm}^z(k, \theta_{\mathbf{k}}) \cos(3\theta_{\mathbf{k}}) \quad (5)$$

This quantity has dimension of time and, as shown below, governs the disorder-induced contribution to the nonlinear Hall effect.

B. Second-order scattering rate and transport scattering time

In this section, we derive the second-order scattering rate and the transport scattering time at the (111) surfaces of Bi considering long-ranged impurities where the impurity potential corresponds to a screened Coulomb interaction. To compute the scattering rates we write the normalized wavefunctions for the two surface state bands as

$$|\mathbf{k}_-\rangle = \begin{pmatrix} \sin \frac{\varphi_{\mathbf{k}}}{2} \\ i \cos \frac{\varphi_{\mathbf{k}}}{2} \exp(i\theta_{\mathbf{k}}) \end{pmatrix} \exp(i\mathbf{k} \cdot \mathbf{r}) \quad (6)$$

$$|\mathbf{k}_+\rangle = \begin{pmatrix} \cos \frac{\varphi_{\mathbf{k}}}{2} \\ -i \sin \frac{\varphi_{\mathbf{k}}}{2} \exp(i\theta_{\mathbf{k}}) \end{pmatrix} \exp(i\mathbf{k} \cdot \mathbf{r}), \quad (7)$$

where we introduced the angle $\varphi_{\mathbf{k}}$ defined by

$$\cos \varphi_{\mathbf{k}} = \frac{\lambda k^3 \cos 3\theta_{\mathbf{k}}}{\sqrt{\hbar^2 v_F^2 k^2 + \lambda^2 k^6 \cos^2 3\theta_k}} \quad (8)$$

We next introduce the ‘‘Dirac’’ energy $\epsilon_0(\mathbf{k}) = \sqrt{\hbar^2 v_F^2 k^2 + \lambda^2 k^6 \cos^2 3\theta_k}$ and the momentum-dependent Dirac mass term $m(\mathbf{k}) = \lambda k^3 \cos 3\theta_k$. In terms of these quantities, the generic Bloch state can be written as

$$|\mathbf{k}_\mu\rangle = \frac{1}{\sqrt{2\epsilon_0(\mathbf{k})}} \begin{pmatrix} \sqrt{\epsilon_0(\mathbf{k}) + \mu m(\mathbf{k})} \\ -i\mu \sqrt{\epsilon_0(\mathbf{k}) - \mu m(\mathbf{k})} \exp(i\theta_{\mathbf{k}}) \end{pmatrix} \exp(i\mathbf{k} \cdot \mathbf{r}) \quad (9)$$

where $\mu = \pm 1$ distinguishes between the inner ($\mu = 1$) and the outer ($\mu = -1$) warped Rashba bands. To make further progress, it is convenient to treat the warping term parametrized by λ as a perturbation and hence expand in powers of λ . To linear order, we can then write the eigenstates as

$$|\mathbf{k}_\mu\rangle = \frac{1}{\sqrt{2}} \begin{pmatrix} 1 + \mu M(\mathbf{k}) \\ -i(\mu - M(\mathbf{k})) \exp(i\theta_{\mathbf{k}}) \end{pmatrix} \exp(i\mathbf{k} \cdot \mathbf{r}), \quad (10)$$

where we introduced the dimensionless Dirac mass $M(\mathbf{k}) = \lambda k^2 \cos 3\theta_k / (2\hbar v_F)$. The matrix element of the Coulomb impurity potential up to linear order in the Dirac mass is given by

$$\langle \mathbf{k}_\mu | \mathcal{V}(\mathbf{r}) | \mathbf{k}'_{\mu'} \rangle = \frac{V_0^{\mathbf{k}, \mathbf{k}'}}{2} \left[1 + \mu\mu' e^{i(\theta_{\mathbf{k}'} - \theta_{\mathbf{k}})} + (\mu M(\mathbf{k}) + \mu' M(\mathbf{k}')) \right. \\ \left. (1 - \mu\mu' e^{i(\theta_{\mathbf{k}'} - \theta_{\mathbf{k}})}) \right] \mathcal{H}(\mathbf{k}_\mu, \mathbf{k}'_{\mu'}) \quad (11)$$

In the equation above, we have introduced $V_0^{\mathbf{k}, \mathbf{k}'} = \sum_j 2\pi Q e^2 / (4\pi\epsilon_0\epsilon) e^{i(\mathbf{k} - \mathbf{k}') \cdot \mathbf{r}_j}$, and the Coulomb kernel $\mathcal{H}(\mathbf{k}_\mu, \mathbf{k}'_{\mu'}) = \left([k_\mu^2 + k_{\mu'}^2 - 2k_\mu k_{\mu'} \cos(\theta_{\mathbf{k}'} - \theta_{\mathbf{k}})]^{1/2} + q_{TF} \right)^{-1}$ where q_{TF} is the Thomas-Fermi wavevector.

The symmetric part of the scattering rate is given by [6–8]

$$\omega_{l,l'}^{(2)} = \frac{2\pi}{\hbar} \langle | \langle \mathbf{k}_\mu | \mathcal{V}(\mathbf{r}) | \mathbf{k}'_{\mu'} \rangle |^2 \rangle_{dis} \delta(\epsilon_l - \epsilon_{l'})$$

where $l = \{\mathbf{k}, \mu\}$. Let us introduce the dimensionless parameter $\alpha = Qe^2 / (4\pi\epsilon_0\epsilon\hbar v_F)$. At the zeroth order in the warping strength, the second-order scattering rate can be written as

$$\omega_{l,l'}^{(2)} = 4\pi^3 n_i \hbar v_F^2 \alpha^2 [1 + \mu\mu' \cos(\theta_{\mathbf{k}'} - \theta_{\mathbf{k}})] \mathcal{H}(\mathbf{k}_\mu, \mathbf{k}'_{\mu'})^2 \delta(\epsilon_l - \epsilon_{l'}) \quad (12)$$

where n_i is the impurity concentration.

Up to order λ^2 , the Fermi surfaces can be considered circular with radius $k_{F\pm}$. Furthermore, the circular Fermi lines radii are related to each other by $k_{F\mu} = k_{F\mu'} - 2mv_F\mu/\hbar$. The momentum shift between the two parabolas proportional to the spin-orbit coupling strength defines the characteristic momentum $k_{SO} = 2mv_F/\hbar$. It is therefore convenient to introduce the shifted momenta $\tilde{\mathbf{k}} = \mathbf{k} + \mu k_{SO}/2$. Note that at the Fermi energy the shifted wavevector $|\tilde{\mathbf{k}}| = \bar{k}_F = \sum_{\mu} k_{F\mu}/2$ is independent of the band index. The Coulomb kernel can be now written as a series expansion in k_{SO}/\bar{k}_F . At the leading order we have

$$\mathcal{K}^{-1}(\mathbf{k}_{\mu}, \mathbf{k}'_{\mu'}) = \bar{k}_F [2(1 - \cos(\theta_{\mathbf{k}'} - \theta_{\mathbf{k}}))]^{1/2} + q_{TF} \quad (13)$$

Consequently, the second-order scattering rate can be expressed as

$$\omega_{l;l'}^{(2)} = \frac{4\pi^3 n_i \hbar v_F^2 \alpha^2 [1 + \mu\mu' \cos(\theta_{\mathbf{k}'} - \theta_{\mathbf{k}})]}{\bar{k}_F^2 \left(2 \left| \sin \frac{\theta_{\mathbf{k}} - \theta_{\mathbf{k}'}}{2} \right| + \frac{q_{TF}}{\bar{k}_F}\right)^2} \quad (14)$$

Then we determine the transport scattering time. We start by recalling that the transport scattering time can be found from the solution of the self-consistent equation

$$e\mathbf{E} \cdot \mathbf{v}_l \frac{\partial f_l^0}{\partial \epsilon_l} = - \sum_{l'} \omega_{l;l'}^{(2)} \left[-e\mathbf{E} \cdot \mathbf{v}_l \tau_l^{tr} \frac{\partial f_l^0}{\partial \epsilon_l} + e\mathbf{E} \cdot \mathbf{v}_{l'} \tau_{l'}^{tr} \frac{\partial f_{l'}^0}{\partial \epsilon_{l'}} \right] \quad (15)$$

The equation above can be simplified by noticing that the second-order scattering rate conserves the energy and the equilibrium distribution function depends only on energy. Therefore, we are left with the set of self-consistent equations for the group velocities $\mathbf{v}_l = \partial \epsilon_l / (\hbar \partial \mathbf{k})$

$$\mathbf{v}_l = \tau_l^{tr} \mathbf{v}_l \sum_{l'} \omega_{l;l'}^{(2)} - \sum_{l'} \omega_{l;l'}^{(2)} \mathbf{v}_{l'} \tau_{l'}^{tr} \quad (16)$$

We follow Ref. [9] and define the quasiparticle scattering times $\frac{1}{\tau_l} = \sum_{l'} \omega_{l;l'}^{(2)}$. Using this definition and the fact that upon momentum integration only the component of $\mathbf{v}_{l'}$ parallel to \mathbf{v}_l survives, we obtain that the equation above can be recast as

$$\frac{\tau_l^{tr}}{\tau_l} = 1 + \sum_{l'} \omega_{l;l'}^{(2)} \tau_{l'}^{tr} \frac{\mathbf{v}_{l'} \cdot \hat{v}_l}{|\mathbf{v}_l|} \quad (17)$$

As noticed in Ref. [9], this is a set of coupled equations for two band-dependent transport scattering times. At the zeroth order in k_{SO}/\bar{k}_F , the magnitude of the two band velocities are equal. Hence, we can derive a constant transport scattering time

$$\frac{1}{\tau^{tr}} = \sum_{l'} \omega_{l;l'}^{(2)} (1 - \cos(\theta_{\mathbf{k}'} - \theta_{\mathbf{k}})) \quad (18)$$

Substituting in the equation above the expression for the second-order scattering rate, the transport scattering time reads

$$\frac{1}{\tau^{tr}} = \frac{2\pi m n_i v_F^2 \alpha^2}{\hbar \bar{k}_F^2} c^S \left(\frac{q_{TF}}{\bar{k}_F} \right) \quad (19)$$

where the numerical factor

$$c^S \left(\frac{q_{TF}}{\bar{k}_F} \right) = \int d\theta_{\mathbf{k}'} \frac{(1 - \cos(\theta_{\mathbf{k}'} - \theta_{\mathbf{k}}))}{\left(2 \left| \sin \frac{\theta_{\mathbf{k}} - \theta_{\mathbf{k}'}}{2} \right| + \frac{q_{TF}}{\bar{k}_F}\right)^2} \quad (20)$$

and in the limit of unscreened impurities reduces to $c^S(q_{TF}/\bar{k}_F) = \pi$. In the opposite limit of δ -like impurities, *i.e.* for $q_{TF} \gg \bar{k}_F$, the numerical factor $c^S(q_{TF}/\bar{k}_F) \simeq 2\pi \bar{k}_F^2 / q_{TF}^2$, as expected.

C. Third-order scattering rate and skew contribution to the nonlinear Hall effect

In the following, we consider the third-order scattering rate (see for instance Ref. [6]) given by

$$\omega_{l;l'}^{(3)} = \frac{2\pi}{\hbar} \left(\sum_{l''} \frac{\langle \mathcal{V}_{ll'} \mathcal{V}_{l'l''} \mathcal{V}_{l''l} \rangle_{dis}}{\epsilon_l - \epsilon_{l''} - i\eta} + \text{c.c.} \right) \delta(\epsilon_l - \epsilon_{l'}) \quad (21)$$

We note that the term in parenthesis can be simplified as

$$P \left(\sum_{l''} \frac{2\text{Re} \langle \mathcal{V}_{ll'} \mathcal{V}_{l'l''} \mathcal{V}_{l''l} \rangle_{dis}}{\epsilon_l - \epsilon_{l''}} \right) - 2\pi \sum_{l''} \text{Im} \langle \mathcal{V}_{ll'} \mathcal{V}_{l'l''} \mathcal{V}_{l''l} \rangle_{dis} \delta(\epsilon_l - \epsilon_{l''}) \quad (22)$$

The first term in the equation above does not contribute to the antisymmetric part of the third-order scattering rate. It is in fact symmetric under the $l \leftrightarrow l'$ once considering the Dirac δ function appearing in Eq. 21. As a result, we can write the antisymmetric third-order scattering term as

$$\omega_{l;l'}^{(3a)} = -\frac{(2\pi)^2}{\hbar} \sum_{l''} \text{Im} \langle \mathcal{V}_{ll'} \mathcal{V}_{l'l''} \mathcal{V}_{l''l} \rangle_{dis} \delta(\epsilon_l - \epsilon_{l''}) \delta(\epsilon_l - \epsilon_{l'}) \quad (23)$$

After tedious but straightforward calculations, one finds that

$$\begin{aligned} \text{Im} \langle \mathcal{V}_{ll'} \mathcal{V}_{l'l''} \mathcal{V}_{l''l} \rangle_{dis} &= \frac{(2\pi\hbar v_F \alpha)^3 n_i \mu \mu' \mu''}{2} [\sin(\theta_q - \theta_{k'}) M(\mathbf{k}_\mu) + \sin(\theta_k - \theta_q) M(\mathbf{k}'_{\mu'}) \\ &\quad - \sin(\theta_k - \theta_{k'}) M(\mathbf{q}_{\mu''})] \mathcal{K}(\mathbf{k}_\mu, \mathbf{k}'_{\mu'}) \mathcal{K}(\mathbf{k}_\mu, \mathbf{q}_{\mu''}) \mathcal{K}(\mathbf{k}'_{\mu'}, \mathbf{q}_{\mu''}) \end{aligned} \quad (24)$$

Inserting this expression in the relation for the antisymmetric third-order scattering rate, we have

$$\begin{aligned} \omega_{\mathbf{k};\mathbf{k}'}^{\mu,\mu'}^{(3a)} &= -4\pi^3 \hbar^2 \alpha^3 v_F^3 n_i \mu \mu' \sum_{\mu''} \mu'' \int q dq d\theta_{\mathbf{q}} \frac{\nu_{\mu''}(q)}{q} \delta(k_{F_{\mu''}} - q) [\sin(\theta_q - \theta_{k'}) M(\mathbf{k}_\mu) \\ &\quad + \sin(\theta_k - \theta_q) M(\mathbf{k}'_{\mu'}) - \sin(\theta_k - \theta_{k'}) M(\mathbf{q}_{\mu''})] \mathcal{K}(\mathbf{k}_\mu, \mathbf{k}'_{\mu'}) \mathcal{K}(\mathbf{k}_\mu, \mathbf{q}_{\mu''}) \mathcal{K}(\mathbf{k}'_{\mu'}, \mathbf{q}_{\mu''}) \\ &\quad \times \delta(\epsilon_{\mathbf{k}} - \epsilon_{\mathbf{k}'}) \end{aligned} \quad (25)$$

In the equation above, we have introduced the quantities related to the density of states $\nu_{\mu''}(q)^{-1} = \hbar^2/m + \mu''\hbar v_F/q$. Note that the antisymmetric third-order scattering rate appears at linear order in the warping strength λ .

Let us first consider the limiting case of δ -like impurities. In this case, the expression for the third-order scattering rate can be recast in the following form:

$$\omega_{\mathbf{k};\mathbf{k}'}^{\mu,\mu'}^{(3a)} \propto \lambda \mu' \sin(\theta_k - \theta_{k'}) \left[\nu_\mu k_{F_\mu}^2 - \nu_{\bar{\mu}} k_{F_{\bar{\mu}}}^2 \right] \int d\theta_q \cos 3\theta_q \times \delta(\epsilon_{\mathbf{k}} - \epsilon_{\mathbf{k}'}), \quad (26)$$

where $\bar{\mu} = -\mu$. Importantly, the scattering rate vanishes because of the threefold symmetry of the dimensionless mass. This is in contrast with the case of a ferromagnetic Rashba model, where instead the absence of skew scattering [10] is due to the identity $\nu_+(k_{F_+})/k_{F_+} \equiv \nu_-(k_{F_-})/k_{F_-}$. Put differently, the vanishing of the skew scattering is not dependent on the number of occupied Kramers' pairs but is solely due to the threefold symmetry of the mass. A finite antisymmetric third-order scattering rate will therefore appear when instead of delta impurities we restore the screened Coulomb kernel for charged impurities.

To explicitly show this, it is convenient to introduce, similarly to the second-order scattering rate, the shifted momentum $\tilde{\mathbf{q}} = \mathbf{q} + \mu k_{SO}/2$. For simplicity we calculate the Coulomb kernels for an equal amplitude \bar{k}_F . Then, Eq. 25 can be recast as

$$\begin{aligned} \omega_{\mathbf{k};\mathbf{k}'}^{\mu,\mu'}^{(3a)} &\simeq -4\pi^3 \hbar^2 \alpha^3 v_F^3 n_i \mu \mu' \sum_{\mu''} \mu'' \left(\bar{k}_F - \frac{\mu'' k_{SO}}{2} \right) \frac{m}{\hbar^2 \bar{k}_F} \frac{\lambda}{2\hbar v_F} \frac{1}{\bar{k}_F^3} \int d\theta_{\mathbf{q}} \left[\sin(\theta_{\mathbf{q}} - \theta_{\mathbf{k}'}) \cos 3\theta_{\mathbf{k}} \left(\bar{k}_F - \mu \frac{k_{SO}}{2} \right)^2 \right. \\ &\quad \left. + \sin(\theta_{\mathbf{k}} - \theta_{\mathbf{q}}) \cos 3\theta_{\mathbf{k}'} \left(\bar{k}_F - \mu' \frac{k_{SO}}{2} \right)^2 - \sin(\theta_{\mathbf{k}} - \theta_{\mathbf{k}'}) \cos 3\theta_{\mathbf{q}} \left(\bar{k}_F - \mu'' \frac{k_{SO}}{2} \right)^2 \right] \frac{1}{2 \left| \sin \frac{\theta_{\mathbf{k}} - \theta_{\mathbf{q}}}{2} \right| + \frac{q_{TF}}{\bar{k}_F}} \times \\ &\quad \frac{1}{2 \left| \sin \frac{\theta_{\mathbf{k}'} - \theta_{\mathbf{q}}}{2} \right| + \frac{q_{TF}}{\bar{k}_F}} \frac{1}{2 \left| \sin \frac{\theta_{\mathbf{k}} - \theta'_{\mathbf{k}}}{2} \right| + \frac{q_{TF}}{\bar{k}_F}} \times \delta(\epsilon_{\mathbf{k}} - \epsilon_{\mathbf{k}'}) \end{aligned} \quad (27)$$

Here we have used the additional identity $\nu_+(k_{F+})/k_{F+} \equiv m/(\hbar^2 \bar{k}_F)$. With this, we obtain that the non-vanishing antisymmetric third-order scattering rate can be conveniently written as

$$\begin{aligned} \omega_{\mathbf{k};\mathbf{k}'}^{\mu,\mu'}(3a) &= \frac{2\pi^3 \lambda v_F^2 \alpha^3 n_i m \mu \mu'}{\hbar \bar{k}_F} \frac{\hat{z} \cdot (\hat{\mathbf{k}} \times \hat{\mathbf{k}}')}{|\hat{\mathbf{k}} - \hat{\mathbf{k}}'| + \frac{q_{TF}}{\bar{k}_F}} \delta(\epsilon_{\mathbf{k}} - \epsilon_{\mathbf{k}'}) \left[\frac{k_{SO}}{\bar{k}_F} \mathcal{F}_1(\theta_{\mathbf{k}}, \theta_{\mathbf{k}'}, \frac{q_{TF}}{\bar{k}_F}) + \frac{k_{SO}^3}{4\bar{k}_F^3} \mathcal{F}_3(\theta_{\mathbf{k}}, \theta_{\mathbf{k}'}, \frac{q_{TF}}{\bar{k}_F}) \right. \\ &\quad \left. - \frac{k_{SO}^2}{\bar{k}_F^2} \mathcal{F}_2^{\mu\mu'}(\theta_{\mathbf{k}}, \theta_{\mathbf{k}'}, \frac{q_{TF}}{\bar{k}_F}) \right] \end{aligned} \quad (28)$$

where we have introduced three angular functions

$$\begin{aligned} \mathcal{F}_1(\theta_{\mathbf{k}}, \theta_{\mathbf{k}'}, \frac{q_{TF}}{\bar{k}_F}) &= \int d\theta_{\mathbf{q}} \left[3 \cos 3\theta_{\mathbf{q}} - \frac{\sin(\theta_{\mathbf{q}} - \theta_{\mathbf{k}'}) \cos 3\theta_{\mathbf{k}} + \sin(\theta_{\mathbf{k}} - \theta_{\mathbf{q}}) \cos 3\theta_{\mathbf{k}'}}{\sin(\theta_{\mathbf{k}} - \theta_{\mathbf{k}'})} \right] \times \frac{1}{2 \left| \sin \frac{\theta_{\mathbf{k}} - \theta_{\mathbf{q}}}{2} \right| + \frac{q_{TF}}{\bar{k}_F}} \\ &\quad \times \frac{1}{2 \left| \sin \frac{\theta_{\mathbf{k}'} - \theta_{\mathbf{q}}}{2} \right| + \frac{q_{TF}}{\bar{k}_F}} \end{aligned} \quad (29)$$

$$\begin{aligned} \mathcal{F}_3(\theta_{\mathbf{k}}, \theta_{\mathbf{k}'}, \frac{q_{TF}}{\bar{k}_F}) &= \int d\theta_{\mathbf{q}} \left[\cos 3\theta_{\mathbf{q}} - \frac{\sin(\theta_{\mathbf{q}} - \theta_{\mathbf{k}'}) \cos 3\theta_{\mathbf{k}} + \sin(\theta_{\mathbf{k}} - \theta_{\mathbf{q}}) \cos 3\theta_{\mathbf{k}'}}{\sin(\theta_{\mathbf{k}} - \theta_{\mathbf{k}'})} \right] \times \frac{1}{2 \left| \sin \frac{\theta_{\mathbf{k}} - \theta_{\mathbf{q}}}{2} \right| + \frac{q_{TF}}{\bar{k}_F}} \\ &\quad \times \frac{1}{2 \left| \sin \frac{\theta_{\mathbf{k}'} - \theta_{\mathbf{q}}}{2} \right| + \frac{q_{TF}}{\bar{k}_F}} \end{aligned} \quad (30)$$

$$\begin{aligned} \mathcal{F}_2^{\mu\mu'}(\theta_{\mathbf{k}}, \theta_{\mathbf{k}'}, \frac{q_{TF}}{\bar{k}_F}) &= \int d\theta_{\mathbf{q}} \frac{-\mu \sin(\theta_{\mathbf{q}} - \theta_{\mathbf{k}'}) \cos 3\theta_{\mathbf{k}} - \mu' \sin(\theta_{\mathbf{k}} - \theta_{\mathbf{q}}) \cos 3\theta_{\mathbf{k}'}}{\sin(\theta_{\mathbf{k}} - \theta_{\mathbf{k}'})} \times \frac{1}{2 \left| \sin \frac{\theta_{\mathbf{k}} - \theta_{\mathbf{q}}}{2} \right| + \frac{q_{TF}}{\bar{k}_F}} \\ &\quad \times \frac{1}{2 \left| \sin \frac{\theta_{\mathbf{k}'} - \theta_{\mathbf{q}}}{2} \right| + \frac{q_{TF}}{\bar{k}_F}} \end{aligned} \quad (31)$$

Next we follow the argument presented in Ref. [5] and use that the largest contribution to the angular function, expanded in harmonic series, is given by $\mathcal{F}_{1,2,3}^{(\mu,\mu')}(\theta_{\mathbf{k}}, \theta_{\mathbf{k}'}, q_{TF}/\bar{k}_F) = c_{1,2,3}^{A(\mu\mu')} (q_{TF}/\bar{k}_F) (\cos 3\theta_{\mathbf{k}} + \cos 3\theta_{\mathbf{k}'})$. Numerical results for the c^A 's show that they decay for large q_{TF}/\bar{k}_F is in agreement with our foregoing analysis for short-range impurities. Furthermore, we obtain that the constant $c_2^{A^{1-1}}$ is numerically zero. Note that while the two terms governed by $c_{1,3}^A$ lead to equal intraband scattering rates opposite to the interband scattering rate, the two intraband scattering rates due to the $c_2^{A^{\pm 1 \pm 1}}$ are opposite between each other.

Let us relate the antisymmetric scattering rate to the Berry curvature triple. Here we can use that in the linear order in the warping strength λ the Berry curvature can be expressed as

$$\Omega_{\pm}^z(k, \theta_{\mathbf{k}}) = \pm \frac{\lambda \cos 3\theta_{\mathbf{k}}}{\hbar v_F} + \mathcal{O}(\lambda^2). \quad (32)$$

Inserting the expression above in the definition of the Berry curvature triple of Eq. 5 for the two warped Rashba bands, we have

$$BCT_{\mu}(\epsilon_F) = \frac{\mu \lambda m}{2\hbar^2 v_F \bar{k}_F} \left(\bar{k}_F - \frac{\mu k_{SO}}{2} \right) \quad (33)$$

The equation above also defines the average Berry curvature triple of our system given by

$$\overline{BCT}(\epsilon_F) = -\frac{\lambda m k_{SO}}{4\hbar^2 v_F \bar{k}_F} \quad (34)$$

and depends on the Fermi energy. Substituting this expression in Eq. 28, we obtain the direct relation between the Berry curvature triple and the antisymmetric third-order scattering rate

$$\omega_{\mathbf{k};\mathbf{k}'}^{\mu,\mu'}(3a) = -\frac{(2\pi\alpha v_F)^3 n_i \hbar \overline{BCT}(\epsilon_F)\mu\mu'}{k_{SO}} \frac{\hat{z} \cdot (\hat{\mathbf{k}} \times \hat{\mathbf{k}'})}{|\hat{\mathbf{k}} - \hat{\mathbf{k}}'| + \frac{q_{TF}}{k_F}} (\cos 3\theta_{\mathbf{k}} + \cos 3\theta_{\mathbf{k}'}) \delta(\epsilon_{\mathbf{k}} - \epsilon_{\mathbf{k}'}) \times \left[\frac{k_{SO}}{k_F} c_1^A\left(\frac{q_{TF}}{k_F}\right) + \frac{k_{SO}^3}{4k_F^3} c_3^A\left(\frac{q_{TF}}{k_F}\right) - \frac{k_{SO}^2}{k_F^2} c_2^{A\mu\mu'}\left(\frac{q_{TF}}{k_F}\right) \right] \quad (35)$$

We can now proceed to evaluate the skew contribution to the nonlinear conductivity tensor $\chi_{\alpha\beta\gamma}$. As discussed below, the \mathcal{C}_{3v} point group of the crystal implies that we need to compute a single component of the nonlinear conductivity tensor given by χ_{yxx} . We therefore follow Ref. [7, 8] and note that there exist two different terms in the skew scattering nonlinear conductivity χ_{yxx} , the first of which is given by

$$\chi_{yxx}^{sk1} = -\frac{e^3\tau^3}{\hbar^3} \sum_{l'l'} \omega_{\mathbf{k};\mathbf{k}'}^{\mu,\mu'}(3a) \left(\partial_{k_x} \partial_{k_y} \epsilon_l - \partial_{k_x'} \partial_{k_y'} \epsilon_{l'} \right) \partial_{k_x} f_l^0, \quad (36)$$

where f_l^0 is the equilibrium Fermi-Dirac distribution function and τ is the transport scattering time evaluated before. At the linear order in the warping strength λ , it is sufficient to keep terms related to the energy of the Rashba bands up to λ^0 . As a result, the first skew scattering contribution to the nonlinear Hall effect is given by

$$\chi_{yxx}^{sk1} = -\frac{e^3\tau^3}{\hbar^3} \frac{2(2\pi\alpha)^3 v_F^4 m n_i \overline{BCT}(\epsilon_F)}{k_F^2} \times g^{sk1}\left(\frac{q_{TF}}{k_F}\right) \quad (37)$$

To obtain the equation above, we have used the symmetry properties of the various terms in the antisymmetric scattering rate and introduce a new constant given by the product of c_2^{A11} with the double integral over the angular dependence. We find that g^{sk1} is positive and of order one for $q_{TF}/k_F \geq 0.4$.

Let us now compute the second skew scattering contribution to the nonlinear Hall effect. It is given by

$$\chi_{yxx}^{sk2} = \frac{e^3\tau^3}{\hbar^3} \sum_{l'l'} \omega_{\mathbf{k};\mathbf{k}'}^{\mu,\mu'}(3a) \left(\partial_{k_y} \epsilon_l - \partial_{k_y'} \epsilon_{l'} \right) \partial_{k_x} \partial_{k_x} f_l^0. \quad (38)$$

We can integrate by parts and thereby obtain that $\chi_{yxx}^{sk2} = \chi_{yxx}^{sk1} + \bar{\chi}_{yxx}^{sk2}$ with

$$\bar{\chi}_{yxx}^{sk2} = -\frac{e^3\tau^3}{\hbar^3} \sum_{l'l'} \partial_{k_x} \omega_{\mathbf{k};\mathbf{k}'}^{\mu,\mu'}(3a) \left(\partial_{k_y} \epsilon_l - \partial_{k_y'} \epsilon_{l'} \right) \partial_{k_x} f_l^0 \quad (39)$$

We only explicitly consider the angular dependence of the scattering rate. Furthermore, using that the group velocity $\partial_{k_y} \epsilon_l = \sin \theta_{\mathbf{k}} (\hbar^2 k/m + \mu \hbar v_F)$ it can be found that only the component of the scattering rate $\propto c_2^{A\pm 1 \pm 1}$ gives a finite contribution at the leading order. With this, it follows that the total skew scattering contribution can be written as

$$\chi_{yxx}^{sk} = -\frac{e^3\tau^3}{\hbar^3} \frac{2(2\pi\alpha)^3 v_F^4 m n_i \overline{BCT}(\epsilon_F)}{k_F^2} \times \left(2g^{sk1}\left(\frac{q_{TF}}{k_F}\right) + g^{sk2}\left(\frac{q_{TF}}{k_F}\right) \right) \quad (40)$$

As for g^{sk1} also g^{sk2} is positive and of order one for $q_{TF}/k_F \geq 0.4$.

As pointed out in Ref. [7, 8], the antisymmetric part of the fourth-order scattering rate provides an additional nonlinear skew scattering contribution to the nonlinear Hall effect. As we will show in Supplementary Theory Note E, also this term must be proportional to the warping strength λ and thus to the Berry curvature triple.

D. Coordinate shift and side jump contributions to the nonlinear Hall effect

We first determine the coordinate shift whose gauge-invariant expression [6] is given by

$$\delta \mathbf{r}_{ll'} = \langle \mathbf{k}_\mu | i \partial_{\mathbf{k}} \mathbf{k}_\mu \rangle - \langle \mathbf{k}'_{\mu'} | i \partial_{\mathbf{k}'} \mathbf{k}'_{\mu'} \rangle - (\partial_{\mathbf{k}} + \partial_{\mathbf{k}'}) \arg[\langle \mathbf{k}_\mu | \mathbf{k}'_{\mu'} \rangle] \quad (41)$$

To find the coordinate shift, we note that with the form of the wavefunction expanded up to linear order in the Dirac mass, the following relations hold

$$\begin{aligned}\langle \mathbf{k}_\mu | \partial_k | \mathbf{k}_\mu \rangle &= M(\mathbf{k}) \partial_k M(\mathbf{k}) \\ \langle \mathbf{k}_\mu | \partial_{\theta_k} | \mathbf{k}_\mu \rangle &= M(\mathbf{k}) \partial_{\theta_k} M(\mathbf{k}) + \frac{i}{2} [\mu - M(\mathbf{k})]^2\end{aligned}\quad (42)$$

In terms of these quantities, one can evaluate the coordinate shift contribution up to linear order in the warping strength λ

$$\begin{aligned}i \langle \mathbf{k}_\mu | \partial_{k_x} | \mathbf{k}_\mu \rangle &= \frac{1}{2} \frac{\sin \theta_{\mathbf{k}}}{k} [1 - 2\mu M(\mathbf{k})] \\ i \langle \mathbf{k}_\mu | \partial_{k_y} | \mathbf{k}_\mu \rangle &= -\frac{1}{2} \frac{\cos \theta_{\mathbf{k}}}{k} [1 - 2\mu M(\mathbf{k})]\end{aligned}\quad (43)$$

To evaluate the coordinate shift contribution $\propto \partial_{k_{x,y}} \arg [\langle \mathbf{k}_\mu | \mathbf{k}'_{\mu'} \rangle]$ we remember the following relation [7]

$$\partial_x \arg A = \frac{i}{|A|^2} \left(\frac{1}{2} \partial_x |A|^2 - A^* \partial_x A \right)\quad (44)$$

Moreover, we have that up to linear order in λ

$$\begin{aligned}\langle \mathbf{k}_\mu | \mathbf{k}'_{\mu'} \rangle &= \frac{1}{2} \left[\left(1 + \mu \mu' e^{i(\theta_{\mathbf{k}'} - \theta_{\mathbf{k}})} \right) + M(\mathbf{k}) \left(\mu - \mu' e^{i(\theta_{\mathbf{k}'} - \theta_{\mathbf{k}})} \right) + M(\mathbf{k}') \left(\mu' - \mu e^{i(\theta_{\mathbf{k}'} - \theta_{\mathbf{k}})} \right) \right] \\ |\langle \mathbf{k}_\mu | \mathbf{k}'_{\mu'} \rangle|^2 &= \frac{1}{2} (1 + \mu \mu' \cos(\theta_{\mathbf{k}'} - \theta_{\mathbf{k}}))\end{aligned}\quad (45)$$

$$\partial_k \arg [\langle \mathbf{k}_\mu | \mathbf{k}'_{\mu'} \rangle] = -\frac{\partial_k M(\mathbf{k}) \mu'}{(1 + \mu \mu' \cos(\theta_{\mathbf{k}'} - \theta_{\mathbf{k}}))} \sin(\theta_{\mathbf{k}'} - \theta_{\mathbf{k}})\quad (46)$$

$$\partial_{k'} \arg [\langle \mathbf{k}_\mu | \mathbf{k}'_{\mu'} \rangle] = -\frac{\partial_{k'} M(\mathbf{k}') \mu}{(1 + \mu \mu' \cos(\theta_{\mathbf{k}'} - \theta_{\mathbf{k}}))} \sin(\theta_{\mathbf{k}'} - \theta_{\mathbf{k}})\quad (47)$$

$$\begin{aligned}\partial_{\theta_{\mathbf{k}}} \arg [\langle \mathbf{k}_\mu | \mathbf{k}'_{\mu'} \rangle] &= -\frac{1}{2} - \frac{\partial_{\theta_{\mathbf{k}}} M(\mathbf{k}) \mu'}{(1 + \mu \mu' \cos(\theta_{\mathbf{k}'} - \theta_{\mathbf{k}}))} \sin(\theta_{\mathbf{k}'} - \theta_{\mathbf{k}}) \\ &\quad + \frac{\mu M(\mathbf{k}) + \mu' M(\mathbf{k}')}{(1 + \mu \mu' \cos(\theta_{\mathbf{k}'} - \theta_{\mathbf{k}}))}\end{aligned}\quad (48)$$

$$\begin{aligned}\partial_{\theta_{\mathbf{k}'}} \arg [\langle \mathbf{k}_\mu | \mathbf{k}'_{\mu'} \rangle] &= \frac{1}{2} - \frac{\partial_{\theta_{\mathbf{k}'}} M(\mathbf{k}') \mu}{(1 + \mu \mu' \cos(\theta_{\mathbf{k}'} - \theta_{\mathbf{k}}))} \sin(\theta_{\mathbf{k}'} - \theta_{\mathbf{k}}) \\ &\quad - \frac{\mu M(\mathbf{k}) + \mu' M(\mathbf{k}')}{(1 + \mu \mu' \cos(\theta_{\mathbf{k}'} - \theta_{\mathbf{k}}))}\end{aligned}\quad (49)$$

We will now show that the coordinate shift can be entirely expressed in terms of the Berry curvature triple just as the antisymmetric third-order scattering rate governing the skew scattering contribution to the nonlinear Hall effect. Let us first evaluate the contribution to the \hat{x} component of the coordinate shift $\delta \mathbf{r}_{\mu'}^x$, given by $\langle \mathbf{k}_\mu | i \partial_{k_x} | \mathbf{k}_\mu \rangle - \partial_{k_x} \arg [\langle \mathbf{k}_\mu | \mathbf{k}'_{\mu'} \rangle]$. Using that $\partial_k M(\mathbf{k}) = 2M(\mathbf{k})/k$ and trigonometric identities, we obtain that

$$\langle \mathbf{k}_\mu | i \partial_{k_x} | \mathbf{k}_\mu \rangle - \partial_{k_x} \arg [\langle \mathbf{k}_\mu | \mathbf{k}'_{\mu'} \rangle] = \frac{\mu'}{2k |\langle \mathbf{k}_\mu | \mathbf{k}'_{\mu'} \rangle|^2} \left[\sin \theta_{\mathbf{k}} M(\mathbf{k}') - \sin \theta_{\mathbf{k}'} M(\mathbf{k}) + \frac{3\lambda k^2}{2\hbar v_F} \cos 2\theta_{\mathbf{k}} \sin(\theta_{\mathbf{k}'} - \theta_{\mathbf{k}}) \right]\quad (50)$$

We note that the last term in the equation above is derived from the angular dependence and the power law of the Dirac mass. Similarly, we have

$$-\langle \mathbf{k}'_{\mu'} | i \partial_{k'_x} | \mathbf{k}'_{\mu'} \rangle - \partial_{k'_x} \arg [\langle \mathbf{k}_\mu | \mathbf{k}'_{\mu'} \rangle] = \frac{\mu}{2k' |\langle \mathbf{k}_\mu | \mathbf{k}'_{\mu'} \rangle|^2} \left[\sin \theta_{\mathbf{k}} M(\mathbf{k}') - \sin \theta_{\mathbf{k}'} M(\mathbf{k}) + \frac{3\lambda k'^2}{2\hbar v_F} \cos 2\theta_{\mathbf{k}'} \sin(\theta_{\mathbf{k}'} - \theta_{\mathbf{k}}) \right]\quad (51)$$

Combining these equations together, we have that

$$\delta \mathbf{r}_{ll'}^x = -\frac{\hbar \overline{BCT}(\epsilon_F) \bar{k}_F}{mk_{SO} |\langle \mathbf{k}_\mu | \mathbf{k}'_{\mu'} \rangle|^2} \left[\mu k' (\cos 3\theta_{\mathbf{k}'} \sin \theta_{\mathbf{k}} + 3 \cos 2\theta_{\mathbf{k}'} \sin (\theta_{\mathbf{k}'} - \theta_{\mathbf{k}})) - \mu \frac{k^2}{k'} \cos 3\theta_{\mathbf{k}} \sin \theta'_{\mathbf{k}} + \mu' k (-\cos 3\theta_{\mathbf{k}} \sin \theta'_{\mathbf{k}} + 3 \cos 2\theta_{\mathbf{k}} \sin (\theta_{\mathbf{k}'} - \theta_{\mathbf{k}})) + \mu' \frac{k'^2}{k} \cos 3\theta'_{\mathbf{k}} \sin \theta_{\mathbf{k}} \right] \quad (52)$$

A similar equation can be derived also for the \hat{y} component of the coordinate shift. It has the same structure and most importantly is governed by the Berry curvature triple. One can then compute the side-jump velocity $\mathbf{v}_{sj} = \sum_{ll'} \omega_{ll'}^{(2)} \delta \mathbf{r}_{ll'}$ and the two side-jump contributions to the nonlinear Hall effect whose expressions are given in Ref. [7, 8]. We also note that there is an additional side-jump contribution related to the interband Berry connection that has no counterpart in linear response [11]. As we will show in Supplementary Theory Note E, also this term must be proportional to the warping strength λ and thus to the Berry curvature triple.

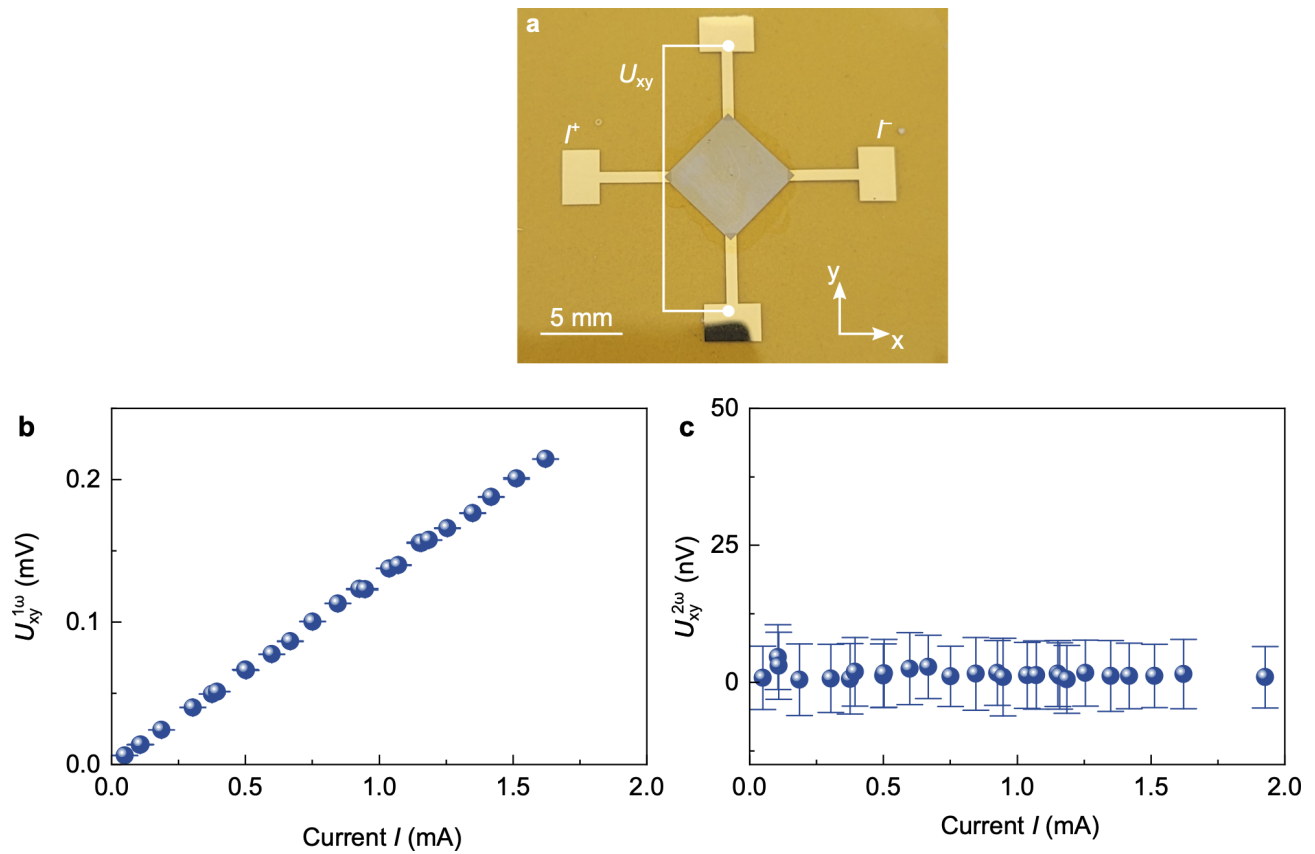
E. Symmetry constraints on the nonlinear conductivity tensor

The nonlinear conductivity tensor is defined by the relation

$$j_\alpha = \chi_{\alpha\beta\gamma} E_\beta E_\gamma \quad (53)$$

We can derive the transformation rule of the nonlinear conductivity tensor under a generic point group symmetry represented by an orthogonal matrix by noticing that both the current j and the driving electric field E transform as vectors under a generic coordinate change. The transformation rule of the nonlinear conductivity tensor imply that in the presence of a \mathcal{M}_x mirror symmetry, we have $\chi_{xxx} = \chi_{xyy} = \chi_{yxy} = \chi_{yyx} = 0$. The additional threefold rotation symmetry in the \mathcal{C}_{3v} point group symmetry implies that the non-zero component of the nonlinear conductivity tensor satisfies the relation $\chi_{xxy} = \chi_{xyx} = \chi_{yxx} = -\chi_{yyy}$. As a result, the nonlinear conductivity tensor is governed by a single quantity. Note that for a driving electric field E_x that is orthogonal to the vertical mirror, the generated nonlinear current is purely transverse. For a driving electric field at an angle ϕ with respect to \hat{x} , the generated nonlinear transverse current $j_T = \bar{\chi} E^2 \cos 3\phi$. The net transverse current in a polycrystalline sample is thus dependent on the distribution of the crystallites in-plane orientation. Note that the small statistics of grains in Hall crosses of finite area (about $1 \times 1 \mu\text{m}^2$ cross area; grain size of about 30 nm) guarantees the non-vanishing of the nonlinear transverse current independent of the distribution. This assumption is confirmed by studying macroscopic, *i.e.* $5 \times 5 \text{ mm}^2$, Bi Hall cross (Supplementary Fig. 4(a)). In particular, transport data demonstrate that this sample does not reveal nonlinear transverse response (Supplementary Fig. 4(b,c)).

Symmetry constraints on the nonlinear Hall effect can be also used to show the one-to-one correspondence between the Berry curvature of the Rashba bands and the disorder-mediated contributions introduced in the preceding Supplementary Theory Notes. Consider the states at a surface containing an evenfold rotation symmetry, *i.e.* with point group \mathcal{C}_{2v} , \mathcal{C}_{4v} or \mathcal{C}_{6v} . The effective Hamiltonian for the surface states up to quadratic order will correspond to a Rashba two-dimensional electron system. However, the trigonal warping term appearing at the (111) surfaces is symmetry-forbidden and the Berry curvature is vanishing. And indeed the concomitant presence of the twofold rotation symmetry \mathcal{C}_2 and time-reversal symmetry Θ implies the presence of the additional combined antiunitary symmetry $\mathcal{C}_2\Theta$ that squares to 1 and transforms \mathbf{k} in itself. Since $\mathcal{C}_2\Theta$ can be represented by a complex conjugation, we obtain that its presence forces the Berry curvature to vanish at any momentum. On the other hand, from the relation $j_\alpha = \chi_{\alpha\beta\gamma} E_\beta E_\gamma$, we have that the presence of a twofold rotation symmetry implies vanishing of all components of the nonlinear conductivity tensor in a two-dimensional system. Combining these results, we obtain that surface states realizing a Rashba two-dimensional electron system must have a vanishing nonlinear Hall effect in the absence of Berry curvature. Consequently, all disorder-mediated contributions to the nonlinear Hall must be directly related to the strength of the Berry curvature effect and, in particular, to the Berry curvature triple.



Supplementary Fig. 4. **Harmonic measurement of a macroscopic 100-nm-thick Bi Hall cross prepared on a polymeric foil.** (a) Photo of the macroscopic 100-nm-thick Bi thin film structured into a Hall cross on mechanically flexible 25- μm -thick Kapton foil (DuPont, USA). Lateral dimensions of the Hall cross are $5 \times 5 \text{ mm}^2$. The middle part of the device is covered with GE-varnish (Oxford Instruments, UK) to prevent bismuth thin film from oxidation. Electrical measurements are done with Tensormeter RTM2 (Tensor Instruments, HZDR Innovation GmbH, Germany). Transverse voltage measured at the (b) first harmonic and (c) second harmonic. The measurements are done at the fundamental frequency of 787 Hz. Contact pads are realized with 100-nm-thick gold thin films.

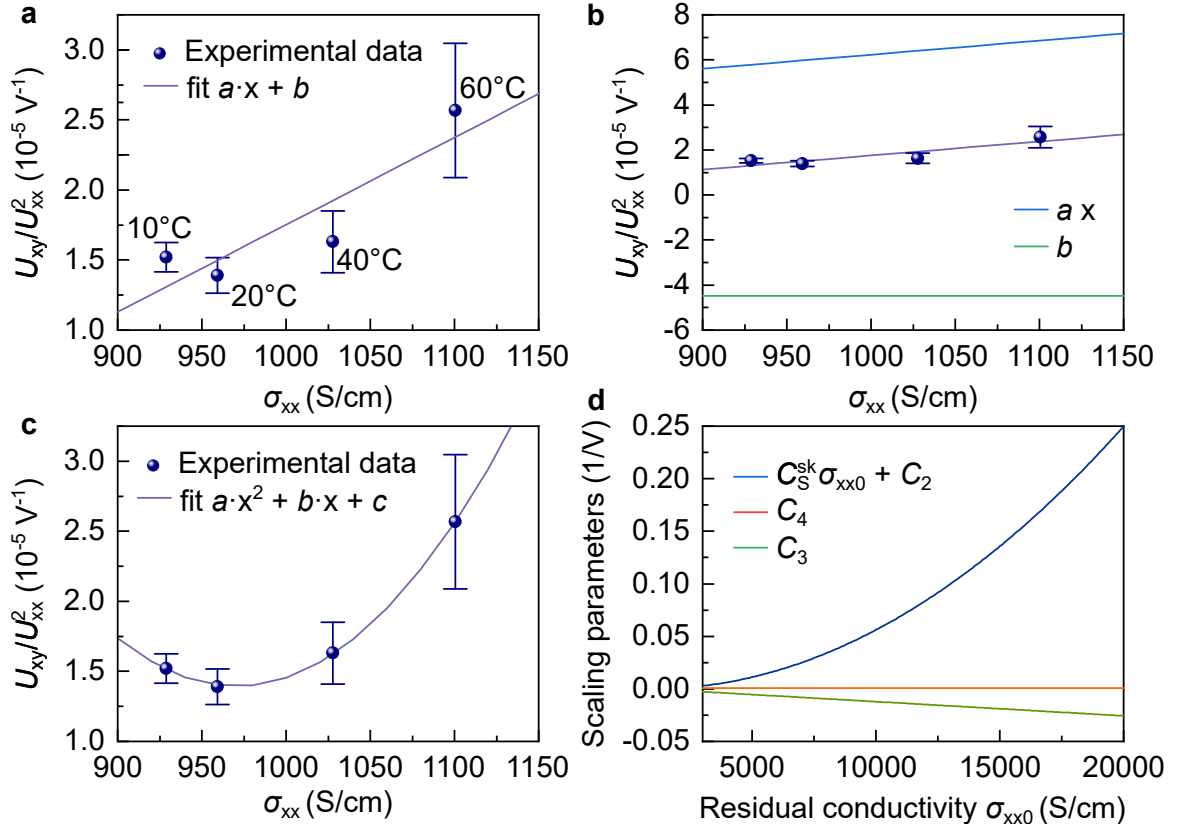
F. On the difference between dissipative and dissipationless (non)linear transverse electrical responses.

To elucidate the difference between dissipative and dissipationless transverse electrical responses, we first consider the linear transport regime. In particular let us assume that in a \mathcal{C}_2 -symmetric material a current is injected in a direction different from a principal crystallographic direction and a linear transverse voltage is obtained. The corresponding transverse conductivity is related to the longitudinal conductivity by a rotation of the conductivity tensor. Hence it will be dissipative. Such dissipative transverse voltages can be also completely unrelated to longitudinal voltages. Consider for example a crystalline system with a trivial \mathcal{C}_1 point group symmetry – the only symmetry in the space group are discrete translations. This situation is realized in, for instance, (111)-grown $\text{LaAlO}_3/\text{SrTiO}_3$ interfaces [see Ref. [12]] since the cubic-to-tetragonal structural phase transition of SrTiO_3 involving antiferrodistortive oxygen octahedron rotations breaks all mirror and rotation symmetries. The linear conductivity tensor is characterized by the presence of a transverse component, which in a constant relaxation time approximation, is related to the (non-vanishing after integration) velocity product $v_x v_y$. As a result, a transverse voltage can be produced even when a current is injected along a principal crystallographic direction.

There is a key physical difference between conventional Hall voltages and these time-reversal symmetric transverse voltages. Transverse voltages can be in fact differentiated by looking at whether or not they contribute to the dissipated power $\mathbf{j} \cdot \mathbf{E}$. An antisymmetric part of the transverse conductivity with $\sigma_{xy} = -\sigma_{yx}$ does not contribute to the dissipative power. On the contrary, the symmetric part of the transverse conductivity with $\sigma_{xy} = \sigma_{yx}$ is dissipative. These properties combined with Onsager relations $\sigma_{xy}(B) = \sigma_{yx}(-B)$ imply that any transverse voltages observed in time-reversal symmetric conditions must be dissipative.

It would be then natural to associate Hall voltages with dissipationless transverse currents. This, however, is not the case. Consider the well-known planar Hall effect conventionally observed in ferromagnets with strong spin-orbit coupling. The planar Hall effect has gained significant attention in recent years in relation with time-reversal symmetric Weyl semimetals where it originates from the so-called chiral anomaly [see Ref. [13]]. In the planar Hall effect, coplanar electric and magnetic fields lead to a transverse voltage. However, such voltage is dissipative for the simple reason that it is unchanged if the direction of the applied magnetic field is reversed. Furthermore, the transverse voltage is connected to the anisotropic longitudinal magnetoresistance. This effect thus represents a prime example of a transverse electrical response with the same underlying mechanism as the longitudinal one and to which we conventionally refer to as Hall.

The question that now arises is whether the transverse nonlinear response, which we observe in our Bi thin films, can be dubbed as a nonlinear Hall voltage or should be called in more broad terms as electrical second-harmonic generation. The nonlinear transverse response of a threefold rotation symmetric system is dissipative due to the equivalence $\chi_{xyx} = -\chi_{yxx}$ [see Ref. [8]] that prohibits a Berry curvature dipole. However, as shown above, it can be entirely related to another Berry curvature related quantity: the Berry curvature triple. Furthermore, the recent study Ref [14] has dubbed the nonlinear electrical transverse responses appearing at the threefold symmetric surfaces of Bi_2Se_3 as nonlinear Hall. Finally, the classical geometry-induced second-order transverse responses has been also named Hall [see Ref. [15, 16]] due to the bent electron trajectories similar to those appearing in the conventional Hall effect. For these reasons, we refer to the nonlinear transverse response in Bi as nonlinear Hall.



Supplementary Fig. 5. **Scaling of the nonlinear transverse voltage $U_{xy}^{2\omega}$ vs. longitudinal bulk conductivity σ_{xx} of 100-nm-thick bismuth thin films prepared on Si/SiOx(500 nm).** Nonlinear transverse voltage and longitudinal bulk conductivity are measured of the same Bi Hall cross structure upon varying the measurement temperature. Temperature is indicated in the figure panel for each data point. In panel (a) the experimental data points are overlaid with the fit $U_{xy}/U_{xx}^2 = a \cdot \sigma_{xx} + b$. Fit coefficients are: $a = (6.2 \pm 2.2) \times 10^{-8} \frac{\text{cm}}{\text{\AA}}$; $b = (4.5 \pm 2.3) \times 10^{-5} \frac{1}{\text{V}}$. Panel (b) shows the individual components of the fit. In panel (c) the experimental data points are overlaid with the fit $U_{xy}/U_{xx}^2 = a \cdot \sigma_{xx}^2 + b \cdot \sigma_{xx} + c$. Fit coefficients are: $a = (6.9 \pm 0.3) \times 10^{-10} \frac{\text{V} \cdot \text{cm}^2}{\text{\AA}^2}$; $b = (-1.35 \pm 0.05) \times 10^{-6} \frac{\text{cm}}{\text{\AA}}$; $c = (6.7 \pm 0.3) \times 10^{-4} \frac{1}{\text{V}}$. (d) Scaling terms for the static ($C_S^{sk} \sigma_{xx0} + C_2$), dynamic (C_4) and mixed (C_3) charge carriers scattering obtained from the fit shown in panel (c) vs residual conductivity σ_{xx0} . Transverse voltage $U_{xy}^{2\omega}$ is measured at the second harmonic. Longitudinal voltage U_{xx} and longitudinal conductivity σ_{xx} are measured at the first harmonic. Transport measurements are done at the fundamental frequency of 787 Hz. The measurement was done using lock-in amplifier HF2LI (Zurich Instruments AG, Switzerland).

G. Scaling of the nonlinear Hall effect in Bi thin films

In this section we investigate the scaling of the nonlinear Hall effect in polycrystalline bismuth thin films. For good metals, dynamic (electron-phonon) scattering sources can compete with the impurity scattering sources, analyzed in Supplementary Theory Notes B,C,D. In this respect, a scaling analysis of the nonlinear Hall effect can help in unveiling the relative role of static impurity and phonon scattering processes.

We follow Ref. [7] and recall that for our system the absence of a Berry curvature dipole implies the existence of three different scaling terms in the nonlinear Hall conductivity, χ_{yxx} . Nonlinear side jump contributes as $\chi_{yxx}^{sj} \propto \rho_i / \rho_{xx}^2$. Here ρ_i is the resistivity of source i [see Ref. [17]] that is connected to the total resistivity by Mathiessen's rule $\sum_i \rho_i = \rho_{xx}$. Note also that the nonlinear Hall contribution related to the interband Berry connection introduced in Ref. [11] scales in the same manner as the side jump and can be thus included in χ_{yxx}^{sj} . The third-order skew scattering (see Supplementary Theory Note D) instead scales as $\chi_{yxx}^{sk} \propto \rho_i / \rho_{xx}^3$, where the cubic dependence on ρ_{xx} follows from the fact that $\chi_{yxx}^{sk} \propto \tau^3$ while the ρ_i factor is associated to the third-order scattering rate. Finally, the skew scattering contribution due to the antisymmetric part of the fourth-order scattering rate scales as $\chi_{yxx}^{sk,4} \propto \rho_i \rho_j / \rho_{xx}^3$. Using the relations $\sigma_{yy} E_y = \sigma_{xx} E_y = \chi_{yxx} E_x^2$, we can express the ratio between the second-harmonic transverse voltage $U_{xy}^{2\omega}$

and the square of the first-harmonic longitudinal voltage $U_{xx}^{1\omega}$ as

$$\frac{U_{xy}^{2\omega}}{(U_{xx}^{1\omega})^2} = \chi_{yxx}\rho_{xx} = \sum_i C_i^{sj} \frac{\rho_i}{\rho_{xx}} + C_S^{sk} \frac{\rho_S}{\rho_{xx}^2} + \sum_{ij} C_{ij}^{sk,4} \frac{\rho_i \rho_j}{\rho_{xx}^2} \quad (54)$$

This analysis is in agreement with Ref. [7]. In the equation above, we introduced the coefficients C quantifying the source-dependent side jump and skew scattering contributions. Moreover, we assumed that in the third-order skew scattering only the contribution due to static impurities C_S is relevant [see Ref. [17, 18]].

First, we assume that there is a single source of scattering due to static impurities. A similar assumption was made for Bi_2Se_3 in Ref. [5]. In this case, Eq. 54 reduces to

$$\frac{U_{xy}^{2\omega}}{(U_{xx}^{1\omega})^2} = (C_S^{sj} + C_S^{sk,4}) + C_S^{sk} \sigma_{xx}, \quad (55)$$

where we have used that $\rho_S = \rho_{xx}$. We have fitted the experimental data obtained of a Bi Hall cross by measuring transport at different temperatures with the linear behavior of the equation above [see Supplementary Fig. 5(a,b)]. We find that the skew scattering C_S^{sk} and the side jump C_S^{sj} coefficients have opposite sign and are comparable in magnitude. Despite the similar values of the longitudinal conductivities, there is thus a qualitative difference with the case of Bi_2Se_3 where the third-order skew scattering was argued to be more relevant than the side jump contribution and the fourth-order skew scattering. Importantly, the authors of Ref.[5] have considered a different type of scaling for the third-order skew scattering $\propto \sigma_{xx}^2$, in disagreement with our analysis and Ref. [7].

We now show that such quadratic term $\propto \sigma_{xx}^2$ appears when considering two sources of scattering: static impurities and phonons. The resistivities associated to these two scattering sources correspond respectively to the zero-temperature residual resistivity ρ_{xx0} and $\rho_{xxT} = \rho_{xx} - \rho_{xx0}$. Then the scaling of Eq. 54 can be written as

$$\frac{U_{xy}^{2\omega}}{(U_{xx}^{1\omega})^2} = \frac{C_S^{sk} \sigma_{xx0} + C_2 + C_4 - C_3}{\sigma_{xx0}^2} \sigma_{xx}^2 + \frac{C_3 - 2C_4}{\sigma_{xx0}} \sigma_{xx} + C_4 \quad (56)$$

In the equation above, we introduced new scattering coefficients $C_{2,3,4}$ with

$$\begin{aligned} C_2 &= C_S^{sj} + C_{SS}^{sk,4} \\ C_3 &= C_S^{sj} + C_{ph}^{sj} + C_{Sph}^{sk,4} \\ C_4 &= C_{ph}^{sj} + C_{phph}^{sk,4}, \end{aligned}$$

where the subscript S, ph stands for static impurities and phonons, respectively. Note that the coefficient C_2 depends only on static impurity scattering, similarly to C_S^{sk} . On the contrary, the coefficient C_4 depends only on dynamic scattering processes. Finally, C_3 is a mixed term. Taking into account the scaling of Eq. 56, we obtain a much better fit, as reported in Supplementary Fig. 5(c,d). Furthermore, from our fits we can estimate the dynamic parameter C_4 , a purely static scattering parameter $C_S^{sk} \sigma_{xx0} + C_2$ as well as the mixed term C_3 . In Supplementary Fig. 5(e) we show their behavior as a function of the residual conductivity of bismuth, σ_{xx0} . For residual conductivities that are one order of magnitude larger than the measured room-temperature conductivity, the static scattering term $C_S^{sk} \sigma_{xx0} + C_2$ is much larger than the two other coefficients. This implies that for large enough residual conductivities the nonlinear Hall signal will be dominated by static impurity scattering. Note that in the literature values as high as $\sigma_{xx0} \simeq 10^6 \text{S/cm}$ have been reported for the residual conductivity of Bi [see Ref. [19]].

In conclusion, both our scaling analyses point to a dominant role played by static impurities with no particular indication of a preferred skew scattering mechanism. As discussed above, both side jumps and skew scattering mechanisms originate from the Berry curvature triple. We also note that according to our scaling laws, which agree with Ref. [7], it would not be possible to individuate a predominant skew scattering mechanism in Bi_2Se_3 due to the quadratic scaling of $U_{xy}^{2\omega}/(U_{xx}^{1\omega})^2$.

H. Thermal effects in bismuth thin films due to charge current

To estimate relevance of thermal effects in our 100-nm-thick Bi films induced by charge current, we use a bimaterial thermal model proposed in [20]. The model considers a conductive thin film material through which the current flows and an electrically insulating substrate. The thermal state of the system is found by solving the heat balance equations in which the thermal energy supplied to the system by Joule resistive heating (i) increases its temperature and (ii) is lost via thermal conduction and convection to the environment.

Joule heating of an electrically resistive material with resistance R due to flowing charge current I is described with the following equation:

$$Q = RI^2\Delta t = \rho \frac{l_f}{d_f a_f} I^2 \Delta t, \quad (57)$$

where ρ - resistivity of the thin film material, Δt - time, and l_f , a_f and d_f stand for length, width and thickness of the conductive thin film. The energy Q is accumulated by the material as thermal energy resulting in an increase of its temperature T from the initial temperature T_0 for ΔT :

$$Q = Cm\Delta T, \quad (58)$$

where C - specific heat of the material (thin film or substrate) and m - mass. In addition, thermal energy Q is lost by the thermal conduction to the substrate and by convection to the environment (air). The amount of heat transferred from the thin film to the substrate can be described as

$$Q_c = \frac{k_s S_s}{d_s} (T_f - T_s) \Delta t, \quad (59)$$

where k_s - thermal conductivity of the substrate, S_s - contact surface area of the thin film with the substrate, T_f and T_s - temperatures of the film and substrate, respectively. The heat lost via convection to the environment is expressed as:

$$Q_h = hS(T - T_0)\Delta t, \quad (60)$$

where h - convection coefficient, S - surface area, T and T_0 - temperatures of surface and environment.

The equation of the heat balance for such a system takes the following form:

$$\begin{cases} Q_0 = Q_f + Q_c + Q_{hf} \\ Q_c + Q_s + Q_{hs} = 0 \end{cases} \quad (61)$$

By combining expressions (57)-(60), we obtain equation, which describes the time evolution of the temperature of the metal thin film:

$$\begin{cases} \frac{\Delta T_f}{\Delta t} + \left(\frac{k_s S_s}{m_f C_{pf} d_s} + \frac{h S_f}{m_f C_{pf}} \right) (T_f - T_0) - \frac{k_s S_s}{m_f C_{pf} d_s} (T_s - T_0) = \frac{\rho_f l_f I^2}{d_f a_f m_f C_{pf}} \\ \frac{\Delta T_s}{\Delta t} + \left(\frac{k_s S_s}{m_s C_{ps} d_s} + \frac{h S_s}{m_s C_{ps}} \right) (T_s - T_0) - \frac{k_s S_s}{m_s C_{ps} d_s} (T_f - T_0) = 0. \end{cases} \quad (62)$$

Material parameters used for calculations are listed in Table II. The later stack consists of thick Si substrate capped with 100-nm-thick Bi thin film. Environment temperature is fixed at room temperature of $T_0 = 25^\circ\text{C}$. The convection coefficient us taken to be 30.

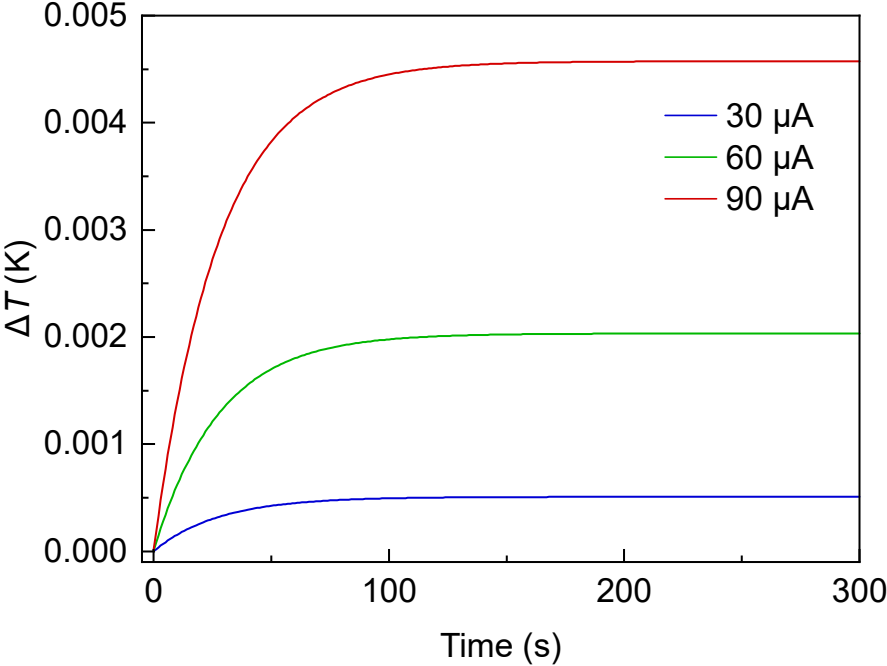
TABLE II. Material parameters used for estimation of the charge current induced thermal effects in bismuth thin films on a silicon substrate.

	Material	Dimentions			Physical properties		
		Length l	Width a	Thickness d	Density ρ	Specific heat capacity C_p	Thermal conductivity k
Thin film	Bi	32 μm	1.42 μm	100 nm	9.78 g/cm ³	123.5 J/(kg K)	7.97 W/(m K)
Substrate	Si	14.5 mm	11 mm	0.5 mm	2.34 g/cm ³	711 J/(kg K)	150.7 W/(m K)

Solving Eq. (62) leads to the temporal dependence shown in Supplementary Fig. 6. For the temperature induced effects to cause any harmonic distortions (generate parasitic AC signals), they have to take place at the timescale

of half-period of the sourcing signal. In our experiments, we work with AC current at the fundamental frequency of 787 Hz with a period of 1.2 ms. At this timescale at maximum current amplitude of $90 \mu\text{A}$, the expected thermally induced signal would be of about 300 pV in the longitudinal channel, which is below the measurement accuracy of our setup.

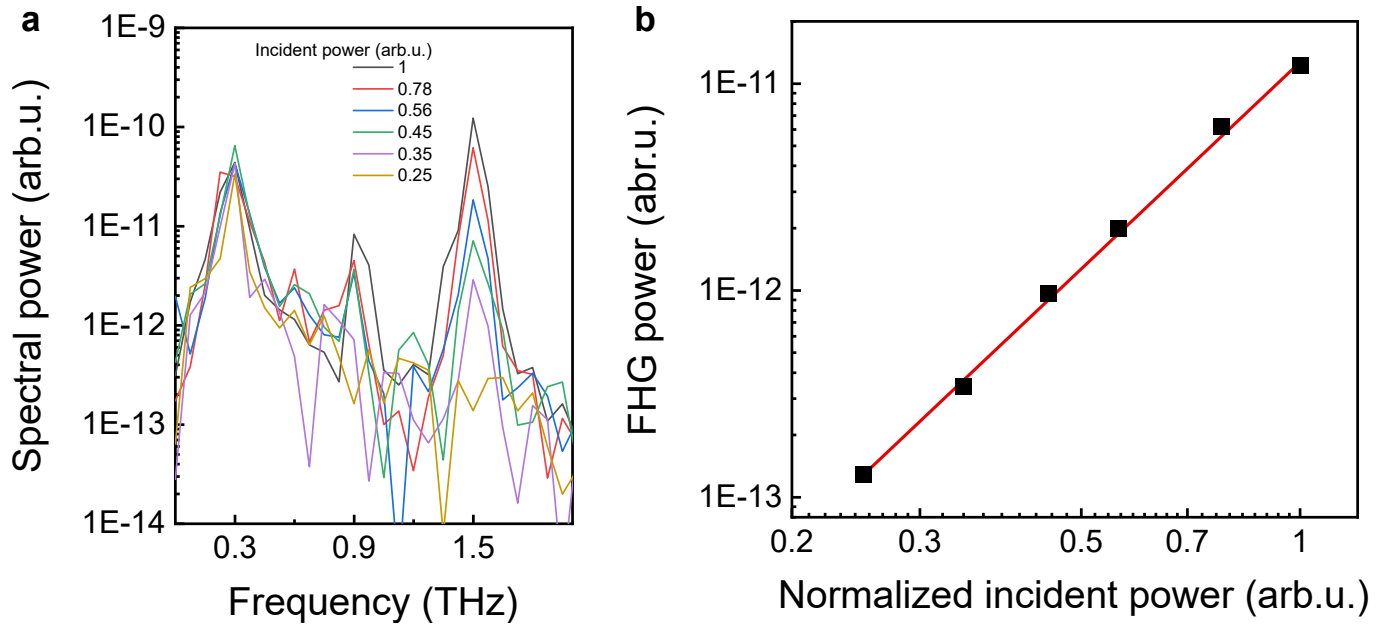
At the timescale of seconds, the temperature difference induced by the Joule heating reaches 4.5 mK at $90 \mu\text{A}$ current amplitude. This effect will not induce any harmonic distortions but will cause constant change in the thin film temperature (similar to supplying DC current $I_{\text{DC}} = \text{RMS}(I_{\text{amp}})$). In the longitudinal channel this effect will cause nonlinearities at the fundamental harmonics of about 150 nV, which is 0.7 ppm of the signal measured of this channel. We consider this contribution to the total measured voltage to be negligible.



Supplementary Fig. 6. **Joule heating in bismuth thin films on 0.5-mm-thick silicon substrate.** Charge current induced heating of a 100-nm-thick bismuth thin film structured into a $1.2 \mu\text{m}$ wide Hall cross structure. The data is shown for the case of dc current of different amplitudes flowing in the Hall cross.

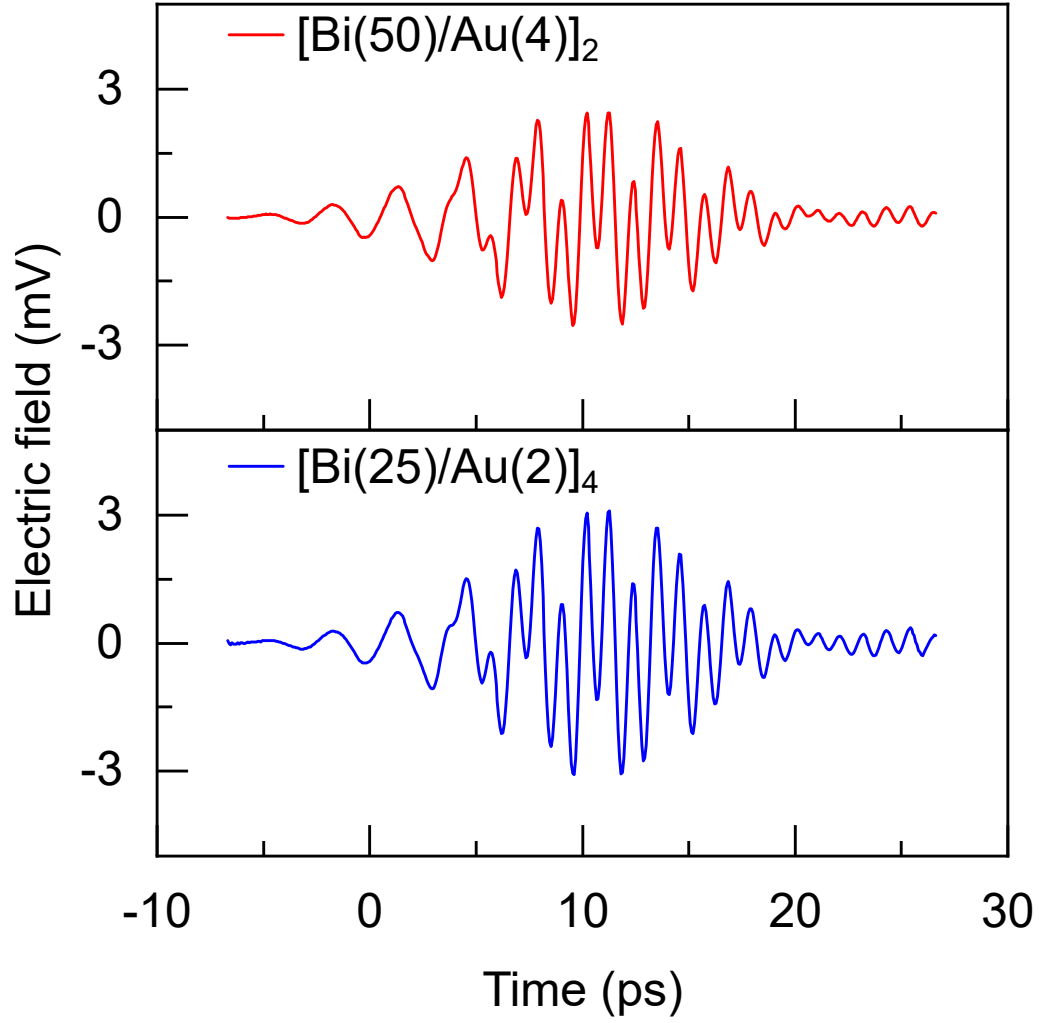
III. SUPPLEMENTARY THZ HIGH HARMONIC GENERATION MEASUREMENTS

A. THz fifth harmonic generation in Bi thin films



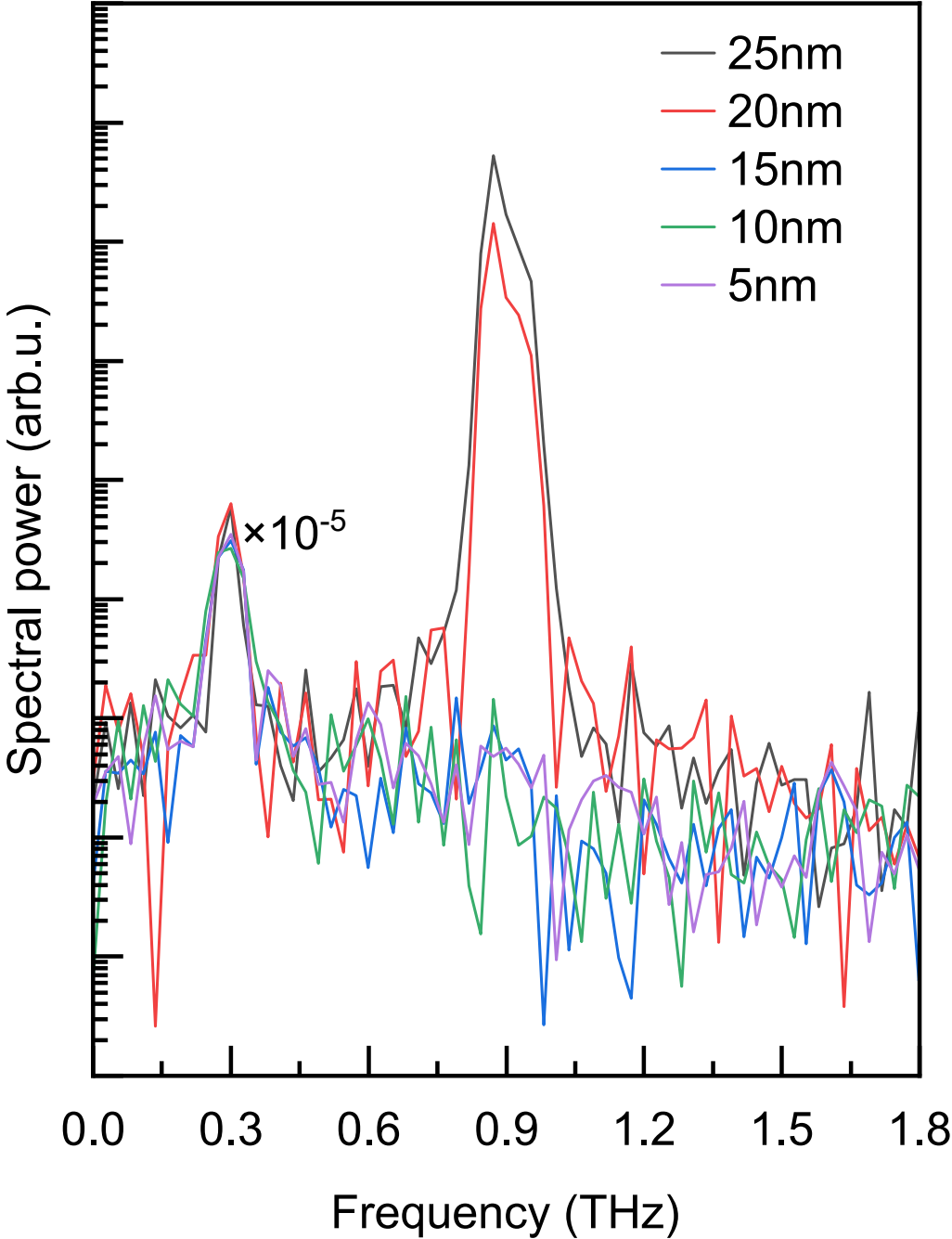
Supplementary Fig. 7. **THz fifth harmonic generation (FGH) in Bi(100 nm)/Au(2 nm) thin films prepared on quartz glass.** (a) Power spectrum of the transmitted THz pulse at different incident power. The fundamental frequency of the incident light at 0.3 THz is attenuated by 5 orders of magnitude. Generation of the fifth harmonic is observed at 1.5 THz. (b) Spectral power of the generated fifth harmonic versus normalized power of the incident pulse.

B. THz third harmonic generation in Bi/Au heterostructures



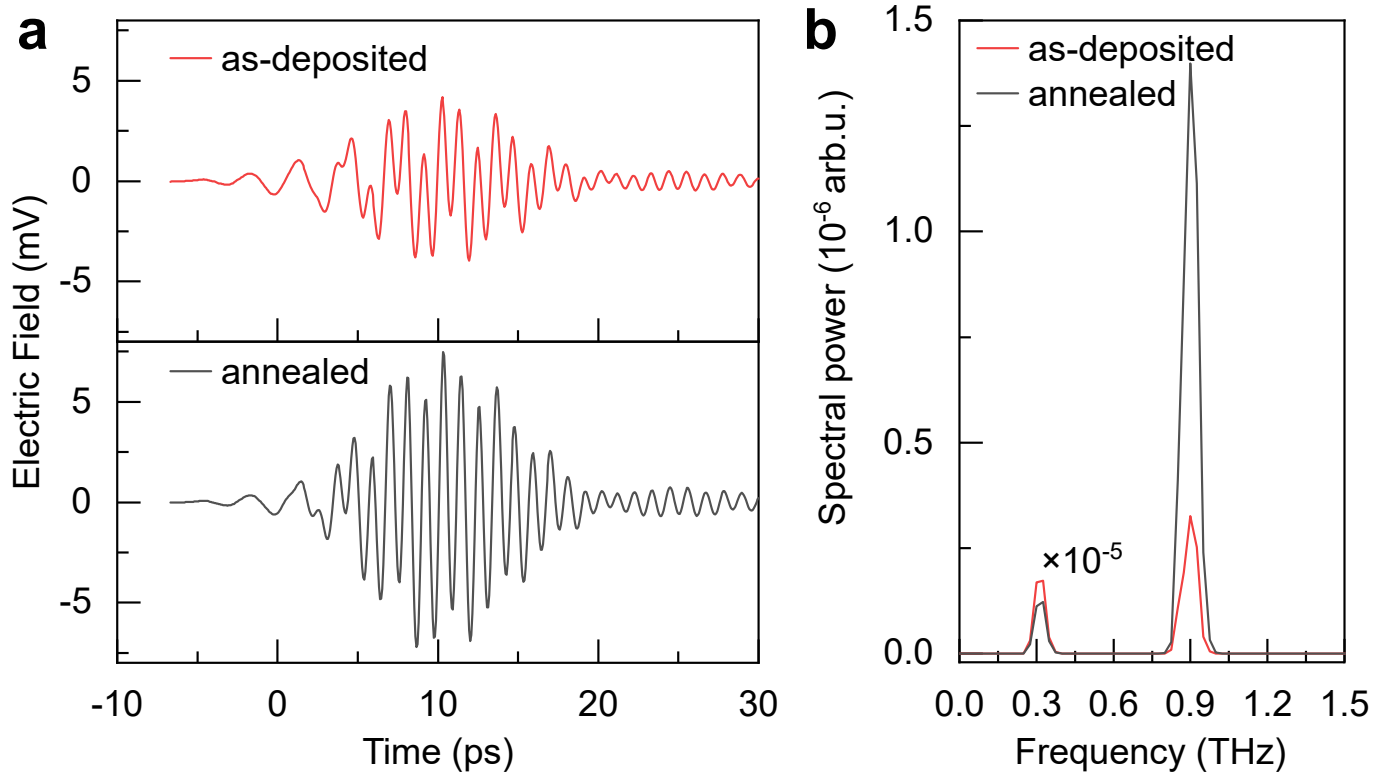
Supplementary Fig. 8. **THz third harmonic generation (THG) in Bi/Au heterostructures (extended film) prepared on quartz glass.** Electric field profile in time domain of the transmitted THz radiation. We note that the light passed through a 300 GHz band-pass filter, which attenuated the fundamental harmonic by 5 orders of magnitude.

C. Bismuth film thickness dependence of the THz third harmonic generation



Supplementary Fig. 9. **THz third harmonic generation (THG) in Bi(x nm)/Au(2 nm) thin films prepared on quartz glass.** Transmitted spectral power measured after Bi thin films of different thickness x varying from 5 to 25 nm. Third harmonic generation is observed only in thin films thicker than 15 nm. The absence of the THG in thinner bismuth films might be related to the island-like growth of the material or to the hybridization of the two surfaces of bismuth, opening the gap in the Rashba type surfaces - therefore quenching the THz THG. The latter is an additional confirmation of the surface contribution to the measured THz third harmonics signal.

D. Effect of thermal annealing on THz third harmonic generation



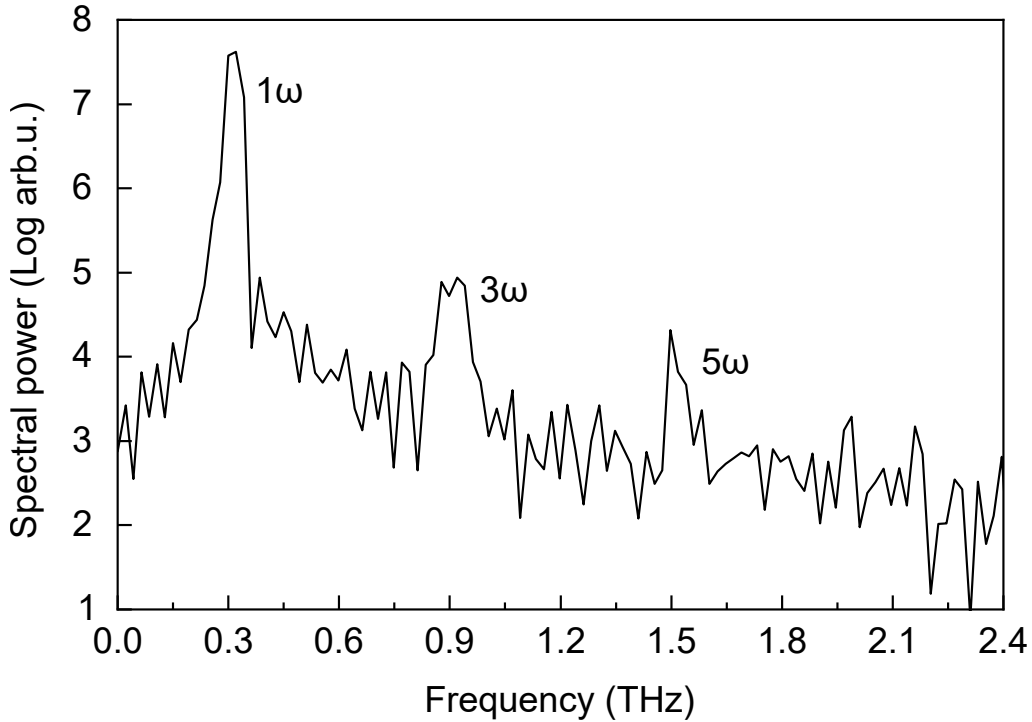
Supplementary Fig. 10. **Effect of thermal annealing on THz third harmonic generation in Bi(100 nm)/Au(2 nm) thin films prepared on quartz glass.** (a) Transmitted THz signal in as-deposited (top panel) and thermally annealed in vacuum at 200°C for 3 h (bottom panel) thin film samples. (b) Power spectrum of the transmitted THz radiation. THz THG is enhanced in the sample after thermal annealing in vacuum. The observed enhancement of the efficiency of the THz THG is attributed to the enhancement of the quality of the (001) texture of the thin films. The fundamental THz signal ($\omega = 300$ GHz) is attenuated by 5 orders of magnitude.

E. Optical second-harmonic generation at THz frequencies in curved devices

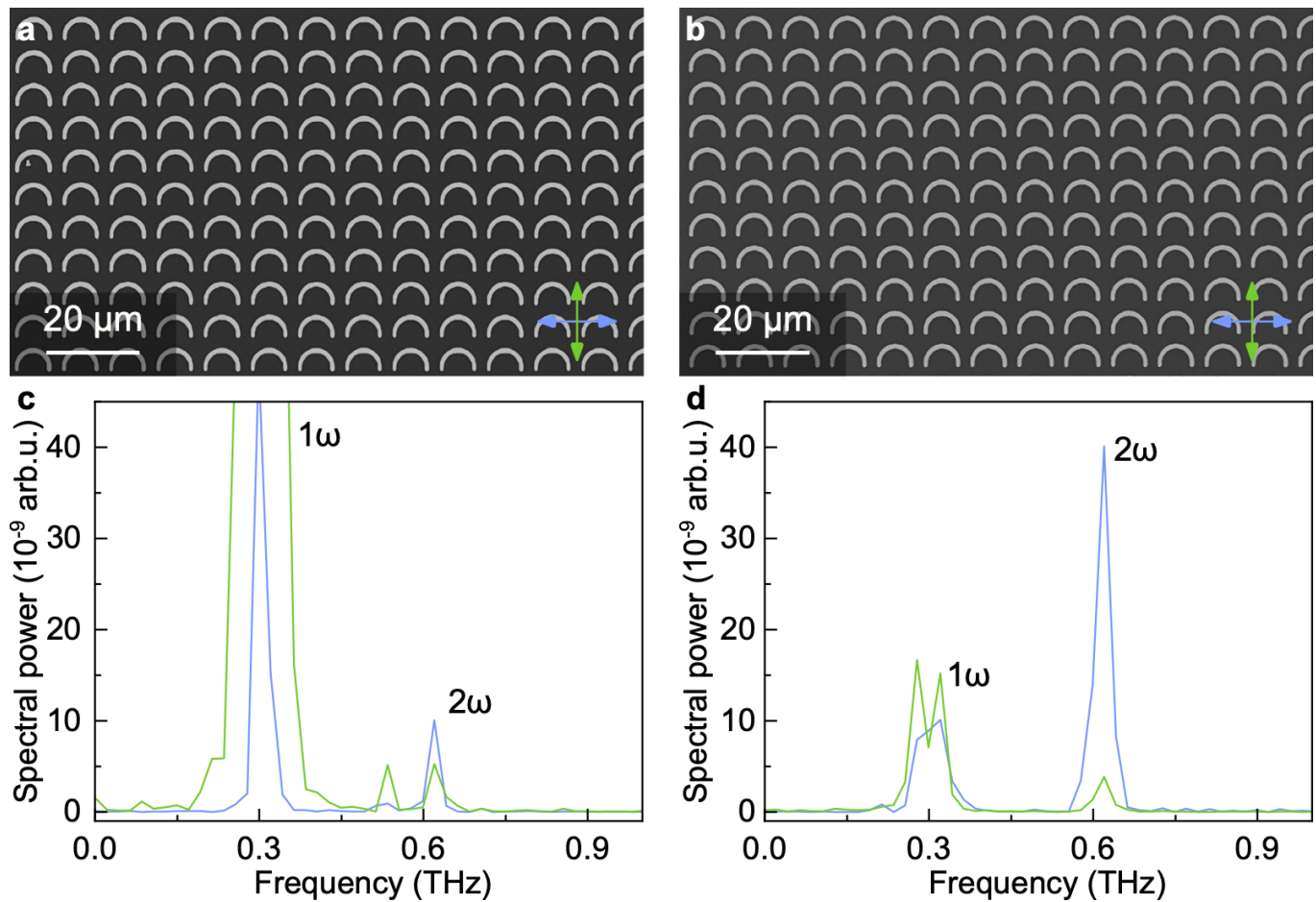
We found conclusive evidence of the THz SHG in samples consisting of arrays of bismuth arcs. Due to small signal, the measurement even on arc arrays required the use of an accelerator TELBE at the HZDR. The resulting data are shown in Fig. 3 of main text. One can distinguish a clear second harmonic peak at 0.6 THz (fundamental frequency: 0.3 THz). Importantly, we have also performed a comparative measurement with monolayer graphene using the same experimental setup [see Supplementary Fig. 11]. We clearly observe third and fifth harmonic generation whereas even harmonics are absent. This is completely compatible with the centrosymmetric nature of graphene that precludes a second-harmonic peak.

We also observe a strong polarization dependence in the THz SHG signal of Bi arcs. As shown in Fig. 3 of the main text, the second-harmonic peak is enhanced when the incident electric field is polarized along the arc, *i.e.* perpendicular to the symmetry axis of an individual arc structure. Based on this observation, we can argue that the geometry-induced nonlinear effects are much stronger than the intrinsic nonlinearities of the surface states. The intrinsic contribution is expected to generate peaks of comparable power spectrum for the two orthogonal polarization because the longitudinal nonlinear conductivity component χ_{yyy} has magnitude equal to the transverse one χ_{yxx} [see Supplemental Theory Note E]. The strong polarization dependence therefore provides signature of the connection between the nonlinear transport regulated by the geometric NLHE and optical SHG at sub-millimeter frequencies.

Furthermore, we can parallel the presence of the geometric NLHE expected in various elemental materials with ubiquity of THz SHG in devices with curved stripes. We performed additional high-harmonic generation measurements at TELBE accelerator using arrays of arcs made of 20-nm-thick gold. The results shown in Supplementary Fig. 12 prove that even though Au thin films do not have a visible THz THG, our arrays of arcs display a THz SHG peak at a much higher intensity level than the array of bismuth arcs (shown in Fig. 3(f) in the main text). Its features, namely the polarization dependence, is similar to elemental bismuth.



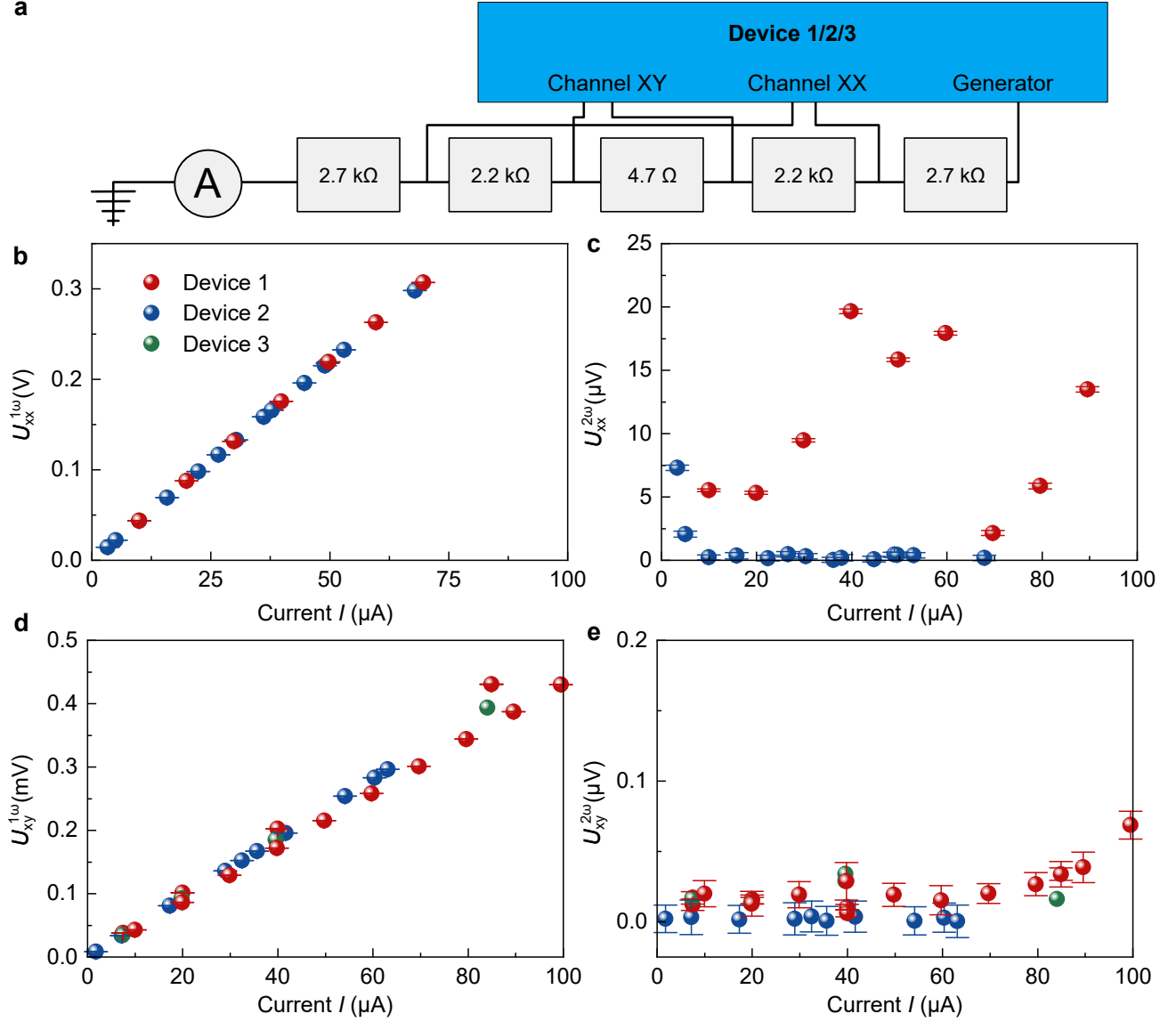
Supplementary Fig. 11. **THz higher harmonic generation in a monolayer graphene.** Power spectrum of the THz radiation transmitted through a monolayer graphene transferred to quartz glass. Third and fifth harmonics are observed.



Supplementary Fig. 12. **THz second harmonic generation (SHG) in arrays of arcs of 20-nm-thick Au prepared on a high purity silicon substrate.** (a,b) Scanning electron microscopy images of two samples of the arrays of arcs prepared using thin film deposition of 20-nm-thick Au and optical lithography to realize arcs with inner radius of $3\ \mu\text{m}$ and width of line of about $1\ \mu\text{m}$. Arrows in the bottom-right corner indicate polarization of the incident THz pulse. (c,d) Power spectrum of the transmitted THz radiation for the samples shown in panels (a) and (b), correspondingly (the data is shown in the same scaling as in Fig.3(f) of the main text). The intensity of the fundamental peak is suppressed by two band-pass filters. The background for each curve is also suppressed by subtracting measurements done in antiparallel polarization of THz pulse relative to the symmetry axis of the arcs, *i.e.* $0 - 180^\circ$ and $90 - 270^\circ$. The color of lines in panels (c,d) corresponds to the color of arrows in panels (a,b) indicating the polarization of the incident light.

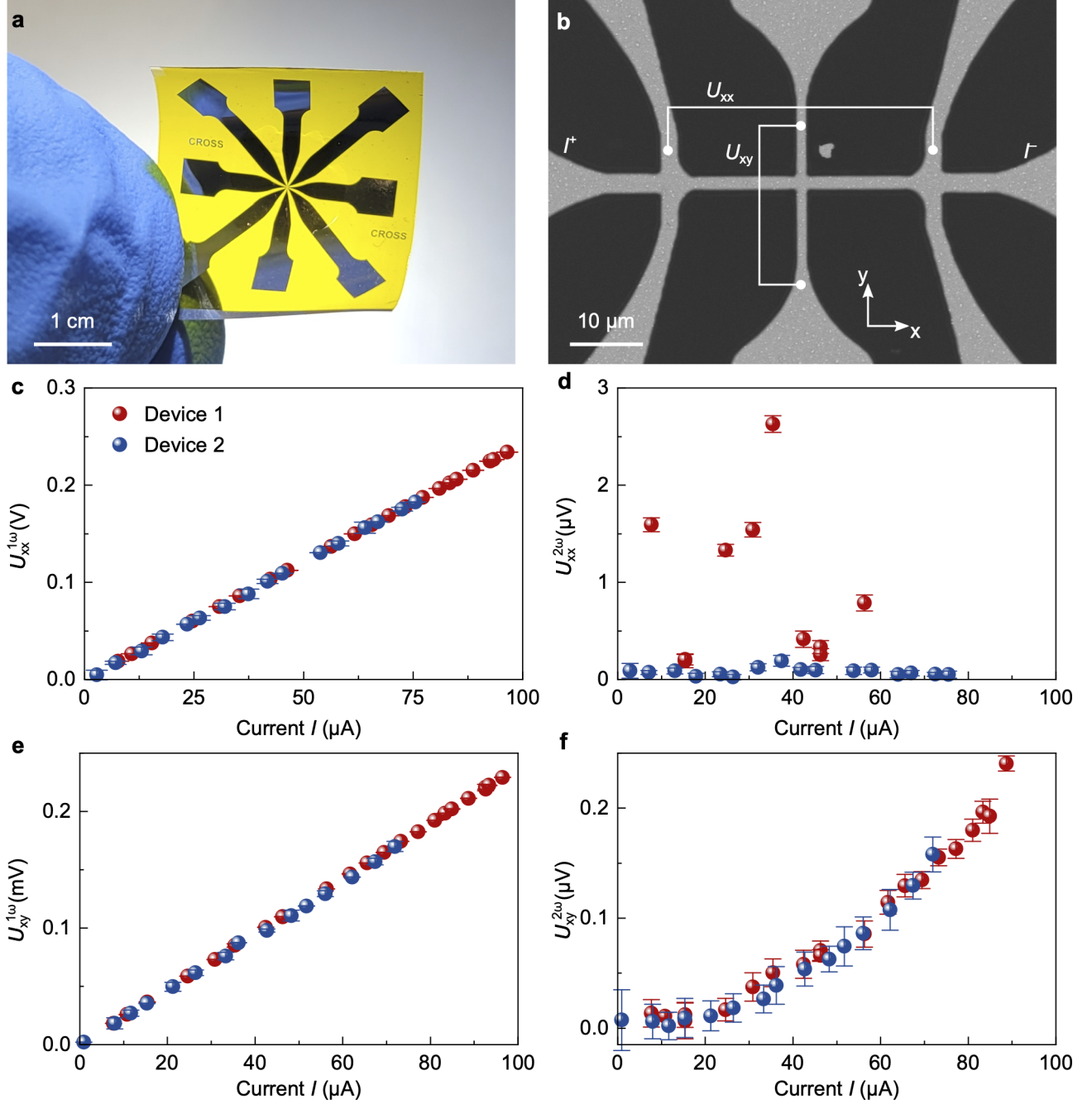
IV. SUPPLEMENTARY TRANSPORT CHARACTERIZATION

A. Harmonic transport measurement of a reference resistor



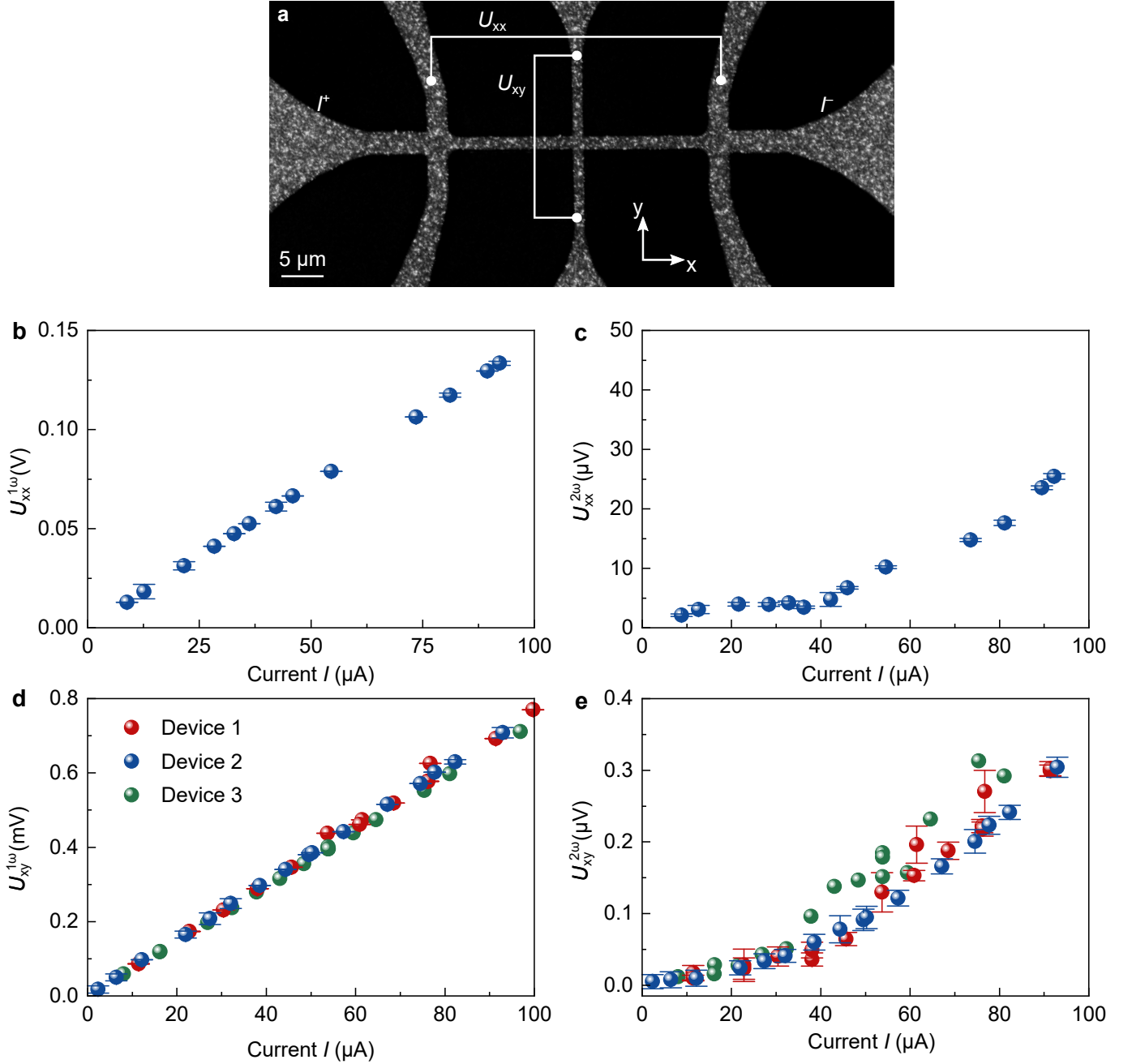
Supplementary Fig. 13. **Harmonic transport measurement of a reference resistor.** The reference measurement is performed of five resistors connected in series. Commercial surface mounted device (SMD) metal film resistors (Nova Electronic GmbH, Germany) were used for this reference measurement. The connection scheme of the resistors to the measurement device is shown in panel (a), A stands for ampermeter. This connection of 5 resistors resembles an electrical equivalent of the Hall cross structure upon measurement of both longitudinal and transverse voltage signals. The circuit mimics electrical properties of our 100-nm-thick Bi-based Hall bar devices rendering similar current and input voltage ranges during the measurement. Device 1: lock-in amplifier HF2LI (Zurich Instruments AG, Switzerland). Device 2: Tensormeter RTM2 (Tensor Instruments, HZDR Innovation GmbH, Germany). Device 3: lock-in amplifier SR860 (Stanford Research Systems, USA). Longitudinal voltage measured at the (b) first harmonic and (c) second harmonic. The first harmonic signal shows Ohmic response to the supplied current. Transverse voltage measured at the (d) first harmonic and (e) second harmonic. The voltage measured in the Channel XY at the second harmonic $U_{xy}^{2\omega}$ is at the level of 20 nV. As nonlinear effects are not expected in reference resistors, we attribute this variation of the $U_{xy}^{2\omega}$ to the noise floor of the measurement setups. The measurements are done at the fundamental frequency of 787 Hz.

B. Harmonic transport measurement of Bi thin films on polymeric foils



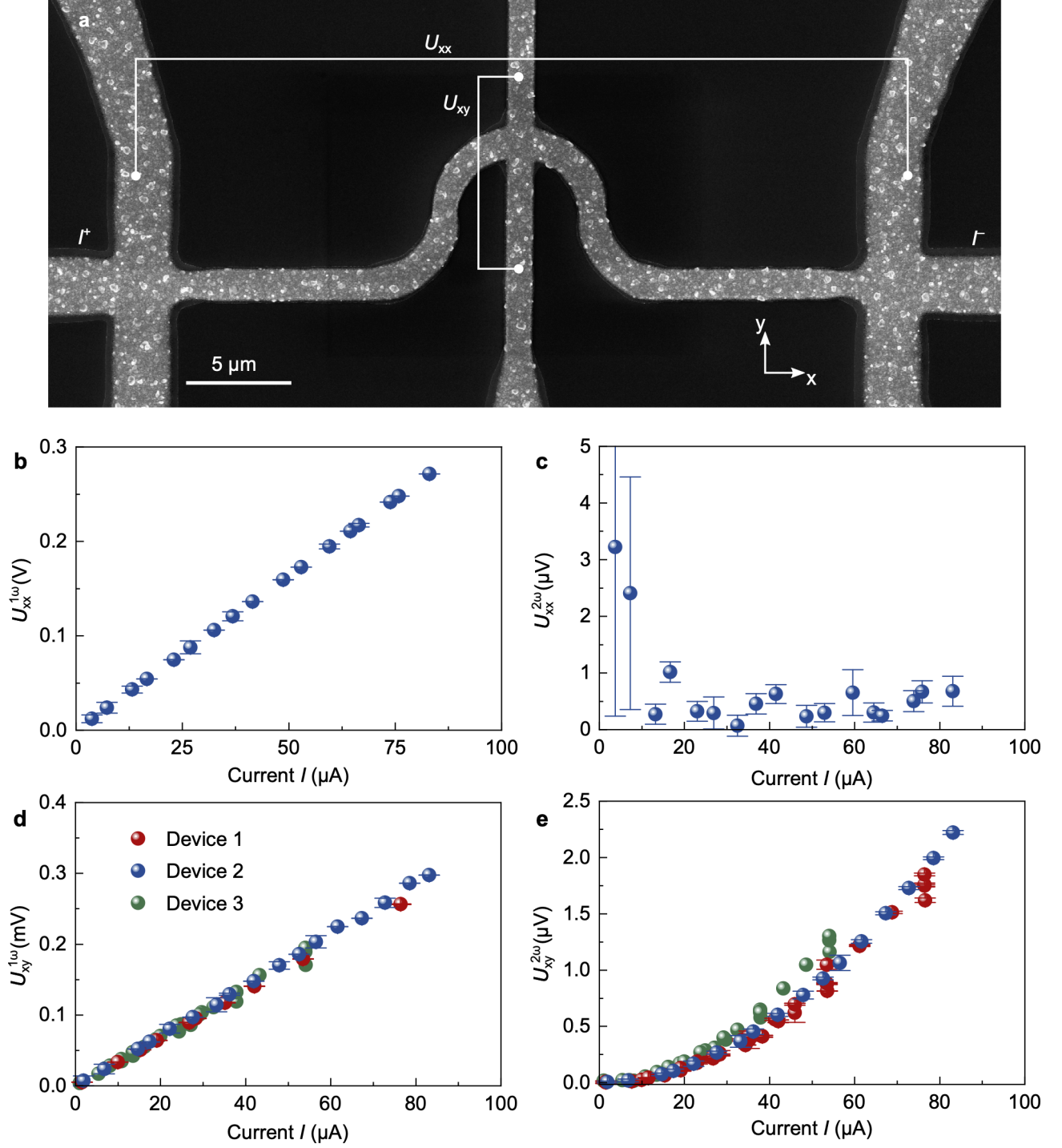
Supplementary Fig. 14. **Harmonic measurement of a 100-nm-thick Bi Hall cross prepared on a polymeric foil.** (a) Photo of the 100-nm-thick Bi thin film structured into a Hall cross on mechanically flexible 25- μm -thick Kapton foil (DuPont, USA). The middle part of the device is covered with GE-varnish (Oxford Instruments, UK) to prevent bismuth thin film from oxidation. (b) Scanning electron microscopy image of the Hall cross structure. Electrical measurements are done with 2 devices. Device 1: lock-in amplifier HF2LI (Zurich Instruments AG, Switzerland). Device 2: Tensormeter RTM2 (Tensor Instruments, HZDR Innovation GmbH, Germany). Longitudinal voltage measured at the (c) first harmonic and (d) second harmonic. Transverse voltage measured at the (e) first harmonic and (f) second harmonic. The measurements are done at the fundamental frequency of 787 Hz.

C. Harmonic transport measurements of Bi Hall crosses using different devices



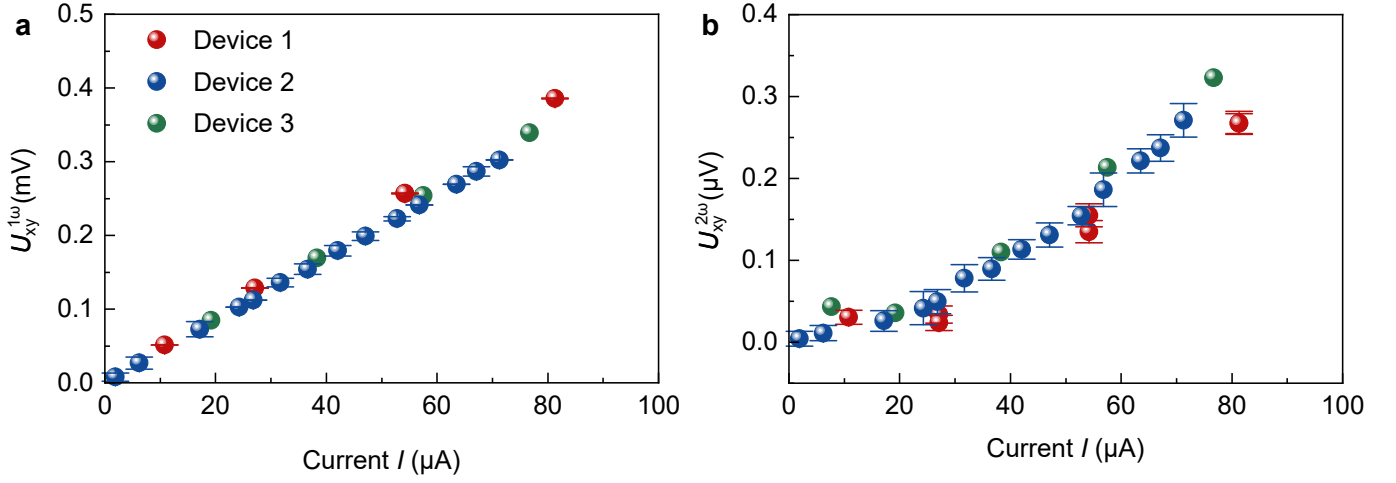
Supplementary Fig. 15. **Harmonic measurement of a 100-nm-thick Bi Hall cross prepared on Si/SiO_x(500 nm).** (a) Scanning electron microscopy image of the Hall cross structure. Electrical measurements of the transverse voltage are done with 3 devices. Device 1: lock-in amplifier HF2LI (Zurich Instruments AG, Switzerland). Device 2: Tensormeter RTM2 (Tensor Instruments, HZDR Innovation GmbH, Germany). Device 3: lock-in amplifier SR860 (Stanford Research Systems, USA). Longitudinal voltage is measured using device 2 only. Longitudinal voltage measured at the (b) first harmonic and (c) second harmonic. Transverse voltage measured at the (d) first harmonic and (e) second harmonic. The measurements are done at the fundamental frequency of 787 Hz.

D. Harmonic transport measurements of arc-shaped Bi Hall bars using different devices



Supplementary Fig. 16. **Harmonic measurement of an arc-shaped ($3 \mu\text{m}$ inner radius) 100-nm-thick Bi Hall bar prepared on Si/SiOx(500 nm).** (a) Scanning electron microscopy image of the arc-shaped Hall bar structure. Electrical measurements of the transverse voltage are done with 3 devices. Longitudinal voltage is measured using device 2 only. Device 1: lock-in amplifier HF2LI (Zurich Instruments AG, Switzerland). Device 2: Tensormeter RTM2 (Tensor Instruments, HZDR Innovation GmbH, Germany). Device 3: lock-in amplifier SR860 (Stanford Research Systems, USA). Longitudinal voltage measured at the (b) first harmonic and (c) second harmonic. Transverse voltage measured at the (d) first harmonic and (e) second harmonic. The measurements are done at the fundamental frequency of 787 Hz.

E. Harmonic transport measurements of Pt Hall crosses using different devices



Supplementary Fig. 17. **Harmonic measurement of a 5-nm-thick Pt Hall cross prepared on Si/SiO_x(500 nm).** Electrical measurements of the transverse voltage are done with 3 devices. Device 1: lock-in amplifier HF2LI (Zurich Instruments AG, Switzerland). Device 2: Tensormeter RTM2 (Tensor Instruments, HZDR Innovation GmbH, Germany). Device 3: lock-in amplifier SR860 (Stanford Research Systems, USA). Transverse voltage measured at the (a) first harmonic and (b) second harmonic. Longitudinal voltage was not measured of this sample. The measurements are done at the fundamental frequency of 787 Hz.

V. FUNDAMENTAL ACHIEVEMENTS OF THIS WORK AND THEIR POTENTIAL TECHNOLOGICAL IMPLICATIONS

We conclude by summarizing the fundamental advances connected with the demonstration of the nonlinear Hall effect at room temperature in bismuth.

- The nonlinear Hall effect of noncentrosymmetric quantum materials has been so far observed in materials with low-energy Dirac (transition metal dichalcogenides, graphene, topological insulator surface states) or Weyl (TaIrTe₄) quasiparticles. An exception is the electron gas formed at the (111) LaAlO₃/SrTiO₃ heterointerface, where, however, the nonlinear Hall effect survives up to $\simeq 30\text{K}$ [see Ref. [12]]. Bismuth is the first material with conventional quasiparticles displaying room temperature nonlinear Hall effect.
- Because of its bulk centrosymmetry, Bi realizes also the first example of a Berry-curvature-free conductive material displaying room-temperature nonlinear Hall effect due to the surface-induced electronic Berry curvature [see Ref. [21]]. This paves the way to exploration of the nonlinear Hall effect in other noble metals, such as Pt, Rh or Ir. We note that we demonstrate that Pt Hall crosses also reveal nonlinear Hall response in transport (Supplementary Fig. 17).
- Our study also shows the first example of nonlinear Hall effect in a material catalogued as an higher-order topological insulator. The connection between topology and Berry curvature-mediated transport effects has been demonstrated so far only in the more conventional (first-order) topological insulator Bi₂Se₃.
- Finally, our study also shows for the first time the realization of the geometric nonlinear Hall effect proposed in Ref. [15, 16] using quasi-one-dimensional arc structures. In this regard, we would like to emphasize that in the semicircle structures studied in Ref. [15], electron trajectories are not constrained to strictly follow circular paths of a given radius.

As it concerns the technological relevance, it must be stressed that the nonlinear Hall effect of quantum materials bears potential for conversion of electromagnetic waves into direct current electricity. This process is a key ingredient for THz and mm-waves technologies. The rectification can be achieved with a diode combined with an antenna, called a rectenna. In conventional rectennas, the AC-DC power conversion efficiency abruptly drops to a few percent at 300 GHz. On the contrary, it has been recently shown [see Ref. [22]] that the power conversion efficiency for a nonlinear Hall rectifier can reach nearly 100%. In this respect, the first demonstration of a room temperature nonlinear Hall effect in an elemental material fabricated with application-relevant thin film technology is of great importance for further device-related explorations.

-
- [1] L. Fu, Hexagonal warping effects in the surface states of the topological insulator Bi_2Te_3 , *Phys. Rev. Lett.* **103**, 266801 (2009).
- [2] A. K. Nayak, J. Reiner, R. Queiroz, H. Fu, C. Shekhar, B. Yan, C. Felser, N. Avraham, and H. Beidenkopf, Resolving the topological classification of bismuth with topological defects, *Science Advances* **5**, eaax6996 (2019), <https://www.science.org/doi/pdf/10.1126/sciadv.aax6996>.
- [3] F. Schindler, Z. Wang, M. G. Vergniory, A. M. Cook, A. Murani, S. Sengupta, A. Y. Kasumov, R. Deblock, S. Jeon, I. Drozdov, H. Bouchiat, S. Guéron, A. Yazdani, B. A. Bernevig, and T. Neupert, Higher-order topology in bismuth, *Nature Physics* **14**, 918 (2018).
- [4] M. Z. Hasan and C. L. Kane, Colloquium: Topological insulators, *Rev. Mod. Phys.* **82**, 3045 (2010).
- [5] P. He, H. Isobe, D. Zhu, C.-H. Hsu, L. Fu, and H. Yang, Quantum frequency doubling in the topological insulator Bi_2Se_3 , *Nature Communications* **12**, 698 (2021).
- [6] N. A. Sinitsyn, A. H. MacDonald, T. Jungwirth, V. K. Dugaev, and J. Sinova, Anomalous Hall effect in a two-dimensional Dirac band: The link between the Kubo-Streda formula and the semiclassical Boltzmann equation approach, *Phys. Rev. B* **75**, 045315 (2007).
- [7] Z. Z. Du, C. M. Wang, S. Li, H.-Z. Lu, and X. C. Xie, Disorder-induced nonlinear Hall effect with time-reversal symmetry, *Nature Communications* **10**, 3047 (2019).
- [8] C. Ortix, Nonlinear Hall effect with time-reversal symmetry: Theory and material realizations, *Advanced Quantum Technologies* **4**, 2100056 (2021).
- [9] V. Brosco, L. Benfatto, E. Cappelluti, and C. Grimaldi, Unconventional dc transport in rashba electron gases, *Phys. Rev. Lett.* **116**, 166602 (2016).
- [10] M. Borunda, T. S. Nunner, T. Lück, N. A. Sinitsyn, C. Timm, J. Wunderlich, T. Jungwirth, A. H. MacDonald, and J. Sinova, Absence of skew scattering in two-dimensional systems: Testing the origins of the anomalous hall effect, *Phys. Rev. Lett.* **99**, 066604 (2007).
- [11] C. Xiao, Z. Z. Du, and Q. Niu, Theory of nonlinear Hall effects: Modified semiclassics from quantum kinetics, *Phys. Rev. B* **100**, 165422 (2019).
- [12] E. Lesne, Y. G. Sağlam, R. Battilomo, M. T. Mercaldo, T. C. van Thiel, U. Filippozzi, C. Noce, M. Cuoco, G. A. Steele, C. Ortix, and A. D. Caviglia, Designing spin and orbital sources of berry curvature at oxide interfaces, *Nature Materials* **22**, 576 (2023).
- [13] S. Nandy, G. Sharma, A. Taraphder, and S. Tewari, Chiral anomaly as the origin of the planar Hall effect in Weyl semimetals, *Phys. Rev. Lett.* **119**, 176804 (2017).
- [14] Z. Z. Du, H.-Z. Lu, and X. C. Xie, Nonlinear hall effects, *Nature Reviews Physics* **3**, 744 (2021).
- [15] N. B. Schade, D. I. Schuster, and S. R. Nagel, A nonlinear, geometric hall effect without magnetic field, *Proceedings of the National Academy of Sciences* **116**, 24475 (2019), <https://www.pnas.org/doi/pdf/10.1073/pnas.1916406116>.
- [16] P. Gentile, M. Cuoco, O. M. Volkov, Z.-J. Ying, I. J. Vera-Marun, D. Makarov, and C. Ortix, Electronic materials with nanoscale curved geometries, *Nature Electronics* **5**, 551 (2022).
- [17] D. Hou, G. Su, Y. Tian, X. Jin, S. A. Yang, and Q. Niu, Multivariable scaling for the anomalous Hall effect, *Phys. Rev. Lett.* **114**, 217203 (2015).
- [18] Y. Tian, L. Ye, and X. Jin, Proper scaling of the anomalous Hall effect, *Phys. Rev. Lett.* **103**, 087206 (2009).
- [19] C. Uher and W. P. Pratt, High-precision, ultralow-temperature resistivity measurements on bismuth, *Phys. Rev. Lett.* **39**, 491 (1977).
- [20] F. Avilés, A. Oliva, and J. Aznárez, Dynamical thermal model for thin metallic film–substrate system with resistive heating, *Applied Surface Science* **206**, 336 (2003).
- [21] D. Wawrzik, J. I. Facio, and J. van den Brink, Surface induced electronic berry curvature in bulk berry curvature free materials, *Materials Today Physics* **33**, 101027 (2023).
- [22] Y. Onishi and L. Fu, High-efficiency energy harvesting based on nonlinear hall rectifier (2023), [arXiv:2211.17219 \[cond-mat.mes-hall\]](https://arxiv.org/abs/2211.17219).